

Herschel-PACS observations of far-IR lines in YSOs I: [OI] and H₂O at 63 μm * **

P. Riviere-Marichalar¹, B. Merín¹, I. Kamp², C. Eiroa³, B. Montesinos⁴

¹ European Space Astronomy Centre (ESA), P.O. Box 78, 28691 Villanueva de la Cañada, Spain e-mail: priviere@sciops.esa.int

² Kapteyn Astronomical Institute, University of Groningen, P.O. Box 800, 9700 AV Groningen, The Netherlands

³ Dep. de Física Teórica, Fac. de Ciencias, UAM Campus Cantoblanco, 28049 Madrid, Spain

⁴ Depto. Astrofísica , Centro de Astrobiología (CAB, INTA-CSIC), P.O. Box 78, ESAC Campus, 28691 Villanueva de la Cañada, Madrid, Spain

ABSTRACT

Context. Gas plays a major role in the dynamical evolution of young stellar objects (YSOs). Its interaction with the dust is the key to our understanding planet formation later on in the protoplanetary disc stage. Studying the gas content is therefore a crucial step towards understanding YSO and planet formation. Such a study can be made through spectroscopic observations of emission lines in the far-infrared, where some of the most important gas coolants emit, such as the [OI] ${}^3P_1 \rightarrow {}^3P_2$ transition at 63.18 μm.

Aims. We provide a compilation of observations of far-IR lines in 362 YSOs covering all evolutionary stages, from Class 0 to Class III with debris discs. In the present paper we focus on [OI] and o-H₂O emission at 63 μm.

Methods. We retrieved all the available *Herschel*-PACS spectroscopic observations at 63 μm that used the dominant observing mode, the chop-nod technique. We provide measurements of line fluxes for the [OI] ${}^3P_1 \rightarrow {}^3P_2$ and o-H₂O $8_{00} \rightarrow 7_{11}$ transitions at 63 μm computed using different methods. Taking advantage of the PACS IFU, we checked for spatially extended emission and also studied multiple dynamical components in line emission.

Results. The final compilation consists of line and continuum fluxes at 63 μm for a total of 362 young stellar objects (YSOs). We detect [OI] line emission at 63 μm in 194 sources out of 362, and line absorption in another five sources. o-H₂O was detected in 42 sources. We find evidence of extended [OI] emission in 77 sources, and detect 3σ residual emission in 71 of them. The number of sources showing extended emission decays from Class 0 to Class II. We also searched for different components contributing to the line emission, and found evidence for multiple components in 30 sources. We explored correlations between line emission and continuum emission and found a clear correlation between WISE fluxes from 4.6 to 22 μm and [OI] line emission. We conclude that the observed emission is typically a combination of disc, envelope and jet emission.

Key words. Stars: Circumstellar matter, Stars: evolution, astrochemistry, protoplanetary disks

1. Introduction

Young stellar objects (YSO) are complex sources consisting of many components, such as the central source (protostellar or stellar), an envelope made of gas and dust, a circumstellar disc, stellar and disc winds, and large-scale collimated jets. Each of the components can contribute to different observables, such as photometry and line fluxes. A detailed study is therefore needed to elucidate the contribution of each component.

In the initial stages of stellar formation, Class 0 and I protostars (Lada & Wilking 1984; Lada 1987; Andre et al. 1993) are surrounded by an envelope. Discs are clearly detected around Class I sources. Class I sources later evolve to Class II sources, in which the central star is already formed and the envelope dispersed. The formation of a dust

opacity hole in the inner disc leads to the formation of the so-called transitional discs (Strom et al. 1989). Many mechanisms have been used to explain the formation of the inner opacity holes, including planet formation. At 10 Myr, most primordial discs have been dispersed (Strom et al. 1989), but destructive collisions between planetesimals can repopulate the circumstellar environment with dust, resulting in the so-called debris discs.

Young stellar objects can also be classified according to their masses. The so-called T Tauri stars are variable stars showing bright emission lines with stellar masses $M_* < 2.0M_\odot$, while HAeBe stars are the high-mass counterparts of T Tauri stars ($2.0 < M/M_\odot < 8.0$).

Although gas is thought to dominate the mass budget during the primordial stages (Class 0 to II), little is known about its mass and spatial distribution, mostly because it is difficult to detect H₂, which lacks a permanent dipole moment. However, to learn about the formation of planets, we need to understand the chemical evolution of gas and dust.

The *Herschel Space Observatory* (Pilbratt et al. 2010) produced thousands of observations of YSOs during its

* Tables B1, B2 and B3 are available in electronic form at the CDS via anonymous ftp to cdsarc.u-strasbg.fr (130.79.128.5) or via <http://cdsweb.u-strasbg.fr/cgi-bin/qcat?J/A+A/>

** *Herschel* is an ESA space observatory with science instruments provided by European-led Principal Investigator consortia and with important participation from NASA.

four-year mission. The most widely used instrument was the Photodetector Array Camera and Spectrometer (PACS, Poglitsch et al. 2010), which can spectroscopically observe the far-IR 50–250 μ m range. Furthermore, it also performed photometric observations at 70, 100 and 160 μ m with great sensitivity. One of the most interesting characteristics of the PACS spectrometer is its Integral Field Unit (IFU), divided into 25 spaxels distributed in a regular grid covering 47'' \times 47''. The IFU allows us to study the spatial distribution of the continuum and line emission.

Some studies have surveyed [OI], CO, OH, and H₂O emission in objects belonging to different stellar associations and moving groups using *Herschel* (Donaldson et al. 2012; Howard et al. 2013; Green et al. 2013; Mathews et al. 2013; Lindberg et al. 2014; Riviere-Marichalar et al. 2013, 2014, 2015). Other studies have focused on the analysis of individual sources (Meeus et al. 2010; van Kempen et al. 2010b,a; Sturm et al. 2010; Thi et al. 2010; Tilling et al. 2012; Lebreton et al. 2012; Riviere-Marichalar et al. 2012a; Thi et al. 2013). However, the spatial extension of the emission was discussed in only a few cases (Karska et al. 2013, 2014b; Nisini et al. 2013, 2015). The most extensively studied wavelength range is 63.0–63.4 μ m, which includes two transitions, [OI] ${}^3\text{P}_1 \rightarrow {}^3\text{P}_2$ at 63.185 μ m and o-H₂O $8_{08} \rightarrow 7_{17}$ at 63.325 μ m. [OI] emission has been detected in YSOs at all evolutionary stages, from Class 0 and I (Green et al. 2013) to Class II and transitional (Howard et al. 2013) and debris discs (Riviere-Marichalar et al. 2012b). o-H₂O emission was observed around Class 0, I, II and transition discs, but not around debris discs.

Understanding the spatial distribution of far-IR lines emission is crucial, since it has been shown that envelopes, protoplanetary discs, and outflows can contribute to [OI] emission (van Kempen et al. 2010b; Podio et al. 2012; Karska et al. 2013). [OI] extended emission along the jet direction has been commonly observed, while molecular extended emission is observed in only a few cases (van Kempen et al. 2010b; Herczeg et al. 2012). Podio et al. (2012) and Karska et al. (2013) explained the extended emission as being produced by J- and C-shocks along the jet, and noted a decay in far-IR lines intensity from Class 0/I to Class II. Howard et al. (2013) studied a sample of Class II sources in Taurus, including sources with and without a jet or an outflow. The authors found a tight correlation between continuum emission at 63 μ m and [OI] emission, suggesting a disc origin for the line. However, sources with jets show a brighter [OI] emission for the same level of continuum, indicating a contribution from the jet. The authors did not find a correlation between disc mass (derived from sub-millimeter continuum emission) and [OI] line intensity, indicating that either the line is optically thick or it is a poor tracer of gas mass. Green et al. (2013) studied a sample of 30 embedded sources (Class 0 and I) from the DIGIT program (see e.g. van Kempen et al. 2010a; Sturm et al. 2010) and found a tight correlation between line intensity and L_{bol}.

In this paper, we present a compilation of 432 PACS spectroscopic observations of 362 YSOs and main-sequence stars with debris discs. We focus on the small wavelength range between 63.0 and 63.4 μ m, which includes the [OI] transition at 63.185 μ m and the o-H₂O transition at 63.325 μ m. Our wavelength range selection is motivated by the fact that the [OI] transition at 63.185 μ m typically is the strongest line coolant in protoplanetary discs (Gorti &

Table 1. Overview of the programs used in this study.

Program ID	observations	Sensitivity (10 ⁻¹⁸ W/m ²)
<i>GT1_vgeers_1</i>	2	2.5
<i>KPOT_bdent_1</i>	185	3.1
<i>KPOT_nevans_1</i>	65	7.3
<i>KPGT_golofs01_1</i>	6	2.9
<i>KPGT_evandish_1</i>	28	8.6
<i>OT1_ascholz_1</i>	1	1.2
<i>OT1_cespaill_2</i>	38	20.0
<i>OT1_ckiss_1</i>	9	3.5
<i>OT1_gmeeus_1</i>	2	28.0
<i>OT1_ipascucc_1</i>	30	1.6
<i>OT1_maudar01_1</i>	11	23.0
<i>OT1_vgeers_2</i>	4	2.5
<i>OT2_amoor_3</i>	2	3.8
<i>OT2_evandish_4</i>	49	7.7

Hollenbach 2008). We leave the study of other transitions observed in *PACS* range mode for a future paper.

2. Sample and observations

The data were collected from fourteen different programs (see Table 1). The sample consists of 362 YSOs and main-sequence stars with debris discs observed with PACS spectroscopy at 63 μ m. The total number of observations was 432: 51 sources were observed twice, and another nine sources were observed three times. We only included pointed observations from programs that used the chop-nod technique to remove the telescope and background contribution. The sample includes objects in all the different evolutionary stages for circumstellar material, from Class 0 to Class III stars and to those that are later surrounded by debris discs (see Fig. 1). Highly embedded sources from the DIGIT program (Sturm et al. 2010) were included, together with highly embedded and high-mass protostellar envelopes from the WISH program (van Dishoeck et al. 2011). Transition discs are a particular case of Class II discs that have opened a gap in the inner part of the disc.

Throughout the paper we treat transition discs separately because of their importance in testing planet formation theories. When we refer to Class II discs, we therefore refer to full discs without an inner gap, in contrast to transition discs which show inner opacity holes. Because of the limited size of the samples and because of the similarities we found, we treat Class 0 and I sources in some sections as a single group of protostellar objects (see Sect. 4). Most of the stars in the sample belong to different star-forming regions and stellar associations, with ages in the range 1–40 Myr, including Tau, Cha, Cha II, Lupus, Lupus III, η Cha, Upper Scorpius, TWA, BPMG, Tuc Hor, CrA, Serpens, Per, and Oph. The source names, positions, spectral type (for Class II and III sources), evolutionary status, and associations for YSOs in the sample are given in Table B.1.

Observations were performed in two different modes depending on the program: line spectroscopy, covering 63.0 to 63.4 μ m (301 observations), and range spectroscopy (131 observations), covering 55 to 72 μ m. Line spectroscopy observes a narrow spectral region centred on a certain spectroscopic transition ([OI] ${}^3\text{P}_1 \rightarrow {}^3\text{P}_2$ in our case), and guarantees the detection of the full line profile for an unresolved line, with enough continuum coverage at either side

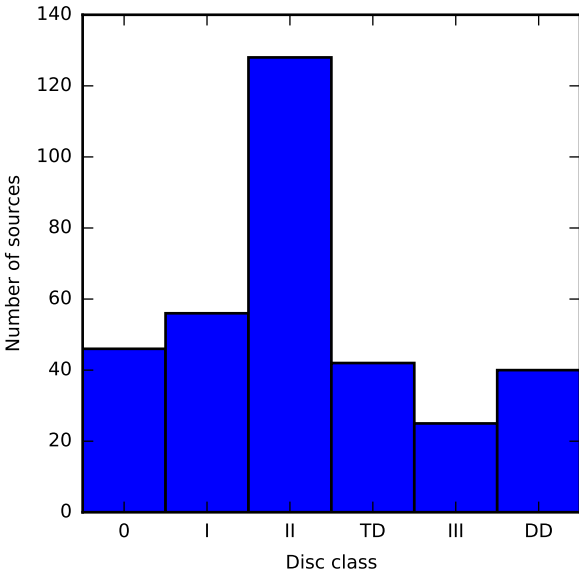


Fig. 1. Distribution of evolutionary stages in the observed sample.

of the line to allow for continuum measurements. Range spectroscopy covers a region around the lines of interest defined by the observer. The 63.0–63.4 μ m range contains the [OI] $^3\text{P}_1 \rightarrow ^3\text{P}_2$ transition at 63.185 μ m and the o-H₂O 818 \rightarrow 707 transition at 63.325 μ m. We focus in this paper on the study of the two lines in the 63 to 63.4 μ m wavelength range. Exposure times ranged from 851 s to 16420 s, with 75% of the observations having $t_{\text{exp}} < 4000$ s. All the observations were performed in chop-nod mode, with a small chopper throw (1'.5) for 299 sources (~71%), medium chopper throw (3') for 13 (~3%) and large chopper throw (6') for 107 (~26%). Most observations used only one nod cycle (~67%), ~26 % used two nod cycles, four observations (~1%) used three nod cycles, 23 (~5%) used four nod cycles and six used five nod cycles (1%).

3. Data reduction

The data were reduced using HIPE 12.0. The reduction was performed as follows. First, the observations were corrected for satellite movements. Then, saturated frames and frames with glitches were flagged and masked, and the chop-off position was subtracted from the chop-on position to remove the sky and telescope contribution. Then, the cubes were divided by the spectral response function, and after that, flat-fielding, using a straight line, was applied to improve the signal-to-noise ratio (S/N) of the continuum. We used a straight line for flat-fielding. Then, the spectra were rebinned, with oversample = 2 and upsample = 4. Observations from the *OT1_cespaill_2* and *OT1_maudar01_1* programs, and some observations from the program *KPOT_nevans_1*, required oversample=2 and upsample=2 (native resolution of the instrument). Finally, the mean value from the two nod positions was computed.

Given the noise increment in the edges of the spectra, we only considered the spectral range from 63.0 to 63.4 μ m for

line spectra and the range 62.5–63.9 μ m for range spectra. We subtracted the continuum contribution by fitting a first-order polynomial after masking a $\pm 3\sigma$ (where σ is the width of an unresolved line at the wavelength of interest) region around each transition present ([OI] and o-H₂O at 63.185 and 63.325 μ m, respectively). Line fluxes were computed by integrating a Gaussian fit to continuum-subtracted spectra of the spaxel with the highest flux. When the continuum was not detected to the 3σ level, we extracted the spectrum from the central spaxel ($x=2$, $y=2$). The spectrum from this spaxel was then aperture corrected. For some sources, a mis-pointing of *Herschel* causes the source to lie in between many spaxels, and therefore the computed flux is a lower limit to the actual flux. Adding the 3×3 spaxels around the position of the source gives a more accurate flux for these sources. The uncertainties on the line fluxes were computed as the integral of a Gaussian with a width equal to the fitted value and a peak equal to the noise of the continuum. Three-sigma upper limits were computed in a similar way as three times the integral of a Gaussian with a width equal to the instrumental value and a peak equal to the noise of the continuum. Given the spread in observing times between the different programs, the sensitivity limits are in the range 1.2×10^{-18} to 2.8×10^{-17} W/m² (see Table 1). We also obtained continuum fluxes at 63 μ m by computing the mean value of the baseline after excluding the 3σ regions around the position of detectable lines, with errors being the standard deviation inside the same region.

4. Results

Examples of continuum-subtracted spectra for different evolutionary stages are shown in Fig. 2. We also show the Gaussian fits to the observed profiles used to compute line fluxes, together with residual plots at the bottom of each spectrum. The shift in the observed line centres compared to the theoretical ones in some sources might be due to mis-pointing of the telescope, since it is a known PACS effect that telescope mis-pointing results in a shift in wavelengths, which hinders concluding whether the line shift is real. The strength of the [OI] line compared to the o-H₂O is evident from the plots, with typical line ratios $F_{[\text{OI}]} / F_{\text{H}_2\text{O}}$ in the range 2.4 to 29. The only exception is BP Tau, where the o-H₂O and [OI] line fluxes at 63 μ m are similar, within the errors.

4.1. Line emission

We detected the [OI] emission line at 63.185 μ m (3σ) in 194 sources out of 362 observed (0.54 ± 0.04 detection fraction). Line fluxes from the central spaxel are given in Table B.2. The detection fractions strongly depend on the evolutionary stage. Class 0 and I sources show very similar detection fractions ($0.87^{+0.04}_{-0.07}$ and $0.93^{+0.02}_{-0.06}$, respectively), but show strong differences with Class II stars ($0.53^{+0.06}_{-0.05}$, including both T Tauri and HAeBe stars). The detection fraction, also seems to depend on the stellar mass, since there is a strong difference between T Tauri and HAeBe stars ($0.42^{+0.05}_{-0.05}$ and $0.96^{+0.01}_{-0.08}$, respectively). Transition discs and full Class II disc sources show detection fractions that are almost compatible ($0.56^{+0.07}_{-0.08}$ for transition discs). Finally, [OI] was detected towards four debris disc sources (HD 172555, β Pictoris, RXJ18523-3700 and HD 141569), lead-

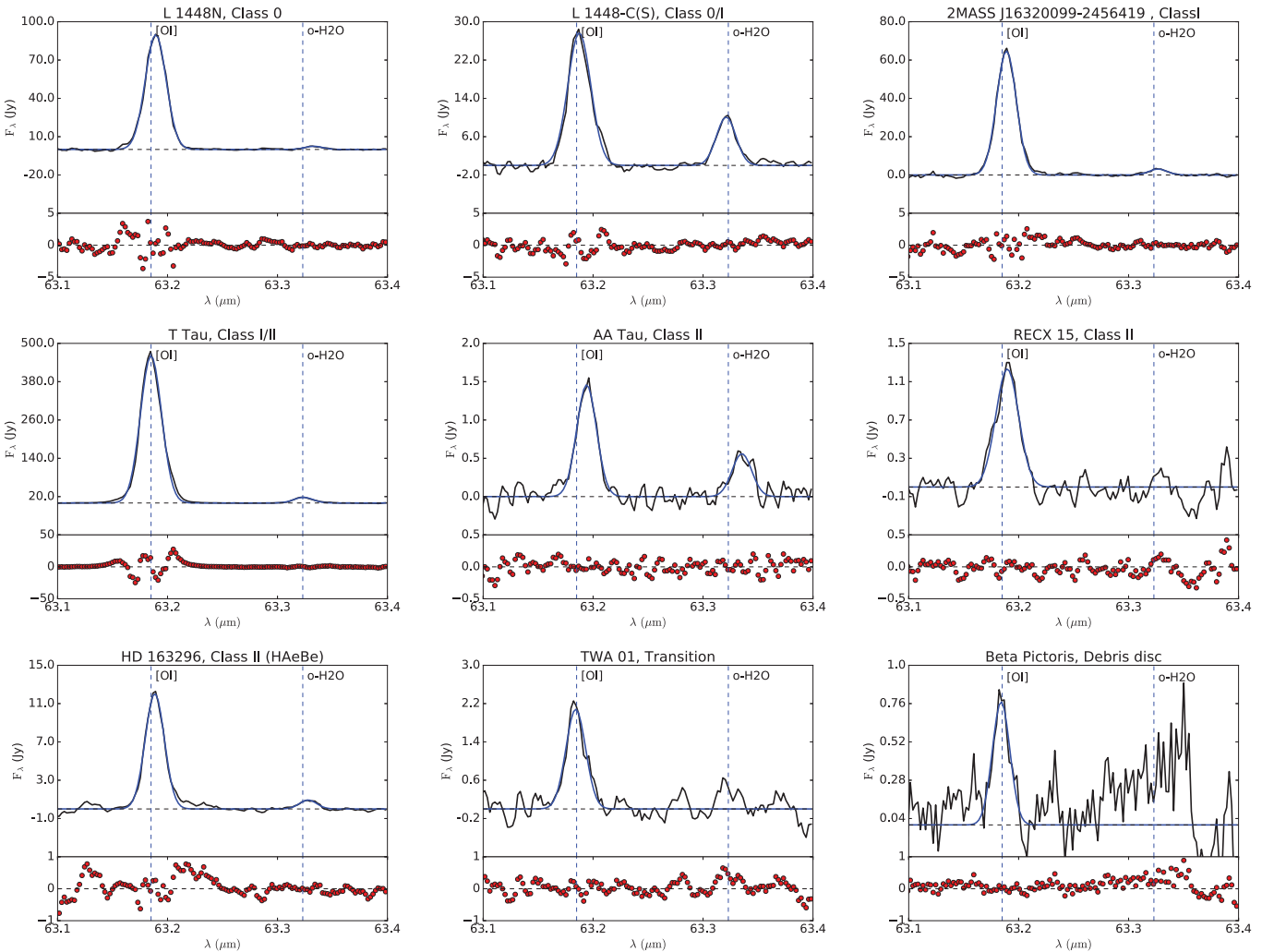


Fig. 2. Example of continuum-subtracted spectra of stars at different evolutionary stages. The black line shows the observed spectra, while the blue line shows a Gaussian fit. We show the rest-frame wavelength of the [OI] and o-H₂O emission lines and vertical dashed blue lines with labels identifying each line. Plots with the model residuals are shown at the bottom of each spectrum.

ing to the smallest detection fraction ($0.10^{+0.07}_{-0.03}$). The detection fraction is likely to be even smaller, since HD 141569 is considered either a HAeBe star (Mendigutía et al. 2011) or a debris disc (Marsh et al. 2002).

o-H₂O at 63.325 μ m was detected in 43 out of 362 sources (0.12 ± 0.02 detection fraction). o-H₂O line emission was only detected in sources where we also detected [OI] emission. Eight of these are Class 0 sources, two are intermediate Class 0/I sources, 20 are Class I sources, one (T Tau) is an intermediate Class I/II source, ten are Class II sources (eight of them are T Tauri stars, and two are HAeBe stars), and two are transitional discs.

[OI] line fluxes extracted from the central spaxel range from 4×10^{-18} to 4×10^{-14} W/m² and o-H₂O line fluxes range from 6×10^{-18} to 7×10^{-16} W/m². We show in Fig. 3 the distribution of [OI] (top) and H₂O (bottom) luminosities for the different types of sources. Class 0 and I sources show a similar distribution of [OI] luminosities. However, they show quite different H₂O distributions. Class II and transitional discs show more differences in their [OI] luminosity distributions than they do in their H₂O luminosity

distributions. The low number of H₂O detections precludes any further comparison of the distributions. The vertical dashed lines in Fig. 3 show the median [OI] line luminosity for each class. We observe a clear evolutionary trend, with [OI] line luminosities that decrease from Class 0 to Class II and transitional, in agreement with the finding by Podio et al. (2012) and Karska et al. (2013), where a decrease in molecular luminosity and total line luminosity was observed.

To test whether the differences of [OI] luminosity distributions between the different classes are real, we performed two-distribution Kolmogorov-Smirnov tests for the different pairs of datasets. Class 0 and I sources do not differ in their distribution of [OI] fluxes ($P=0.93$). As we find no difference between both distributions, we combined the two distributions for an additional comparison with the other classes. The comparison with the distributions for Class II bear strong differences: $P \ll 10^{-3}$ for Class II sources compared to Class 0 and I sources, where Class II includes full disc T Tauris, transition discs T Tauris and HAeBe stars. The difference is dominated by low-mass stars, since the proba-

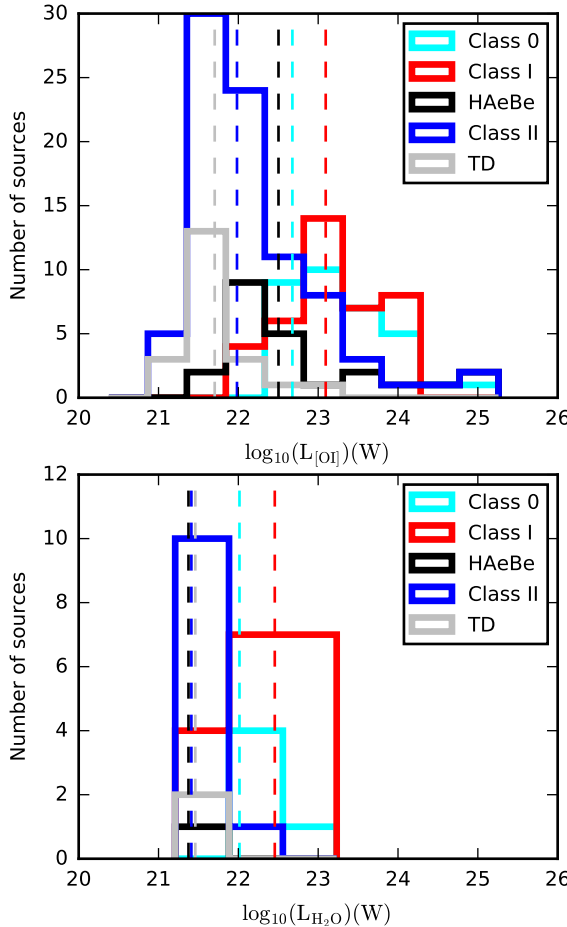


Fig. 3. Top: histogram for [OI] line luminosities in the observed sample. Bottom: histogram for H₂O line luminosities in the observed sample. The vertical dashed lines show the median luminosity for each class.

bility is $P \ll 10^{-3}$ when HAeBe stars are excluded from the comparison. The comparison between T Tauri stars and HAeBe stars also shows strong differences ($P \sim 10^{-3}$). We furthermore compared the distribution of luminosities for T Tauri stars surrounded by full discs and those surrounded by transitional discs, and found a probability $P \sim 10^{-3}$ that both populations are build from the same distribution. We did not perform the comparison for debris discs sources due to the small number of detections. However, we highlight the large dispersion of [OI] fluxes observed in debris discs, with only four detections covering more than two orders of magnitude. Figure 3 also shows an evolution of the typical [OI] luminosity with class, with the peak of the distribution having its maximum at fainter luminosities when moving from Class 0 to Class II and transitional discs.

It is important to note that many sources suffer from mis-pointing, affecting both the fluxes and the future assessment of extended emission (Sect. 4.4). This mis-pointing can be in the form of small shifts, which makes the flux from the central spaxel a poor estimate of the real value. In other cases, the shift can cause the source to be located in a spaxel other than the central one. In these cases, the sources can again be properly centred inside this spaxel

or it can be shifted. These sources are marked in Table B.2 with an asterisk.

4.2. Line absorption

Five sources in the sample showed line absorption, at least in the central spaxel. These sources are AFGL 2591, G327-0.6, G34.26+0.15, NGC 6334-I, and W33A. Their spectra are shown in Fig. 5. They are part of the WISH sample, and are classified as high-mass YSOs (van Dishoeck et al. 2011). Since the observations were performed using the chop-nod technique, we inspected the on and off positions separately. We always found absorption in the on position, and only in one case, W33A, we observe faint emission in the off position. Therefore, we conclude that the observed absorption features are real.

The sources showing absorption were discussed in detail by Karska et al. (2014a). For two sources, namely AFGL 2591 and NGC 6334-I, the profile features the shape of a P-Cygni profile (Karska et al. 2014a). Line maps for sources showing absorption in the [OI] transition at 63.185 μ m are shown in Fig. 6, where we can see that absorption peaks at the positions where the continuum reaches the maximum. Absorption towards NGC 6334-V was previously reported by Kraemer et al. (1998), who attributed the absorption to cooler or less dense gas in the foreground core cloud.

Even if all the sources showing line absorption were high-mass YSOs, we cannot conclude that high-mass envelopes lead to absorption, since another three high-mass YSOs in the sample, namely DR 21 (OH), NGC 7538 IRS1, and W3-IRS5 show prominent emission. None of the eight sources showed o-H₂O emission or absorption at 63.323 μ m.

4.3. Continuum and line variability

A total of 60 sources were observed multiple times (see Sect. 2, the discussed fluxes are shown in Table B.2). We can use this subsample to gain insight on line and continuum variability in the far-IR. In terms of line emission, we can distinguish three groups:

- Sources that show fluxes that agree, within the uncertainties. This group contains 38 sources.
- Sources that show fluxes that do not match because of a mis-pointing in one (or all) the observations. This group contains 16 sources. Mis-pointed sources mostly come from the GASPS program, where a problem with the pointing of Taurus sources has been highlighted by Howard et al. (2013). These sources are properly flagged in Table B.2.
- Sources with fluxes that do not match, and where the disagreement is not due to mis-pointing, but most likely to real variability or unknown instrumental effects. This group includes six sources: HD 100453, HD 139614, HD 142527, HD 36112, IRAS 04016+2610, and SAO 206462. The spectra obtained at different epochs for these sources are shown in Fig. 7. Five of these (HD 100453, HD 139614, HD 142527, HD 36112 and SAO 206462) are HAeBe stars, and one (IRAS 04016+2610) is a Class 0/I embedded source. For IRAS 04016+2610 the difference in the fluxes could be due to the different observational techniques used, since one of the observations is a line spectrum, while the other is a range spectrum. Furthermore, all sources are variable at most

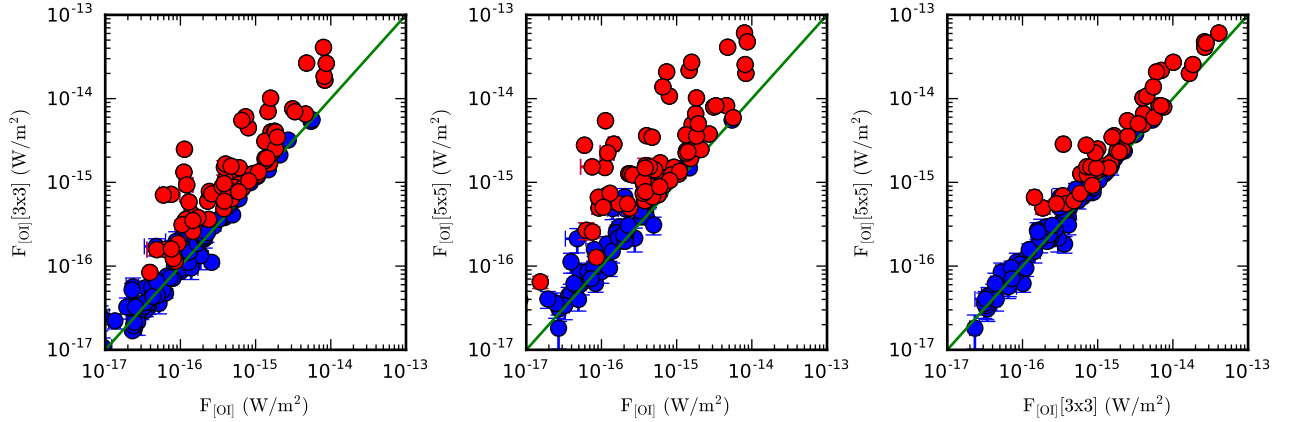


Fig. 4. Extended emission tests for sources in the sample. Red dots identify sources showing extended emission in each of the tests. The solid diagonal line depicts a one-to-one ratio to help identify extended emission.

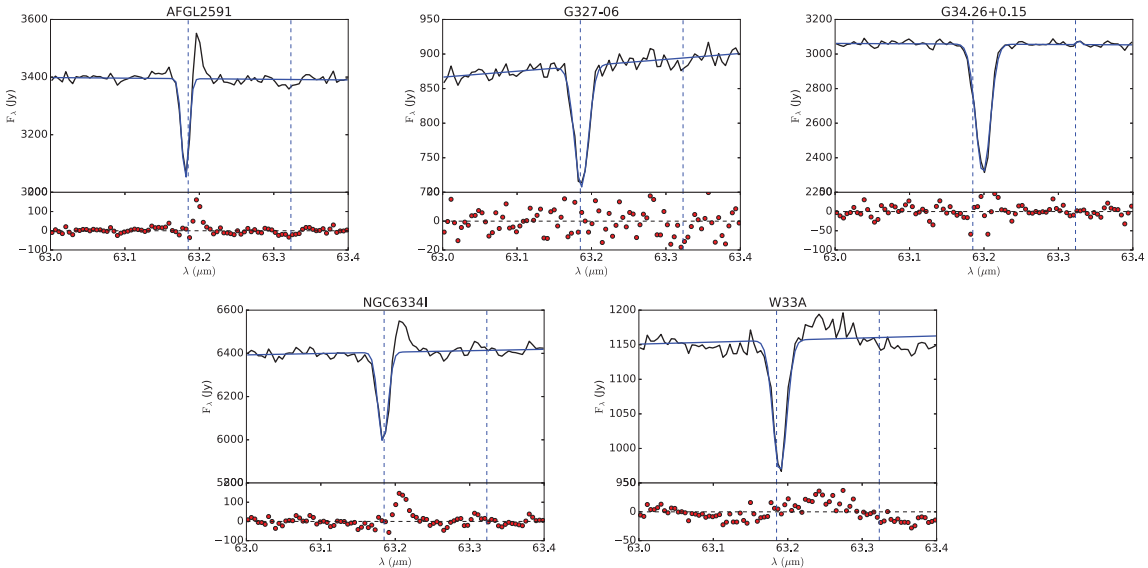


Fig. 5. Spectral profiles for high-mass YSOs showing [OI] line absorption.

at the 3σ level. For HD 100453, three observations are available, and none of them shows compatible line fluxes at the 1σ level, but they are compatible at the 3σ level. Furthermore, the continuum sources are not compatible at either the 1 or 3σ levels.

Follow-up of [OI] line emission at 63 μ m is needed to understand line variability and rule out instrumental effects.

4.4. Extended emission

The Integral Field Unit (IFU) used for PACS spectroscopy allowed us to study whether the emission is extended or not. We first compared the flux derived from the central spaxel (or the spaxel with the highest signal) to those derived from co-adding the nine central spaxels (test 1) and the 25 spaxels (test 2). Finally, we also compared the flux from the central nine spaxels with that of the 25 spaxels (test 3). If the emission is extended, we expect the co-added fluxes to be substantially higher than the flux from

the central spaxel. This stronger emission from co-added spaxels can be due to extended emission or to the presence of multiple sources. On the one hand, if the flux from the 25 spaxels were higher than the flux from the central spaxel, but the flux from the central were coincident with the flux from the central spaxel, then the most likely explanation would be the presence of another source (or sources) in the outer spaxels. On the other hand, if we were to detect higher fluxes only when the central nine spaxels are considered, then the difference would most likely be due to extended emission. We are aware that by co-adding the different spaxels, the signal detected in one of them can be diluted when the other spaxels are noise-dominated.

We show in Table B.3 the computed fluxes for sources detected with at least one of the two methods. In Fig. 4, we compare the different fluxes computed to test for extended emission. When the difference in flux is larger than three times the quadratic sum of the uncertainties, we consider that the emission is extended. Sources with extended emission are shown as red dots in Fig. 4. When test 1 was

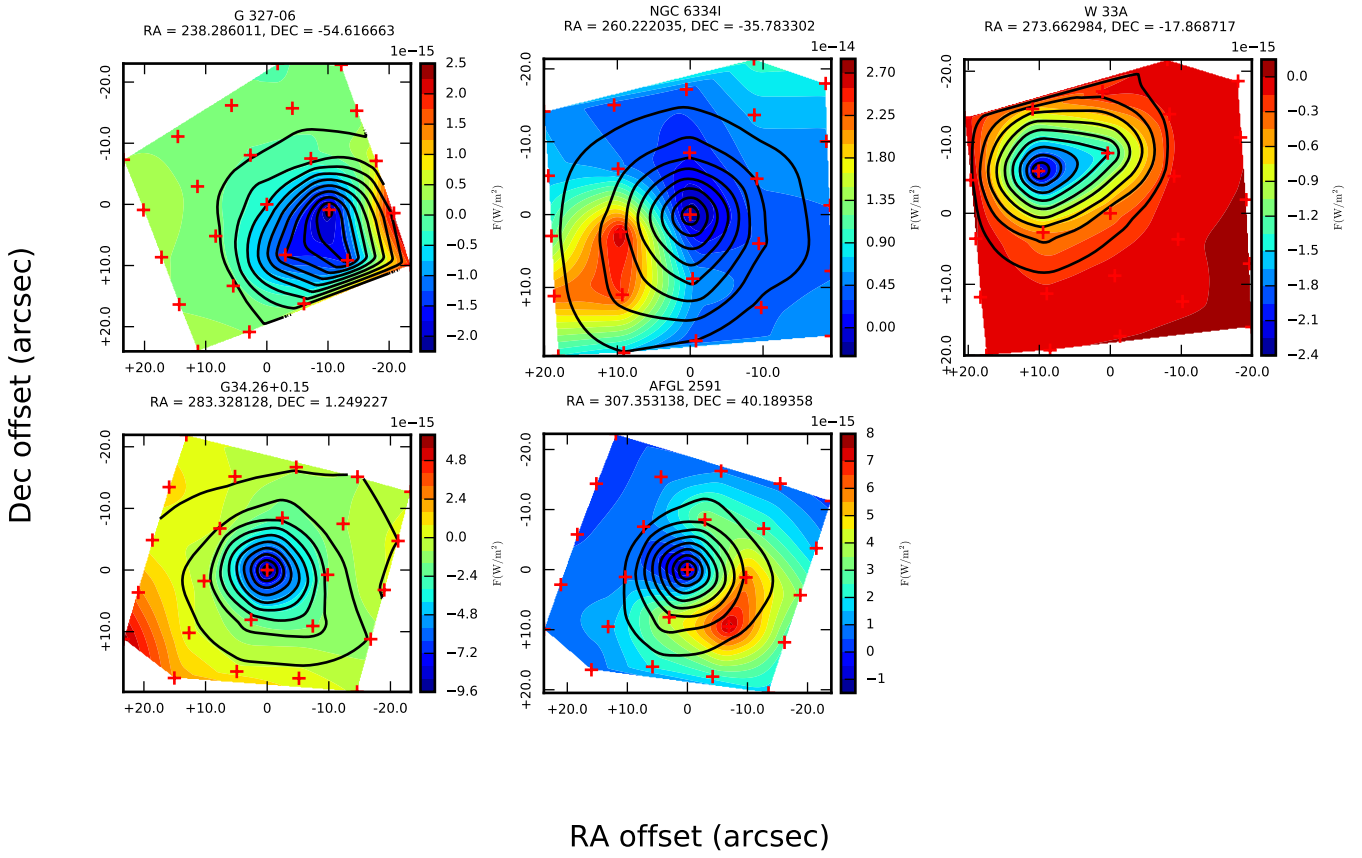


Fig. 6. Line emission (coloured contours) and continuum maps at 63 μ m (solid lines) for sources showing [OI] absorption at 63.185 μ m. The crosses mark the position of individual spaxels.

used, 69 sources showed extended emission, 59 of which belonged to Class 0 and I, 9 belonging to Class II and transitional (including both T Tauri and HAeBe stars) and one is a highly embedded source with unknown class (RCrA-IRS7A). When test 2 was used, 69 sources showed extended emission, 56 of which belonged to Class 0 and I, 12 to Class II and transitional, and one is a highly embedded protostar (RCrA-IRS7A). Finally, 51 sources showed extended emission when Test 3 was used, 41 of which belonged to Class 0 and I, eight belonged to Class II and transitional, and two are highly embedded protostars (RCrA-IRS7A and AFGL 2591, which shows absorption in the central spaxel, together with extended emission in the surrounding spaxels). The final fraction of extended sources per class is shown in Fig. 8.

For all the sources showing higher fluxes from co-added spaxels, we used the method by Podio et al. (2012) to detect extended emission. This method compares the ratio of line to continuum emission in the different spaxels with that in the central one, aiming to detect residual emission over the expected value. The method implicitly assumes that the continuum is emitted by a point source. While this is true for most Class II sources and transitional discs, it might not be true for Class 0 and I sources in the sample, as shown by Lindberg et al. (2014).

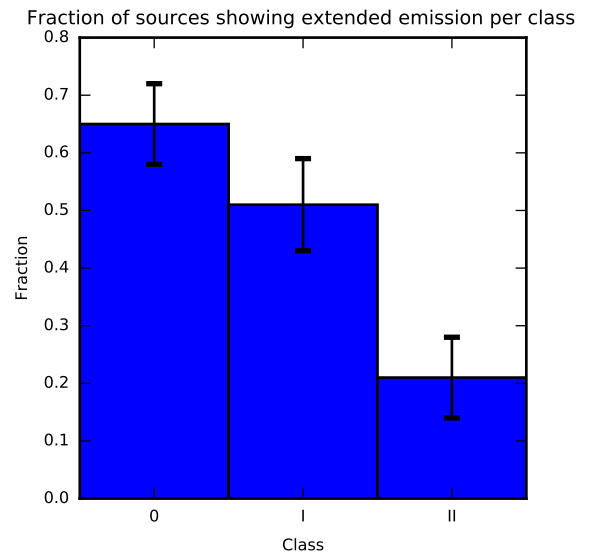


Fig. 8. Bar plot showing the global fraction of sources with extended [OI] emission per class.

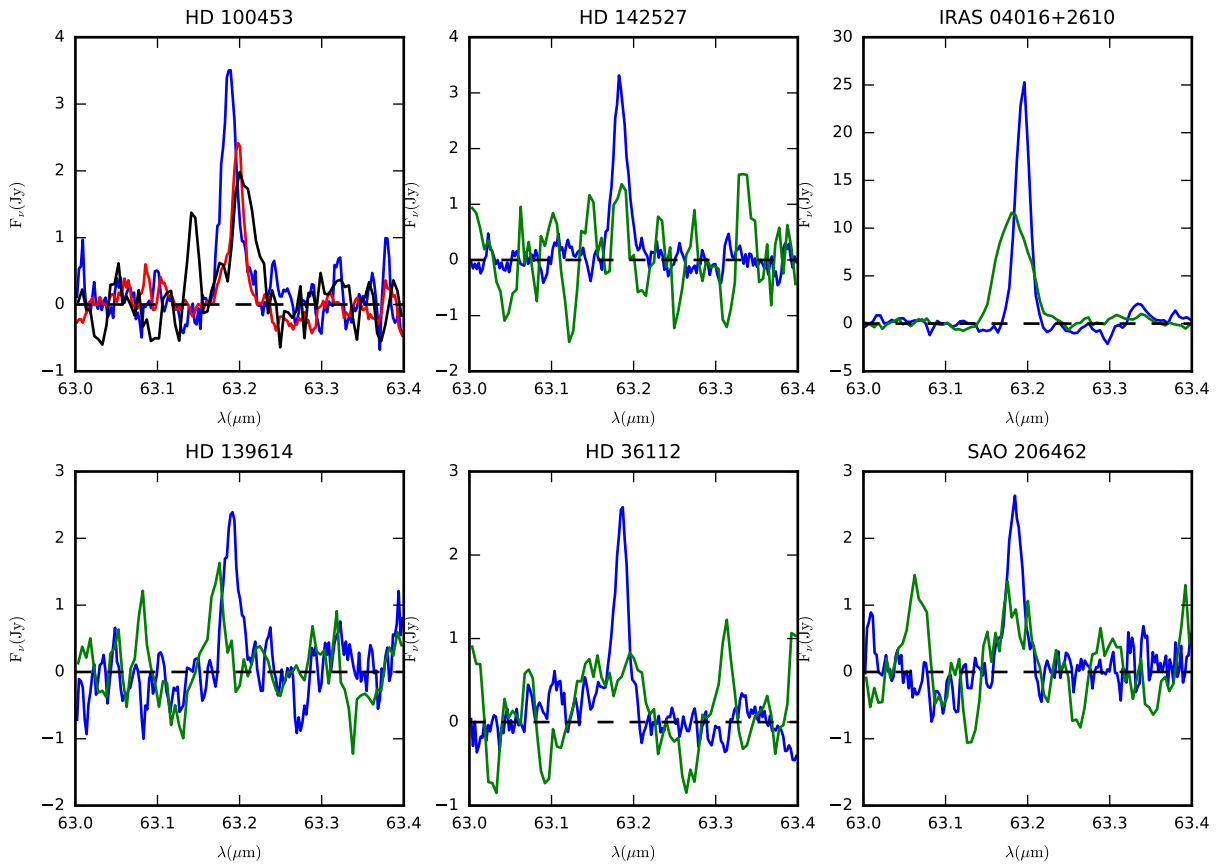


Fig. 7. Spectra obtained at different epochs showing hints of line variability.

We detected 3σ residual emission in the maps of 71 sources (line emission maps for these sources are shown in Fig. A.1 and residual maps are shown in Fig. B.1). FS Tau and FS Tau B are both included in the same OBSID, making the algorithm identify false residual emission. The residual found westward of the source is indeed emitted by FS TauB. The fields for RCRA-IRS7B are too crowded, and therefore we decided to exclude them from the analysis. Lindberg et al. (2014) performed a detailed study of this region, and we refer to this paper for more detailed results.

To compare between continuum and line emission, we distinguished three groups of maps. In the first group, we included sources that showed the peaks of line and continuum emission at the same position. In total, 39 sources were included in this first group. Prominent examples of this type are the maps of sources such as IRAS 03235+3004 or IRAS 04264+2433. In the second group, we included 18 maps where continuum and line emission peak at different positions. Examples of this sources are NGC1333 IRS 4A and VLA 1623-243. Finally, the third group, with 14 observations, included very complex maps, mostly due to the presence of multiple sources. For this third group, the analysis of line emission and continuum maps is precluded, since it is a very complicated task to isolate the contribution of each component. Again, we refer to Lindberg et al. (2014) for insight into the methods that can be used.

Only one source showed extended emission in o-H₂O at 63.325 μ m, NGC 2071, a Class 0 source from the WISH program. Its line emission and residual maps are shown in Fig. 9. The source shows both [OI] and o-H₂O residual emission. [OI] residual emission is found south and north-east of the source, while o-H₂O residual emission is found southward only. Interestingly, [OI] residual emission is brighter in the north-east position than in the south position, and the maximum is ~ 10 times brighter than that of the o-H₂O residual. Melnick et al. (2008) detected extended warm H₂O emission in the region aligned with the direction of the outflow.

4.5. Multiple components

van Kempen et al. (2010b) showed that the profile of the [OI] line at 63 μ m towards HH 46 observed with PACS consisted of three components: blue- and red-shifted components and a rest-frame velocity component. The authors also showed that the velocities of the red- and blue-shifted components are consistent with observations of jets in the near-IR and in the optical. In Riviere-Marichalar et al. (2015), the [OI] emission line was fitted by multiple Gaussians in DK Cha, indicating that several dynamical components might be present. The different velocities can be attributed to different components. While the rest-frame

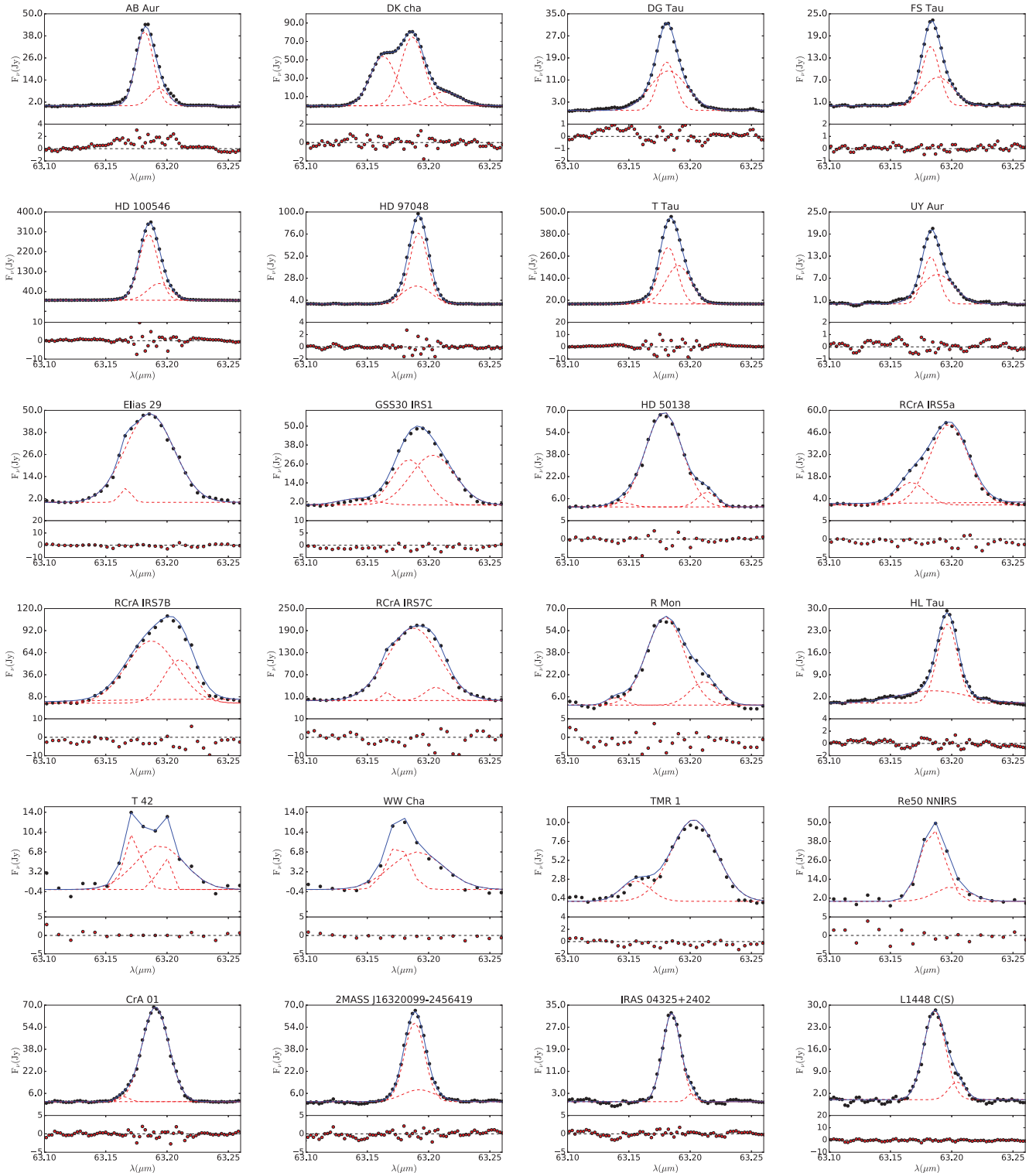


Fig. 10. Multiple-component fits for sources that are better fitted by a combination of two to three Gaussians. The red dashed lines show the individual Gaussian components, while the blue solid lines depict the combined model. Black dots represent the observed spectra.

emission seems to be associated with an envelope and/or disc plus wind emission, the most natural explanation for high-velocity components is jet emission.

We performed a multiple Gaussian analysis of the YSOs in the sample. Model fits with one, two, or three Gaussian

components were compared using the Bayesian information criterion (BIC, see Feigelson & Babu 2012) to detect the most representative one. The BIC is described for each model as

$$\text{BIC} = -2 \times \ln(L^0(M)) + k \times \ln(N) \quad (1)$$

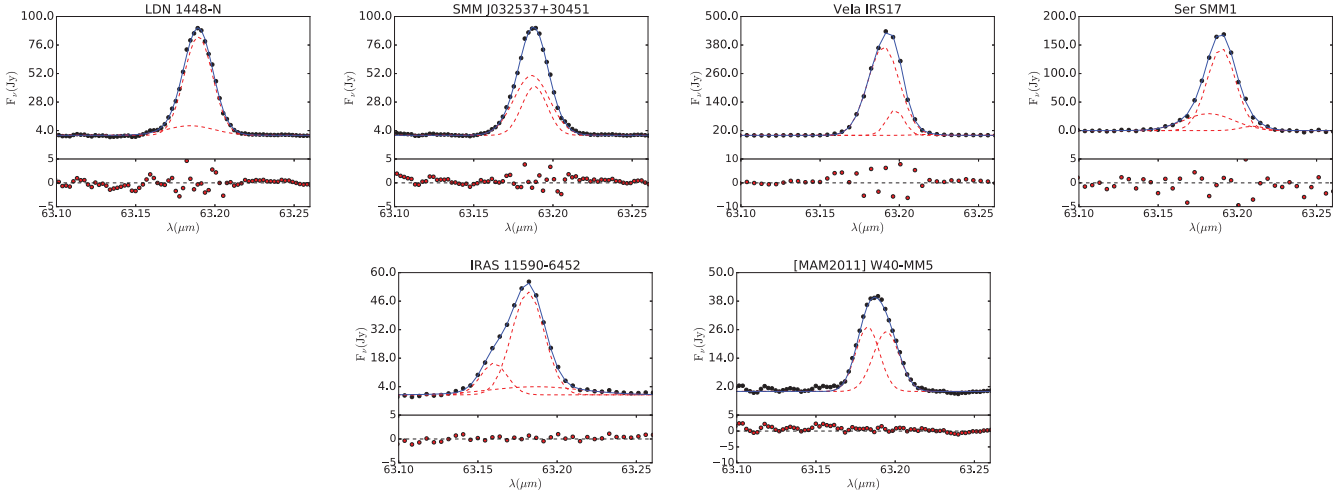


Fig. 10. continued.

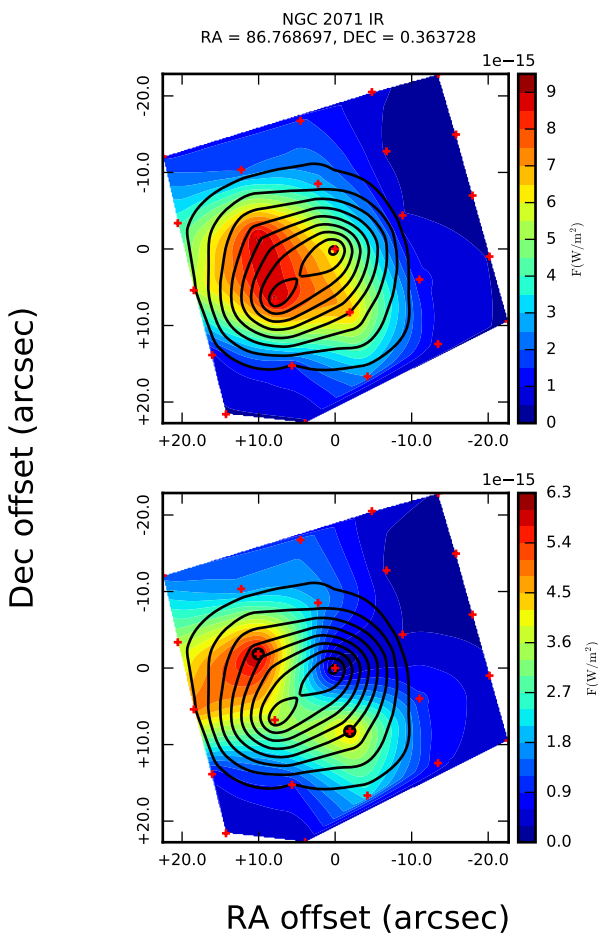


Fig. 9. Top: o-H₂O emission at 63 μ m map for NGC 2071 IR.. Bottom: residual map for o-H₂O emission at 63 μ m for NGC 2071 IR. The solid line contours depict the continuum emission in both panels.

where $L^0(M)$ is the highest value of the likelihood distribution, k is the number of free parameters, and N the number

of spectral points. To detect the best model in each case, we performed a χ^2 minimization, and therefore Eq. 1 becomes

$$\text{BIC} = \chi_0^2 + k \times \ln(N) \quad (2)$$

where χ_0^2 is the lowest value of χ^2 , corresponding to the highest value of the likelihood distribution. To decide which model better reproduces the observations, the BIC for one-, two-, and three-Gaussians models must be compared. A BIC difference $2 < \Delta\text{BIC} < 6$ shows evidence against the model with the higher BIC, while a BIC difference larger than 10 excludes the model with the higher BIC with high probability.

Thirty sources showed evidence of multiple components. We show in Fig. 10 the resulting fits for these sources, and the Gaussian parameters are given in Table 4. It is a known effect that when a source is not properly centred on a PACS spaxel it can result in a shift in the line centre and in a distortion of the Gaussian shape. However, 24 of the 30 sources are properly centered on their spaxels, and therefore, at least for them, we are sure that the effect is real and not an observational artefact. The number of sources per evolutionary stage is as follows: one is a highly embedded source with unknown evolutionary stage, four are Class 0 sources, one is an intermediate Class 0/I sources, 12 are Class I, one is an intermediate Class I/II, 10 are Class II (six are T Tauri and four are HAeBe stars), and one is a transitional disc.

Fourteen of them have a smaller separation between the different components than the spectral resolution at 63 μ m, ~ 88 km/s. Twenty sources are better reproduced by a model with two Gaussians, while twelve sources are better reproduced by a model with three components. The most prominent case is that of DK Cha (see Riviere-Marichalar et al. 2015), where the separation between the different components in the central spaxel is evident. Of the 30 sources that need multiple Gaussians to be fitted, 21 show evidence of extended emission according to their 3×3 fluxes and 5σ residual emission in their IFUs.

To test whether detecting multiple components was linked to high S/N observations, we compared the distributions of continuum and line S/Ns of the whole sample

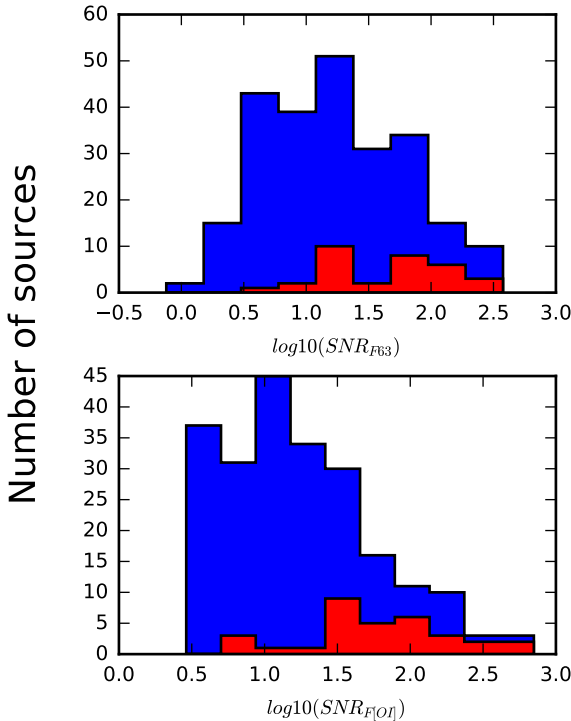
Table 2. Distances to associations in the sample

Fig. 11. Top: distribution of continuum S/N for the whole sample (blue) and for sources that are better reproduced by multiple Gaussians (red). Bottom: distribution of line S/N for the whole sample (blue) and for sources that are better reproduced by multiple Gaussians (red).

with that of sources that are better reproduced by multiple Gaussians. Histograms comparing the distributions are shown in Fig. 11, demonstrating that multiple-Gaussian detections are linked to high S/N sources. A Kolmogorov-Smirnov test confirmed this trend: the probability that both distributions are drawn from the same sample are $\sim 10^{-3}$ for the continuum S/N and $\sim 10^{-7}$ for the line S/N. Therefore, we cannot rule out that some, if not all, of the low-S/N sources also have multiple components.

5. Discussion

As shown by Podio et al. (2012), [OI] emission can be extended along the jet direction, indicating that the jet contributes to, or even dominates, the line emission. We computed in Sect. 4.4 residual emission maps for sources in the sample, and showed that [OI] is extended for a large number of sources: 83 sources show extended emission when the flux from the central spaxel is compared to that of co-added ones, and 71 of them showed residual emission. We also showed that H₂O emission is extended in only one case, compared to [OI], an indication that the o-H₂O line most likely has its origin in a compact and high-density region at the base of the jet (see Podio et al. 2012), like the disc or shocks along the cavity walls in the envelope. Aiming to better understand the physics behind the line emission at 63 μ m and its origin, we compared line fluxes and different observables. To minimize the scatter associ-

Association	Distance (pc)	Reference
BPMG	33	Zuckerman & Song (2004b)*
Cha	165	Luhman (2008)
Cha II	178	Luhman (2008)
CrA	130	Neuhäuser & Forbrich (2008)
η Cha	97	Mamajek et al. (1999)
Lupus	150	Comerón (2008)
Lupus III	200	Comerón (2008)
Oph	130	Wilking et al. (2008)
Per	235	Hirota et al. (2008)
Serpens	415	Dzib et al. (2010)
Taurus	140	Kenyon et al. (2008)
TWA	50	Webb et al. (1999)
Tuc Hor	46	Zuckerman & Song (2004b)*
Up Sco	145	de Zeeuw et al. (1999)

Notes. (*): the distance provided is the average of the distances to individual sources shown in the referenced papers.

ated with the different distances, all the fluxes were scaled to the distance to Taurus (140 pc, Kenyon et al. 2008), so that only sources belonging to known associations or with known distances were used. The distances for the different associations are given in Table 2.

5.1. Correlation between far-IR line emission fluxes

In Fig. 13, we show the relation between o-H₂O line flux and [OI] line flux at 63 μ m. This correlation was previously found by Riviere-Marichalar et al. (2012b). With better source statistics, we now tentatively see a change in slope from Class 0 and I to Class II sources. However, the small number of o-H₂O detections precludes any firm conclusion. The fact that [OI] and o-H₂O fluxes at 63 μ m are correlated might suggest a common origin for the two lines. However, while [OI] is sometimes extended, the o-H₂O line is extended in only one source. Furthermore, while we sometimes need multiple components to fit the [OI] line, a simple Gaussian fit is enough to fit the o-H₂O line in all detections. However, the lack of multiple components can be linked to the low-S/N nature of the detections. Adding more evidence against a co-spatial origin, the critical density for the o-H₂O line is orders of magnitude higher than the one for [OI].

The lack of multiple-components in the profile of o-H₂O might be due to low S/N. o-H₂O detections with a line flux S/N similar to that of [OI] lines that require multiple Gaussians (such as L1448-C(S), $S/N_{H_2O} \sim 24$), are well reproduced by a single Gaussian. We show in Fig. 12 a comparison of the [OI] and H₂O line profiles for sources whose [OI] profiles are better reproduced by a combination of Gaussians. L1448-C(S) and 2MASS J16320099-2456419 show similar [OI] and H₂O profiles, with bumps at similar velocities ($\sim 50 - 100$ km/s), but narrower H₂O lines. By contrast, L 1448N, FS Tau and UY Aur show very different profiles. T Tau show similar shapes for both lines, but the H₂O shows a narrower profile and no bumps are seen. Observations with high spectral resolution are needed to explain multiple components.

The most likely explanation for the spatial extension of the emission, and for the presence of multiple components

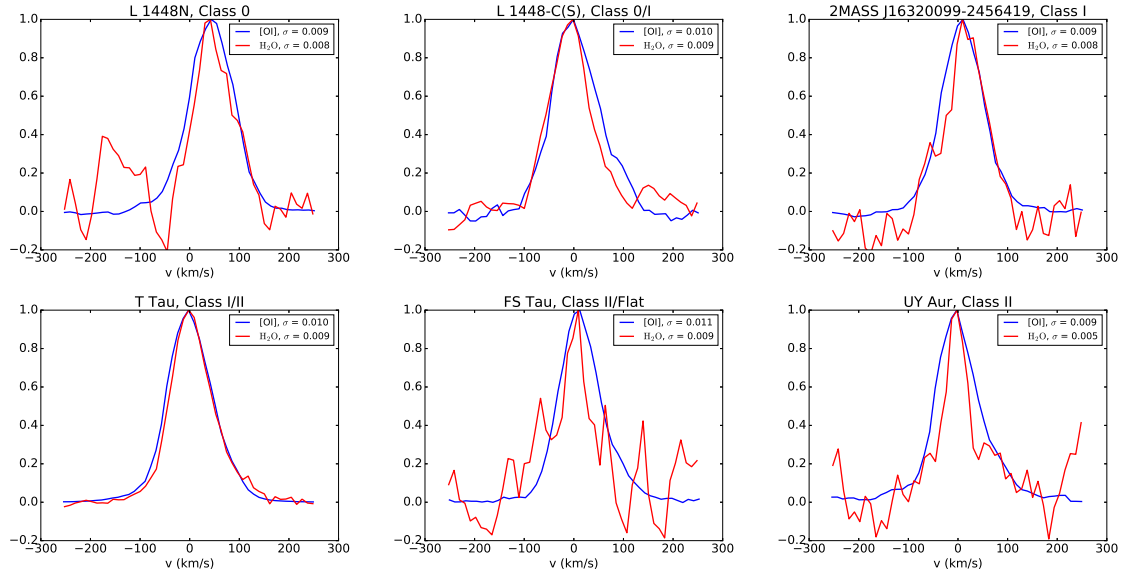


Fig. 12. Comparison of the [OI] and o-H₂O line profiles for sources whose [OI] profiles are better reproduced by multiple Gaussians. In the legends we show the measured σ of the Gaussian fits.

in the [OI] line is a contribution from jet emission associated with the source (Podio et al. 2012; Howard et al. 2013). The high-velocity components ($v_{\text{HVC}} \sim 100$ km/s) must be associated with jets, while the low-velocity ones (which might also be rest-frame velocity, due to the limited spectral resolution) can be associated with envelope and wind emission, as well as disc emission.

o-H₂O seems to be dominated by disc or envelope emission or compact jet emission, since extended emission is observed in only one Class I source, and the line profiles are consistent single Gaussians. However, we mostly detected water emission in jet sources, and therefore we cannot rule out that the emission originates at the base of the jet, and that the lack of multiple components is due to a low S/N in the observations presented here.

5.2. Correlations with continuum emission

Howard et al. (2013) studied [OI] emission in Taurus and found a correlation between [OI] line emission at 63 μ m and the continuum at the same wavelength. This correlation was later confirmed for other associations (Mathews et al. 2013; Riviere-Marichalar et al. 2015). We have extended the study to the entire sample of YSOs observed with PACS in spectroscopic mode. The resulting plot is shown in Fig. 14. The different sources are placed at different loci in the diagram. Class 0 and I sources show on average higher line fluxes for the same continuum level than Class II and transitional discs. Furthermore, transitional discs show also lower [OI] fluxes for the same level of continuum emission than Class II sources. Transitional discs are located in the lowest part of the diagram because theirs is the lowest [OI] emission for the same continuum level. Class II sources show intermediate [OI] fluxes, while the Class 0 and I sources show the highest flux levels for the same continuum.

The correlation between [OI] flux and the continuum flux at 63 μ m is different for jet and non-jet sources (Howard et al. 2013). Given the correlation between line emission and continuum emission at 63 μ m, we tested cor-

relations against continuum photometry at different wavelengths. We first started by retrieving WISE (Wright et al. 2010) magnitudes for sources in the sample, within a search radius of 2.6''. When testing the correlations, we only included sources belonging to associations with known distances, or belonging to known associations, to correct the fluxes and magnitudes for distance. All the fluxes were scaled to the distance to Taurus (140 pc), and the magnitudes were converted into absolute magnitudes. The resulting comparison is shown in Fig. 15. We observed clear correlations between the [OI] flux and WISE band 4 flux, but the correlation seems to vanish for WISE1, with a Spearman probability for the null hypothesis (i. e. that there is no correlation) that decreases from 3.4 μ m (WISE 1) to 22 μ m (WISE 4). However, the results change when only Class II sources are considered, and the correlation is present for all the WISE bands, with strong to very strong correlation coefficients in the range 0.7 to 0.8.

The scatter in the correlations has many contributions, such as instrumental uncertainties, scatter in distance within the same association, and different disc mass and geometry. Furthermore, jets and winds also contribute to the [OI] line flux, but not to the continuum, which increases the scatter. We observed clear correlations from 22 to 63 μ m. The fact that [OI] correlates with magnitudes at different IR wavelengths, and that the strength of the correlation increases with wavelength, and is more pronounced for Class II sources very likely indicates that dust at different temperatures and gas emission are related, which most likely points to a contribution from discs and envelopes. However, this is not the only interpretation. Sources accreting at higher rates will show brighter continuum emission at 63 μ m. If accretion is driving [OI] emission at 63 μ m, then sources with higher accretion rates will also show brighter [OI] emission at 63 μ m, explaining the correlation.

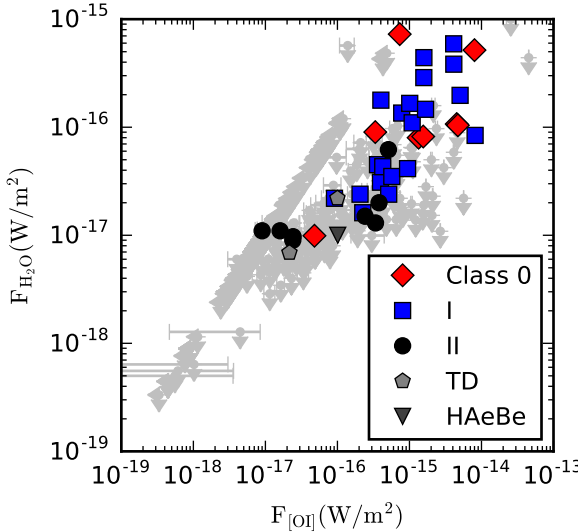


Fig. 13. o-H₂O line flux versus [OI] line flux at 63 μ m. Arrows show the positions of upper limits for non-detected sources. All fluxes have been scaled to the distance of Taurus.

5.3. Comparison with DENT models

To better understand the correlations, we compared our results with predictions from the DENT grid (Woitke et al. 2010; Kamp et al. 2011). The DENT grid consists of more than 3×10^5 models of protoplanetary discs that were developed to help in the interpretation of photometric and spectroscopic observations of protoplanetary discs for the GASPS program (Dent et al. 2013). The grid contains models representing different evolutionary stages. To restrict the number of models and interpret the results, we fixed $R_{\text{in}} = R_{\text{sub}}$ (where R_{sub} is the dust sublimation radius), $R_{\text{out}} = 300$ au, a surface mass density distribution power-law with index $\epsilon_0 = 1.0$, the gas-to-dust ratio to 100 and the minimum grain size to 0.05 μ m. We also excluded edge-on models ($i = 90^\circ$) and models with $\beta = 0.8$ (where β is the exponent of the scale height relation $H = H_0(r/r_0)^\beta$, leaving us with $\beta = 1.0$ and $\beta = 1.2$).

The DENT grid does not include continuum fluxes at 22 μ m, but at 24 μ m, so that this is what we show in Fig. 16. The difference in wavelength is so short that any effect on the shape of the correlation must be small. Owing to the limited parameter space covered by the DENT grid, the brightest sources are not covered by the models. The spearman probability (p) for the null hypothesis (i. e., that there is no correlation) is $p \ll 1.0^{-3}$ for the observations and for the models. We then fitted a straight line in the log-log space to the distributions of models and observations. The resulting fit has slope $m=0.72$ for the observational distribution, and $m=0.61$ for the distribution of models.

According to Woitke et al. (2010) the UV radiation field is one of the main drivers of [OI] emission, together with the flaring geometry and the total gas mass. To better understand the influence of these parameters on the [OI] flux distribution, we performed a more detailed analysis by fixing one of them at a time, and letting the other parameter free. The resulting comparison is shown in Fig. 16. For

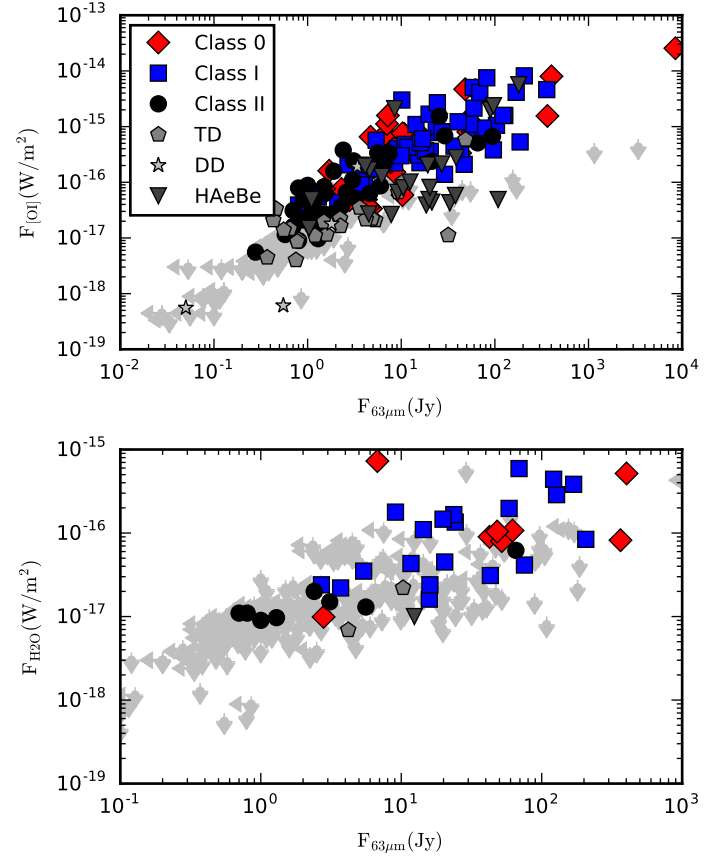


Fig. 14. [OI] (top) and o-H₂O (bottom) line fluxes versus continuum flux at 63 μ m for sources in the sample. Sources are labelled according to evolutionary stage. All the fluxes have been scaled to the distance to Taurus (140 pc). Arrows show the position of upper limits for non-detected sources.

$f_{\text{UV}} = 0.001$, only models with $\beta = 1.2$ can reproduce the observations. When $f_{\text{UV}} = 0.1$, models with $\beta = 1.2$ overestimate the flux for most of the observations. It is clear from the plots that we need intermediate values of both f_{UV} and β . However, extremely flared discs with low f_{UV} or flat discs with very high f_{UV} overlap with the observations. Overall, DENT models provide a good description of [OI] emission at 63 μ m for Class II sources. This shows that observations of Class II sources are compatible with pure protoplanetary disc models. Furthermore, the DENT models do not include jets or outflows, but they describe the emission well. The theoretical prediction by Woitke et al. (2010) that in a disc f_{UV} and β control [OI] emission is therefore compatible with our observations. We conclude that disc models provide an explanation for the correlations, but other solutions cannot be excluded.

5.4. Origin of line emission

In a study of molecular and atomic emission towards HH 46, van Kempen et al. (2010b) showed that the bulk of [OI] emission comes from low-velocity gas, after the impact of

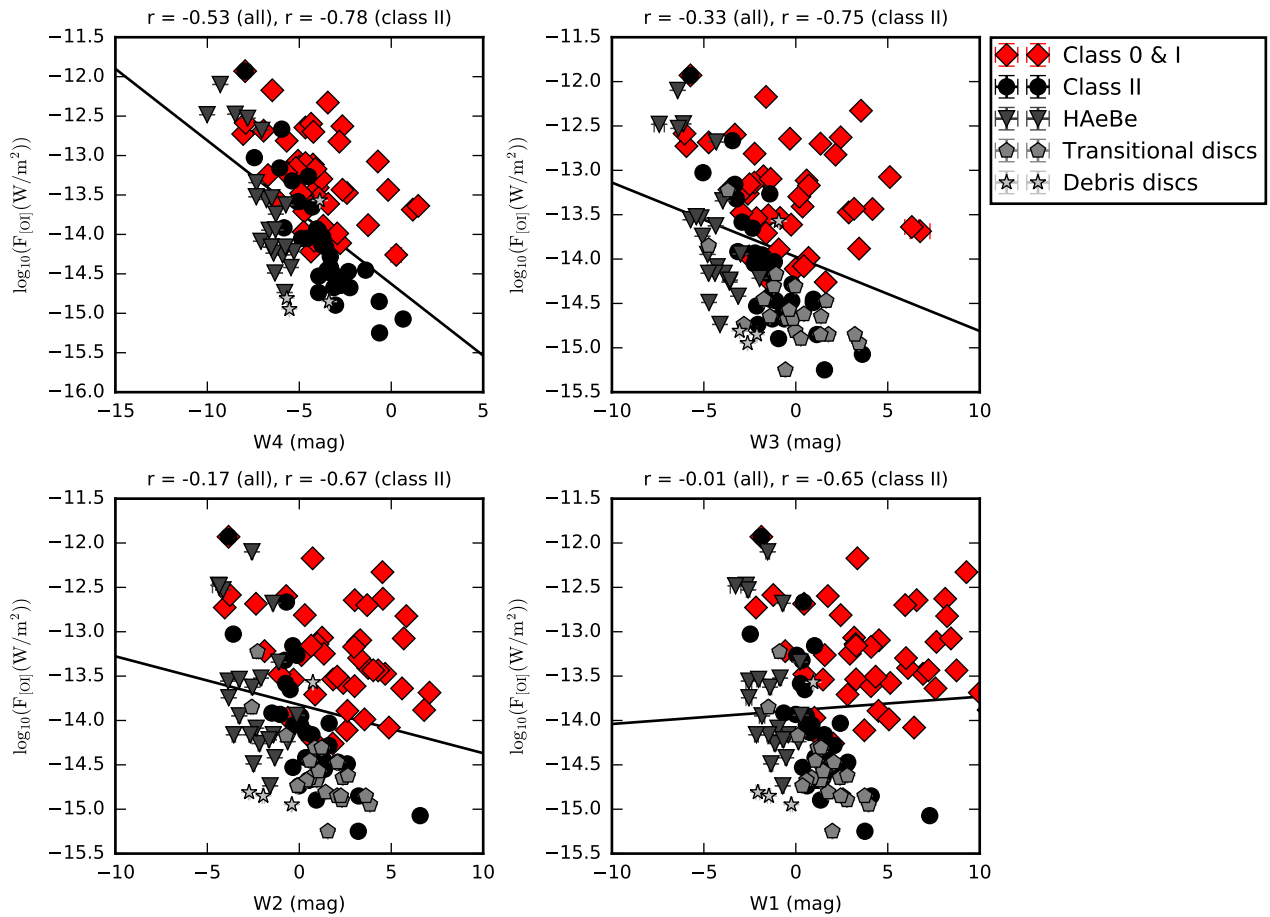


Fig. 15. [OI] fluxes at 63 μ m versus WISE magnitudes. All the fluxes have been scaled to the distance to Taurus. Magnitudes are corrected for distance. Spearman correlation coefficients are shown at the top of each plot.

high-velocity jets in the cavity walls. The authors also concluded that the high-velocity component observed in the central and outer spaxels originates in fast dissociative shocks in the lower density jet. Podio et al. (2012) demonstrated that atomic [OI] and [CII] line emission were extended and correlated with the direction of optical jets, and proposed that the extended atomic emission could be produced by J-shocks. Karska et al. (2013) studied a sample of low-mass Class 0 and I YSO and concluded that [OI] emission at 63 μ m originates in dissociative shocks. The authors also distinguished two groups of sources with extended emission, based on morphological differences: a compact group, where [OI] and OH emission dominates the central spaxel, while CO and H₂O can follow the same trend or are dominated by off-source emission, and an extended group, where OH off-source emission is strong. Class 0 sources dominate the extended group while Class 0 and I are equally represented in the compact group. The ratios of [OI] line emission at 63 and 145 μ m computed by Lee et al. (2014) for six low-mass embedded sources in Taurus were consistent with an origin in C-shocks, and again the authors highlighted that atomic emission is commonly extended along the jet direction. Additional support for a jet origin comes from Nisini et al. (2015), where the very similar profiles shown by [OI] and [FeII] towards LDN 1448N were highlighted. The authors were able to separate the

contributions from the different dynamical components in a few favourable cases, and observed an increment in [OI] velocity with distance from the central source, in agreement with observations of SiO.

In the present paper we have studied the spatial distribution of [OI] line emission towards 110 Class 0 and I sources, and detected hints of extended emission in at least 60 of them ($55\% \pm 5$). When separated by groups (see Fig. 8), we found a slightly larger extended emission fraction for Class 0 ($0.63^{+0.07}_{-0.08}$) than for Class I (0.51 ± 0.07), although they are compatible within the errors. The fraction then dramatically decreases for Class II sources (0.17 ± 0.08 , where we included Class II, both HAeBe and T Tauri, and transitional discs). We interpret this as a clear evidence that extended emission in Class 0, I, and II sources is due to shocks along the jet direction, in agreement with the results discussed in the previous paragraph, and that outflow activity drops with age.

Additional evidence for a jet contribution comes from the fact that 30 sources needed multiple Gaussians to fit the line profile. The reason for the low number is that only the most favorable cases will result in broad complex profiles because of the limited spectral resolution of PACS. Therefore, it is clearly established that extended emission is due to a jet contribution, and that at least part of the

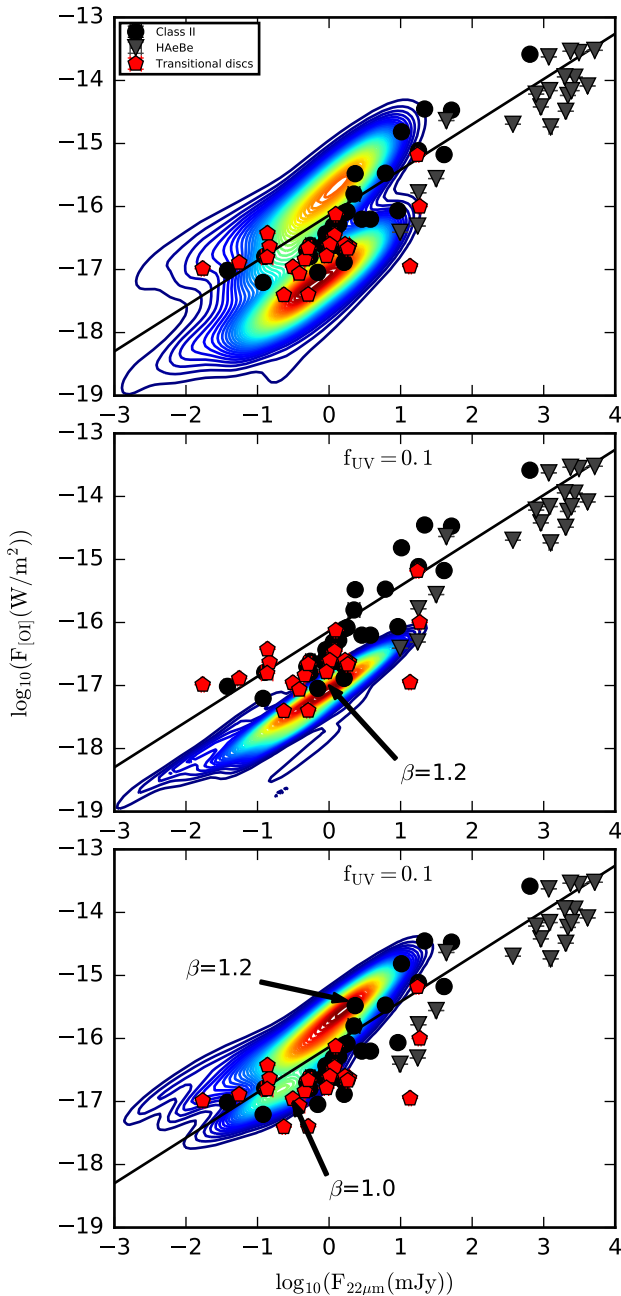


Fig. 16. [OI] fluxes at 63 μ m versus WISE flux at 22 μ m: observations compared to models. The contours show the density of points for models from the DENT grid. Black dots show the position of observed Class II sources, red pentagons are transitional discs, and grey triangles are HAeBe stars. The top panel shows the whole distribution of selected models. The middle panel shows the distribution of models with $f_{UV} = 0.1$, while the bottom panel shows models with $f_{UV} = 0.001$. The arrows point to the location of sources with different values of β . The solid line is a linear fit to the observed data.

compact emission is also due to shocks at the base of the jet, near the compact source.

However, various authors explained [OI] emission in Class II sources solely by means of disc emission (see, e.

g. Thi et al. 2010; Woitke et al. 2011; Meeus et al. 2010; Thi et al. 2013, 2014; Tilling et al. 2012, , among others). Early results by Mathews et al. (2010) ruled out an outflow shock origin for the [OI] line emission observed towards HD 169142 and showed that TWA 01 and RECX 15 observations required extreme outflowing fractions to explain [OI] emission through outflow activity. Furthermore, the authors highlight edthat there is no evidence of outflows in these sources, and the spectral profiles for RECX 15 and TWA 01 are not resolved, precluding the presence of jets with line-of-sight velocities higher than 45 km s⁻¹. Gorti et al. (2011) modelled in detail a large set of emission lines towards TWA 01, from UV to radio emission, and concluded that [OI] line emission comes from a region that covers almost the whole disc (30–120 au). The comparison of [OI] line emission versus continuum emission at 63 μ m performed by Howard et al. (2013) for Taurus sources leads to different loci for jet sources and sources without known jets. Jet sources show fluxes up to 20 times larger than than the non-jet sources. Furthermore, the authors discussed that transitional discs show even fainter fluxes, a trend that was confirmed by Keane et al. (2014), who studied [OI] emission in 17 transitional discs and demonstrated that they show weaker emission than full Class II discs, tentatively attributing the difference to flatter and/or less massive transitional discs compared to full ones.

In Sect. 5.3 we have shown that radiative transfer models of protoplanetary discs can explain [OI] emission in Class II sources, adding evidence for a disc contribution. Gorti & Hollenbach (2008) showed that [OI] emission can be emitted by the surface of protoplanetary discs at all radii. Protoplanetary disc modelling of HAeBe stars by Kamp et al. (2010) predicted [OI] emitting regions extending from 30 to 100 au. Correlations between line emission and the continuum emission from 4.6 to 63 μ m shown in Sect. 5.2 argue in favour of an extended emitting region, and for similar spatial origins for the line and continuum emission, additionally supporting the likeliness of a disc contribution. Transitional discs in Fig. 14 lie in the lower envelope of the cloud of points. We consider that they probably represent the real disc contribution, since no strong jet activity is expected in these sources.

Overall, there is strong observational evidence supporting contributions from both the jet (in Class 0, I and II sources) and the disc (Class II sources), while van Kempen et al. (2010b) ruled out a contribution from the passively heated envelope present in Class 0 and I sources.

6. Summary and conclusions

We have compiled *Herschel*-PACS observations of [OI] and o-H₂O at 63 μ m in YSOs, including Class 0, I, II, transitional discs, and debris discs, for a total of 432 observations of 362 sources.

We note that the [OI] emission line intensity, as well as detection fractions, decreases during the evolution from Class 0 to debris discs. However, we did not see a difference in [OI] emission between Class 0 and Class I, nor between Class II and transition discs. o-H₂O emission line intensity also decreases from Class 0 and I to more evolved sources (Class II and transition discs).

By means of comparing the fluxes computed from the central spaxel, the central 3x3 spaxels and the integrated IFU, we detected extended emission in the [OI] line for

a total of 77 sources. For those sources showing hints of extended [OI] emission, we obtained line emission maps and residual maps, and confirmed residual emission in 71 sources. The fraction of sources showing extended emission decreases dramatically from Class 0, where 63% of the sources show extended emission, to Class II, where only 17% of the sources show extended emission.

We detected extended o-H₂O line emission in only one source.

For 30 sources in the sample we were able to fit multiple components to the line emission profile, which is indicative of different contributions to the line (envelope, discs, winds, and jets).

We have tested previously identified correlations in the entire sample. The [OI] line emission correlates with continuum emission at 63 μ m for all classes, with the exception of debris discs.

We confirm the correlation between [OI] and o-H₂O at 63 μ m, and tentatively see a change in slope in the correlation between class 0 and I sources and class II sources.

We have identified new correlations with continuum emission between 4.6 and 22 μ m, indicating an extended emitting region (from the inner disc to tens of au) as the origin of the disc contribution.

Acknowledgements. The authors would like to thank the anonymous referee for a very fruitful discussion that helped to improve the quality of the paper. P.R.M. acknowledges funding from the ESA Research Fellowship program. C.E. and B.M. are partly supported by Spanish Grant AYA 2014-55840-P.

References

- Alcalá, J. M., Natta, A., Manara, C. F., et al. 2014, A&A, 561, A2
 Andre, P., Ward-Thompson, D., & Barsony, M. 1993, ApJ, 406, 122
 Bouvier, J. & Appenzeller, I. 1992, A&AS, 92, 481
 Bouy, H. & Martín, E. L. 2009, A&A, 504, 981
 Carpenter, J. M., Mamajek, E. E., Hillenbrand, L. A., & Meyer, M. R. 2006, ApJ, 651, L49
 Comerón, F. 2008, The Lupus Clouds, ed. B. Reipurth, 295
 de la Reza, R., Torres, C. A. O., Quast, G., Castilho, B. V., & Vieira, G. L. 1989, ApJ, 343, L61
 de Zeeuw, P. T., Hoogerwerf, R., de Bruijne, J. H. J., Brown, A. G. A., & Blaauw, A. 1999, AJ, 117, 354
 Dent, W. R. F., Thi, W. F., Kamp, I., et al. 2013, PASP, 125, 477
 Donaldson, J. K., Roberge, A., Chen, C. H., et al. 2012, ApJ, 753, 147
 Dzib, S., Loinard, L., Mioduszewski, A. J., et al. 2010, ApJ, 718, 610
 Erickson, K. L., Wilking, B. A., Meyer, M. R., Robinson, J. G., & Stephenson, L. N. 2011, AJ, 142, 140
 Fedele, D., Bruderer, S., van Dishoeck, E. F., et al. 2013, A&A, 559, A77
 Feigelson, E. D. & Babu, J. G. 2012, Modern Statistical Methods for Astronomy
 Furlan, E., Watson, D. M., McClure, M. K., et al. 2009, ApJ, 703, 1964
 Gorti, U. & Hollenbach, D. 2008, ApJ, 683, 287
 Gorti, U., Hollenbach, D., Najita, J., & Pascucci, I. 2011, ApJ, 735, 90
 Gray, R. O., Corbally, C. J., Garrison, R. F., et al. 2006, AJ, 132, 161
 Green, J. D., Evans, II, N. J., Jørgensen, J. K., et al. 2013, ApJ, 770, 123
 Gregorio-Hetem, J., Lepine, J. R. D., Quast, G. R., Torres, C. A. O., & de La Reza, R. 1992, AJ, 103, 549
 Hales, A. S., De Gregorio-Monsalvo, I., Montesinos, B., et al. 2014, AJ, 148, 47
 Harlan, E. A. 1974, AJ, 79, 682
 Herczeg, G. J., Karska, A., Bruderer, S., et al. 2012, A&A, 540, A84
 Hirota, T., Bushimata, T., Choi, Y. K., et al. 2008, PASJ, 60, 37
 Houk, N. 1978, Michigan catalogue of two-dimensional spectral types for the HD stars
 Houk, N. 1982, Michigan Catalogue of Two-dimensional Spectral Types for the HD stars. Volume_3. Declinations -40_deg0 to -26_deg0.
 Houk, N. & Cowley, A. P. 1975, University of Michigan Catalogue of two-dimensional spectral types for the HD stars. Volume I. Declinations -90_ to -53.deg0.
 Houk, N. & Smith-Moore, M. 1988, Michigan Catalogue of Two-dimensional Spectral Types for the HD Stars. Volume 4, Declinations -26deg.0 to -12deg.0.
 Houk, N. & Swift, C. 1999, in Michigan Spectral Survey, Ann Arbor, Dep. Astron., Univ. Michigan, Vol. 5, p. 0 (1999), Vol. 5, 0
 Howard, C. D., Sandell, G., Vacca, W. D., et al. 2013, ApJ, 776, 21
 Hughes, J., Hartigan, P., Krautter, J., & Kelemen, J. 1994, AJ, 108, 1071
 Kamp, I., Tilling, I., Woitke, P., Thi, W.-F., & Hogerheijde, M. 2010, A&A, 510, A18
 Kamp, I., Woitke, P., Pinte, C., et al. 2011, A&A, 532, A85
 Karska, A., Herczeg, G. J., van Dishoeck, E. F., et al. 2013, A&A, 552, A141
 Karska, A., Herpin, F., Bruderer, S., et al. 2014a, A&A, 562, A45
 Karska, A., Kristensen, L. E., van Dishoeck, E. F., et al. 2014b, A&A, 572, A9
 Keane, J. T., Pascucci, I., Espaillat, C., et al. 2014, ApJ, 787, 153
 Kenyon, S. J., Gómez, M., & Whitney, B. A. 2008, Low Mass Star Formation in the Taurus-Auriga Clouds, ed. B. Reipurth, 405
 Köhler, R., Kunkel, M., Leinert, C., & Zinnecker, H. 2000, A&A, 356, 541
 Kraemer, K. E., Jackson, J. M., & Lane, A. P. 1998, ApJ, 503, 785
 Kraus, A. L., Ireland, M. J., Martinache, F., & Lloyd, J. P. 2008, ApJ, 679, 762
 Lada, C. J. 1987, in IAU Symposium, Vol. 115, Star Forming Regions, ed. M. Peimbert & J. Jugaku, 1-17
 Lada, C. J. & Wilking, B. A. 1984, ApJ, 287, 610
 Lebreton, J., Augereau, J.-C., Thi, W.-F., et al. 2012, A&A, 539, A17
 Lee, J.-E., Lee, J., Lee, S., Evans, II, N. J., & Green, J. D. 2014, ApJS, 214, 21
 Levenhagen, R. S. & Leister, N. V. 2006, MNRAS, 371, 252
 Lindberg, J. E., Jørgensen, J. K., Green, J. D., et al. 2014, A&A, 565, A29
 López Martí, B., Jiménez-Estebar, F., & Solano, E. 2011, A&A, 529, A108
 Luhman, K. L. 2004, ApJ, 602, 816
 Luhman, K. L. 2007, ApJS, 173, 104
 Luhman, K. L. 2008, Chamaeleon, ed. B. Reipurth, 169
 Luhman, K. L., Allen, P. R., Espaillat, C., Hartmann, L., & Calvet, N. 2010, ApJS, 186, 111
 Mamajek, E. E., Lawson, W. A., & Feigelson, E. D. 1999, ApJ, 516, L77
 Manoj, P., Bhatt, H. C., Maheswar, G., & Muneer, S. 2006, ApJ, 653, 657
 Marsh, K. A., Silverstone, M. D., Becklin, E. E., et al. 2002, ApJ, 573, 425
 Martin, E. L., Montmerle, T., Gregorio-Hetem, J., & Casanova, S. 1998, MNRAS, 300, 733
 Mathews, G. S., Dent, W. R. F., Williams, J. P., et al. 2010, A&A, 518, L127
 Mathews, G. S., Pinte, C., Duchêne, G., Williams, J. P., & Ménard, F. 2013, A&A, 558, A66
 McClure, M. K., Furlan, E., Manoj, P., et al. 2010, ApJS, 188, 75
 Meeus, G., Pinte, C., Woitke, P., et al. 2010, A&A, 518, L124
 Meeus, G., Salyk, C., Bruderer, S., et al. 2013, A&A, 559, A84
 Melnick, G. J., Tolls, V., Neufeld, D. A., et al. 2008, ApJ, 683, 876
 Mendigutía, I., Calvet, N., Montesinos, B., et al. 2011, A&A, 535, A99
 Mohanty, S., Greaves, J., Mortlock, D., et al. 2013, ApJ, 773, 168
 Mora, A., Merín, B., Solano, E., et al. 2001, A&A, 378, 116
 Mortier, A., Oliveira, I., & van Dishoeck, E. F. 2011, MNRAS, 418, 1194
 Neuhauser, R. & Forbrich, J. 2008, The Corona Australis Star Forming Region, ed. B. Reipurth, 735
 Nilsson, R., Liseau, R., Brandeker, A., et al. 2009, A&A, 508, 1057
 Nisini, B., Santangelo, G., Antonucci, S., et al. 2013, A&A, 549, A16
 Nisini, B., Santangelo, G., Giannini, T., et al. 2015, ApJ, 801, 121
 Pilbratt, G. L., Riedinger, J. R., Passvogel, T., et al. 2010, A&A, 518, L1+
 Podio, L., Kamp, I., Flower, D., et al. 2012, A&A, 545, A44
 Poglitsch, A., Waelkens, C., Geis, N., et al. 2010, A&A, 518, L2
 Prato, L., Greene, T. P., & Simon, M. 2003, ApJ, 584, 853
 Preibisch, T., Brown, A. G. A., Bridges, T., Guenther, E., &

Table 4. Fitted parameters for [OI] lines with multiple components

Source	peak ₀ (Jy)	$\lambda_{0,0}$ (μ m)	v ₀ (km/s)	σ_0 (μ m)	peak ₁ (Jy)	$\lambda_{0,1}$ (μ m)	v ₁ (km/s)	σ_1 (μ m)	peak ₂ (Jy)	$\lambda_{0,2}$ (μ m)	v ₂ (km/s)	σ_2 (μ m)
T Tau	15.52	63.159	-123	0.0074	309.76	63.182	-14	0.0075	209.03	63.19	24	0.0101
FS Tau*	16.15	63.183	-10	0.007	7.78	63.189	19	0.0122	0.0	0.0	0.0	0.0
DG Tau*	17.62	63.181	-20	0.0072	14.3	63.182	-13	0.0149	0.0	0.0	0.0	0.0
HL Tau*	25.11	63.197	55	0.0083	3.92	63.185	0.0	0.0279	0.0	0.0	0.0	0.0
TMR 1	2.58	63.156	-189	0.012	10.36	63.203	85	0.0185	0.0	0.0	0.0	0.0
UY Aur*	12.77	63.183	-10	0.0065	8.03	63.188	16	0.0133	0.0	0.0	0.0	0.0
AB Aur*	40.46	63.182	-15	0.0071	9.42	63.194	41	0.0074	0.0	0.0	0.0	0.0
HD 50138	3.33	63.144	-197	0.0083	68.75	63.179	-30	0.015	10.94	63.214	137	0.0077
R Mon	4.03	63.139	-219	0.004	61.89	63.180	-22	0.0154	14.22	63.212	126	0.0099
HD 97048*	77.27	63.192	33	0.0074	19.49	63.19	25	0.0116	0.0	0.0	0.0	0.0
T 42	9.73	63.169	-77	0.0051	12.6	63.191	28	0.0164	0.0	0.0	0.0	0.0
WW Cha	12.38	63.178	-35	0.013	5.16	63.207	105	0.0121	0.0	0.0	0.0	0.0
HD 100546	149.42	63.184	-7	0.0155	66.07	63.210	121	0.008	0.0	0.0	0.0	0.0
chaii-j12531723-7707107	53.95	63.163	-105	0.0103	74.84	63.187	8	0.0095	14.92	63.213	131	0.013
GSS30 IRS1	3.91	63.142	-206	0.0152	28.76	63.184	-4	0.0137	31.69	63.203	88	0.0178
Elias 29	7.58	63.166	-89	0.0044	48.41	63.186	3	0.0198	0.0	0.0	0.0	0.0
RCrA IRS5A	14.33	63.167	-86	0.0117	51.29	63.198	61	0.0157	0.0	0.0	0.0	0.0
RCrA IRS7C	23.05	63.166	-90	0.004	197.92	63.188	12	0.0211	36.5	63.206	99	0.0086
RCrA IRS7B	4.96	63.233	227	0.0961	79.13	63.187	10	0.0203	55.44	63.210	119	0.0128
Re 50 NN IRS*	45.99	63.184	-5	0.010	9.20	63.200	71	0.014	0.0	0.0	0.0	0.0
Cra01	3.64	63.164	-100	0.005	68.61	63.190	24	0.011	0.0	0.0	0.0	0.0
2MASS J16320099-2456419*	57.10	63.189	19	0.00829	8.63	63.192	33	0.014	0.0	0.0	0.0	0.0
[MAM2011] W40-MM5*	27.13	63.183	-9	0.0075	25.13	63.194	43	0.00827	0.0	0.0	0.0	0.0
IRAS 04325+2402*	32.15	63.185	0	0.0074	2.98	63.20	71	0.003	0.0	0.0	0.0	0.0
L1448-C(S)*	28.29	63.186	5	0.0088	5.60	63.204	90	0.0069	0.0	0.0	0.0	0.0
LDN 1448N*	82.94	63.189	19	0.0090	8.08	63.184	-5	0.015	0.0	0.0	0.0	0.0
SMM J032537+30451*	41.18	63.188	14	0.008	50.41	63.185	0	0.012	0.0	0.0	0.0	0.0
VELA IRS 17	375.22	63.190	24	0.099	108.50	63.197	57	0.005	3.84	63.218	157	0.0078
Serpens-SMM3	19.00	63.155	-142	0.0093	24.18	63.189	19	0.011	11.52	63.218	157	0.0077
Serpens-SMM1a*	29.68	63.182	-14	0.016	144.41	63.190	24	0.0091	7.60	63.210	119	0.0076
2MASS J23134531+6128116	225.25	63.168	-81	0.010	2205	63.175	-47	0.0099	1.38	63.197	57	0.024
IRAS 11590-6452	15.54	63.160	-119	0.0083	5051	63.182	-14	0.010	3.99	63.187	9	0.029

Notes. (*): the velocity separation between the components is smaller than the spectral resolution (~ 88 km/s).

- Zinnecker, H. 2002, AJ, 124, 404
Preibisch, T., Guenther, E., Zinnecker, H., et al. 1998, A&A, 333, 619
Ricci, L., Testi, L., Natta, A., & Brooks, K. J. 2010, A&A, 521, A66
Riviere-Marichalar, P., Barrado, D., Augereau, J.-C., et al. 2012a, A&A, 546, L8
Riviere-Marichalar, P., Barrado, D., Montesinos, B., et al. 2014, A&A, 565, A68
Riviere-Marichalar, P., Bayo, A., Kamp, I., et al. 2015, A&A, 575, A19
Riviere-Marichalar, P., Ménard, F., Thi, W. F., et al. 2012b, A&A, 538, L3
Riviere-Marichalar, P., Pinte, C., Barrado, D., et al. 2013, A&A, 555, A67
Rydgren, A. E. 1980, AJ, 85, 444
Spezzi, L., Alcalá, J. M., Covino, E., et al. 2008, ApJ, 680, 1295
Strom, K. M., Strom, S. E., Edwards, S., Cabrit, S., & Skrutskie, M. F. 1989, AJ, 97, 1451
Sturm, B., Bouwman, J., Henning, T., et al. 2010, A&A, 518, L129
Thi, W.-F., Mathews, G., Ménard, F., et al. 2010, A&A, 518, L125
Thi, W. F., Ménard, F., Meeus, G., et al. 2013, A&A, 557, A111
Thi, W.-F., Pinte, C., Pantin, E., et al. 2014, A&A, 561, A50
Tilling, I., Woitke, P., Meeus, G., et al. 2012, A&A, 538, A20
Torres, C. A. O., Quast, G. R., da Silva, L., et al. 2006, A&A, 460, 695
Vacca, W. D. & Sandell, G. 2011, ApJ, 732, 8
van Dishoeck, E. F., Kristensen, L. E., Benz, A. O., et al. 2011, PASP, 123, 138
van Kempen, T. A., Green, J. D., Evans, N. J., et al. 2010a, A&A, 518, L128
van Kempen, T. A., Kristensen, L. E., Herczeg, G. J., et al. 2010b, A&A, 518, L121
Vieira, S. L. A., Corradi, W. J. B., Alencar, S. H. P., et al. 2003, AJ, 126, 2971
Webb, R. A., Zuckerman, B., Platais, I., et al. 1999, ApJ, 512, L63
Weinberger, A. J., Becklin, E. E., Zuckerman, B., & Song, I. 2004, AJ, 127, 2246
Wichmann, R., Krautter, J., Covino, E., et al. 1997, A&A, 320, 185
Wilking, B. A., Gagné, M., & Allen, L. E. 2008, Star Formation in the ρ Ophiuchi Molecular Cloud, ed. B. Reipurth, 351
Woitke, P., Pinte, C., Tilling, I., et al. 2010, MNRAS, 405, L26
Woitke, P., Riaz, B., Duchêne, G., et al. 2011, A&A, 534, A44

Wright, E. L., Eisenhardt, P. R. M., Mainzer, A. K., et al. 2010, AJ, 140, 1868
Zuckerman, B. & Song, I. 2004a, ApJ, 603, 738
Zuckerman, B. & Song, I. 2004b, ARA&A, 42, 685

Appendix A: Line emission maps

Appendix B: Residual line emission maps

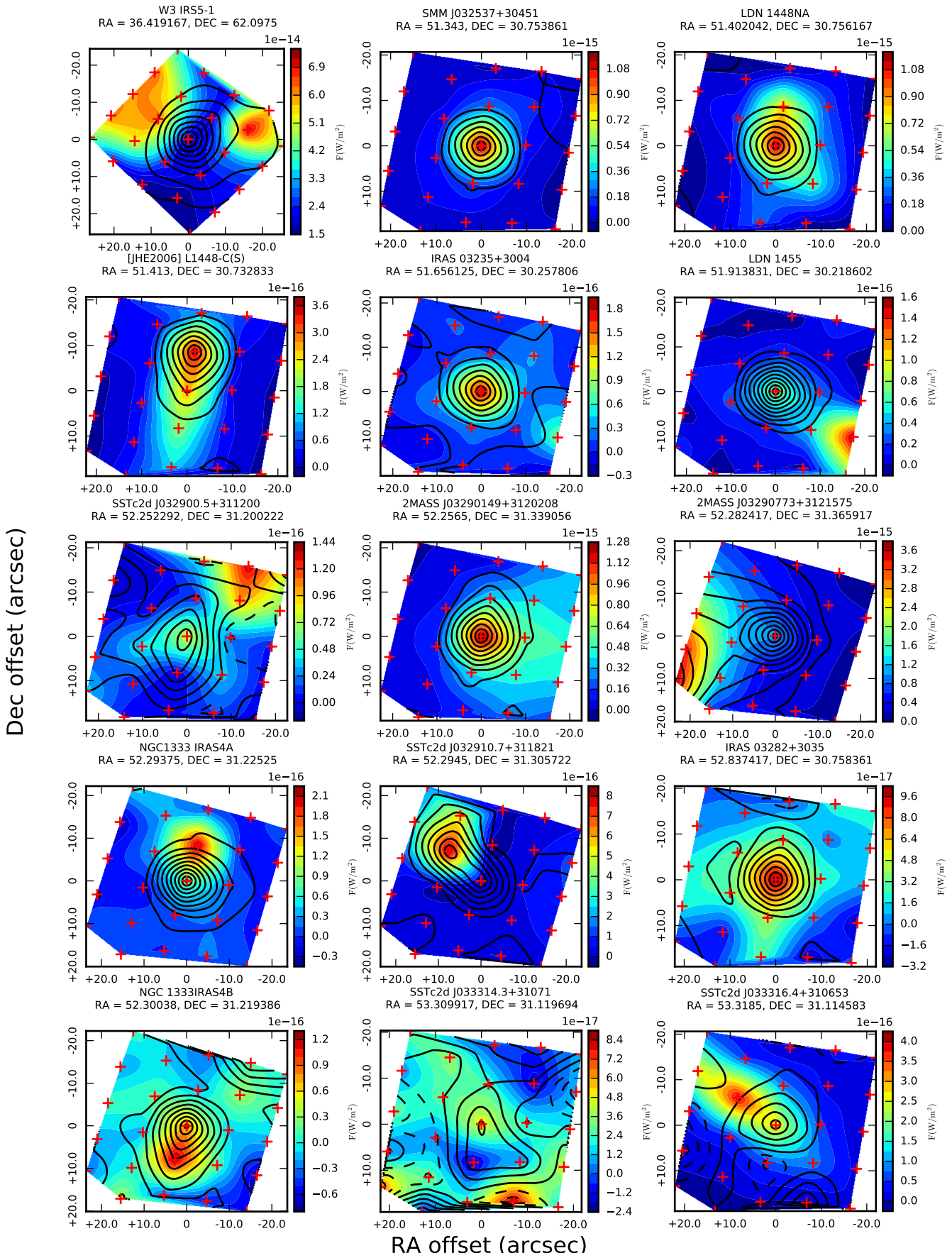


Fig. A.1. [OI] line emission at 63 μ m (coloured contours) and 63 μ m continuum contours (solid black lines) for sources identified as extended by any of the three tests used. The positions of spaxels are marked with red plus signs.

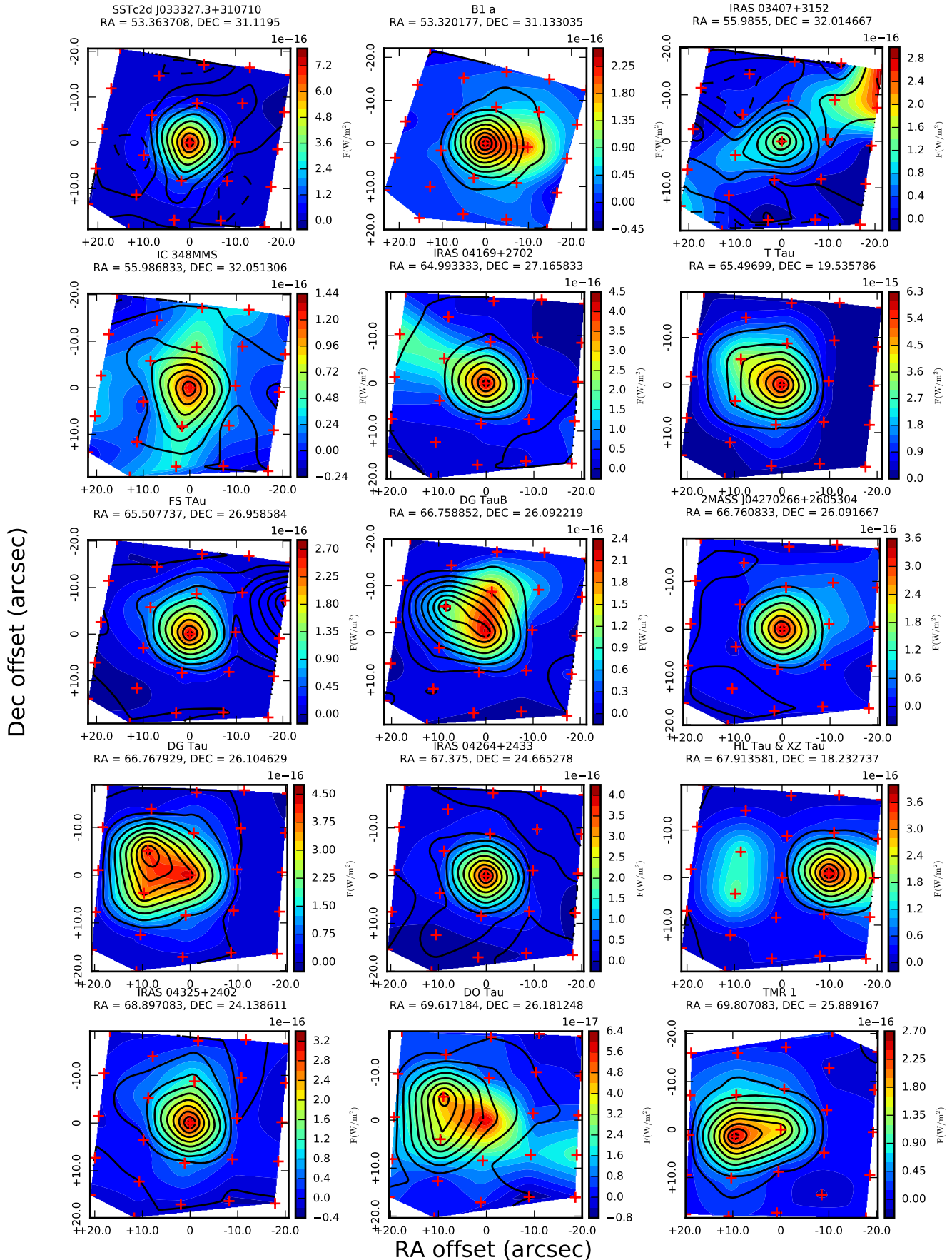


Fig. A.1. continued.

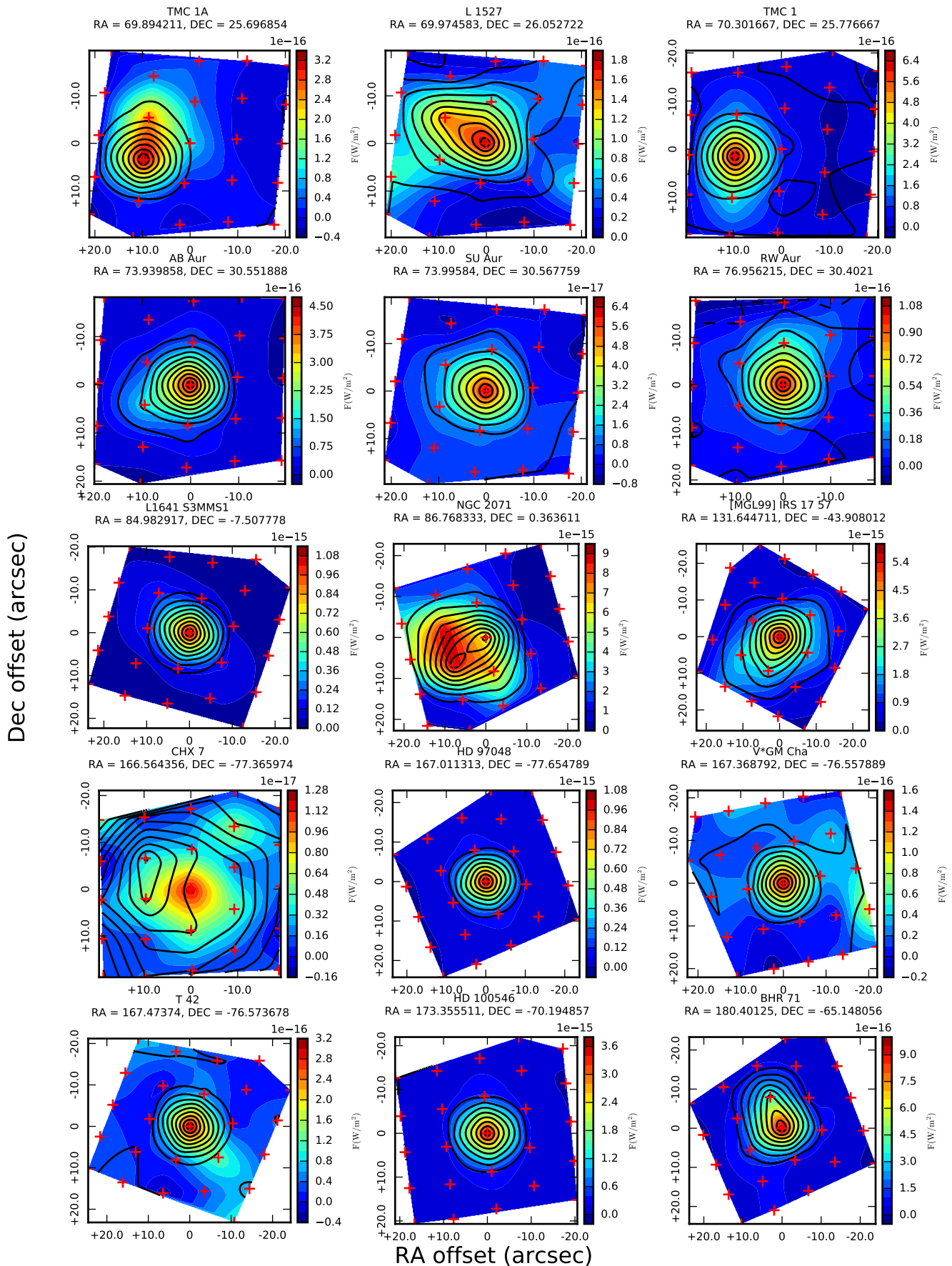
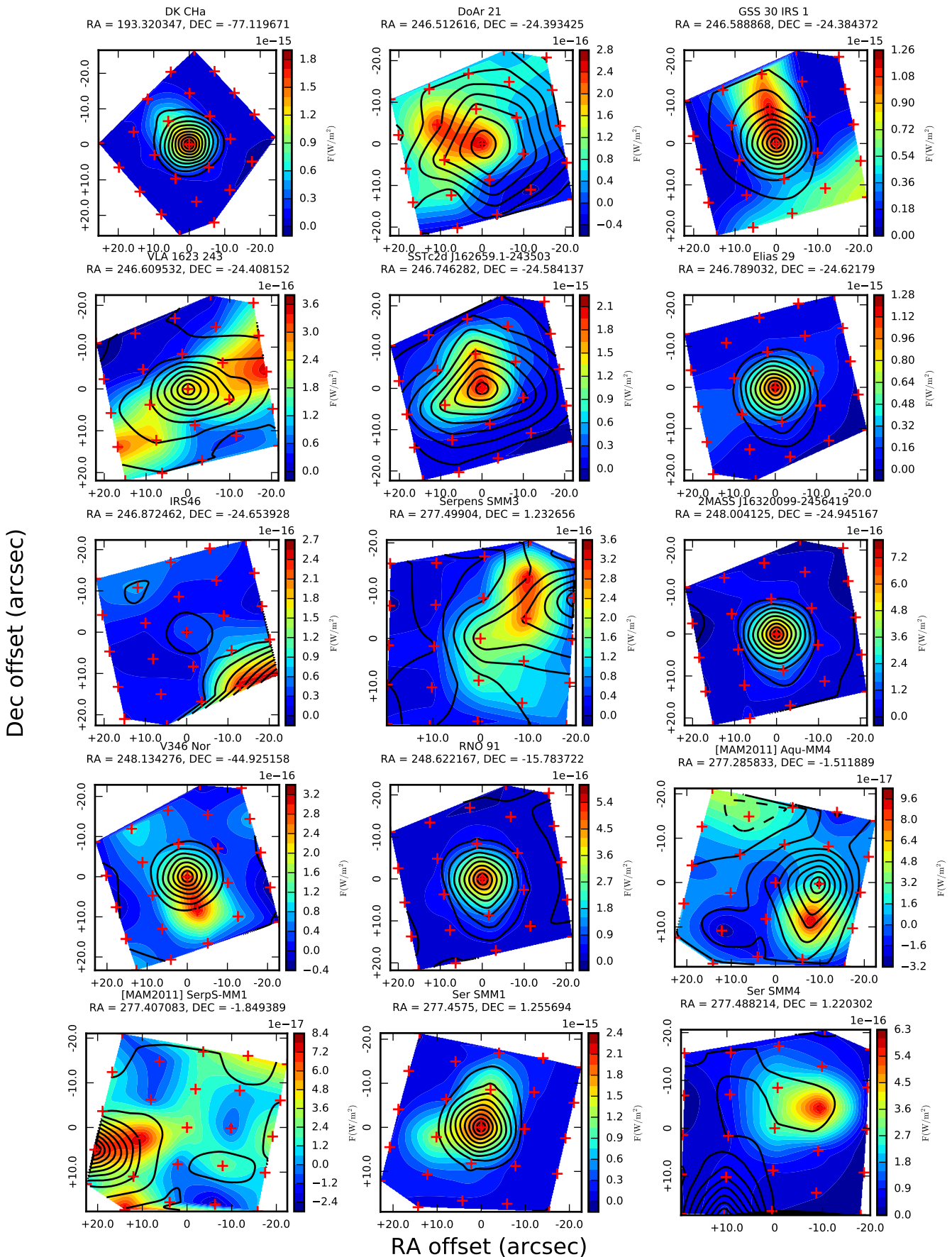


Fig. A.1. continued.


Fig. A.1. continued.

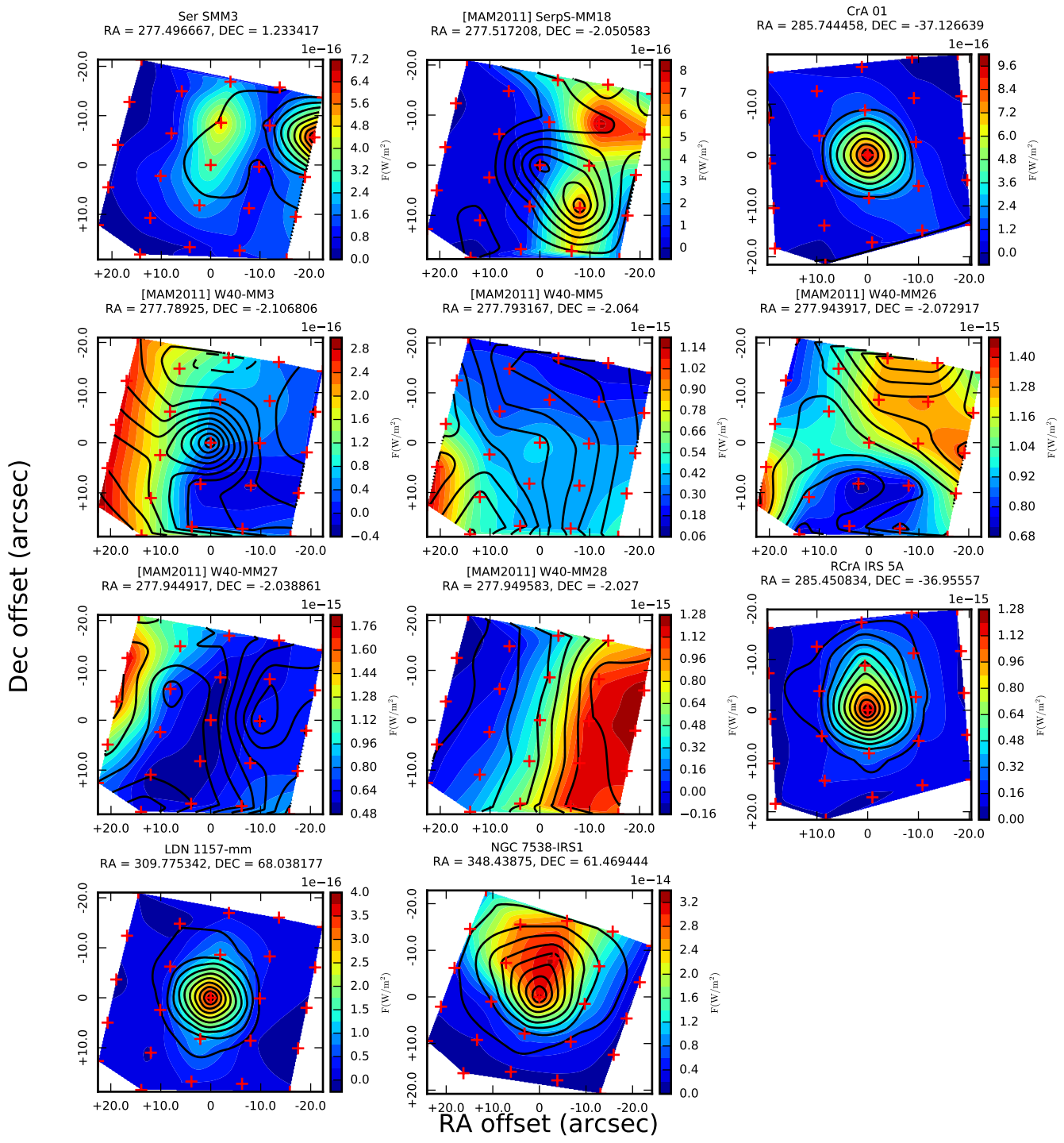


Fig. A.1. continued.

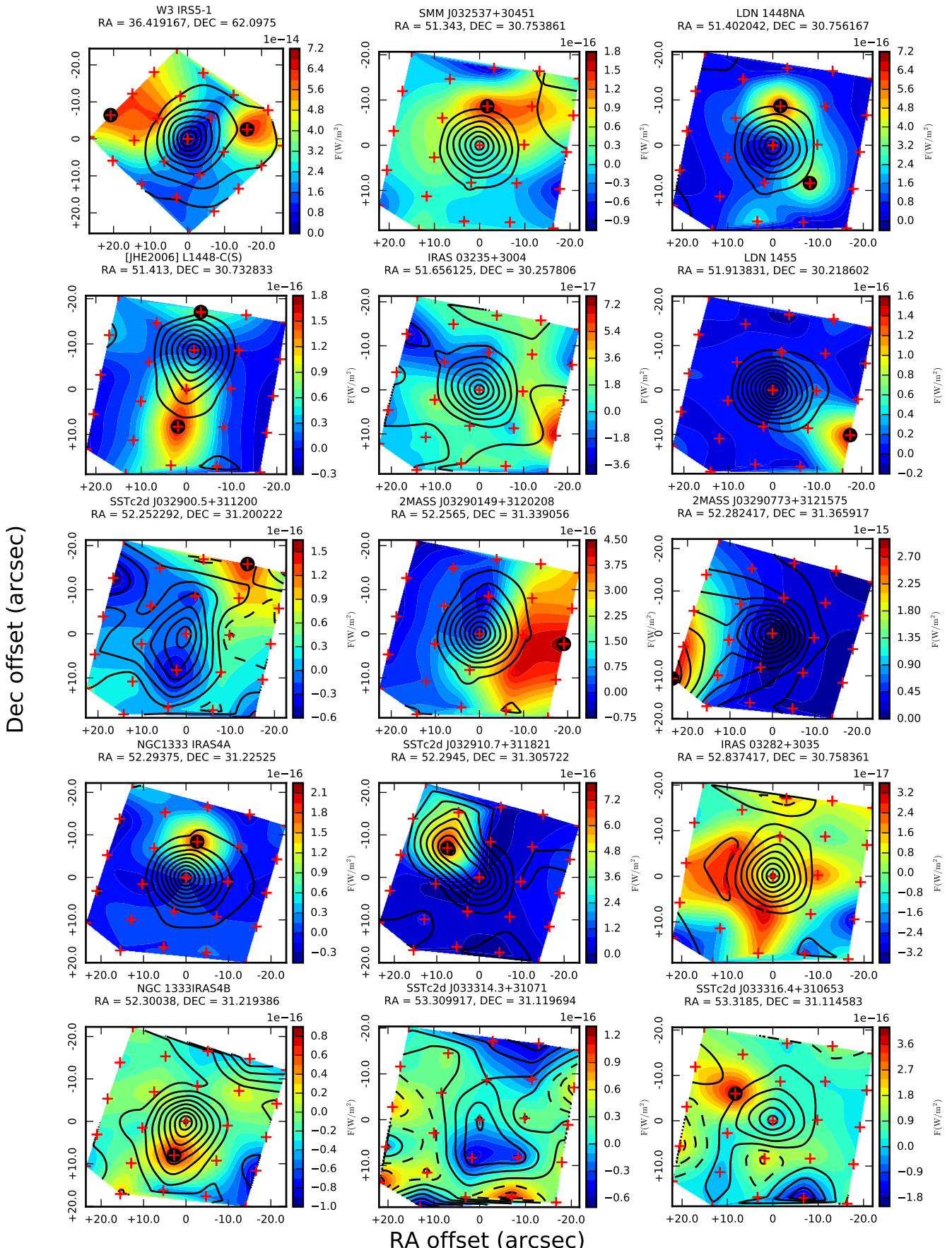


Fig. B.1. [OI] residual line emission at 63 μ m (coloured contours) and 63 μ m continuum contours (solid black lines) for sources identified as extended by any of the three tests used. The positions of spaxels with 5 σ residual detections are surrounded by black dots.

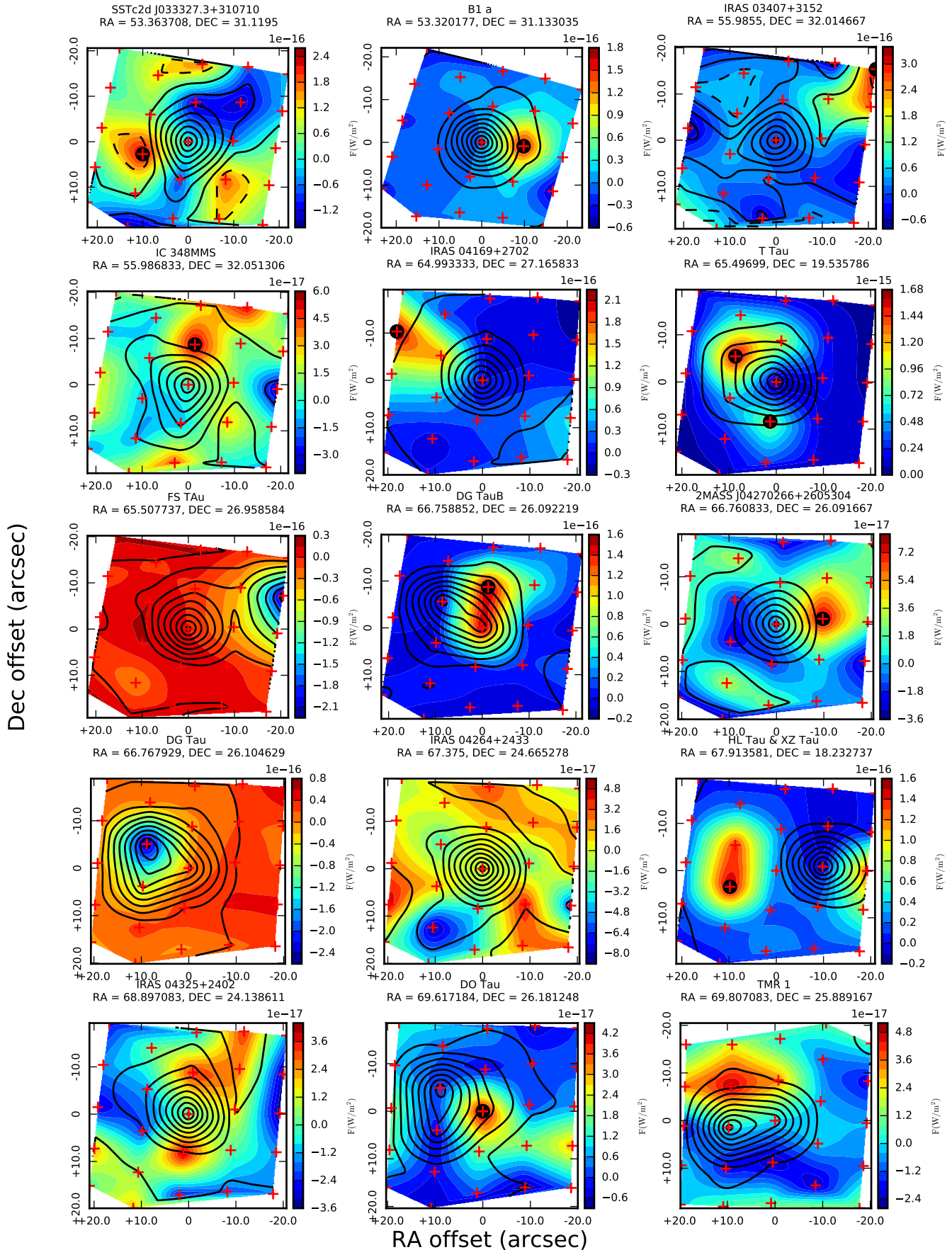


Fig. B.1. continued.

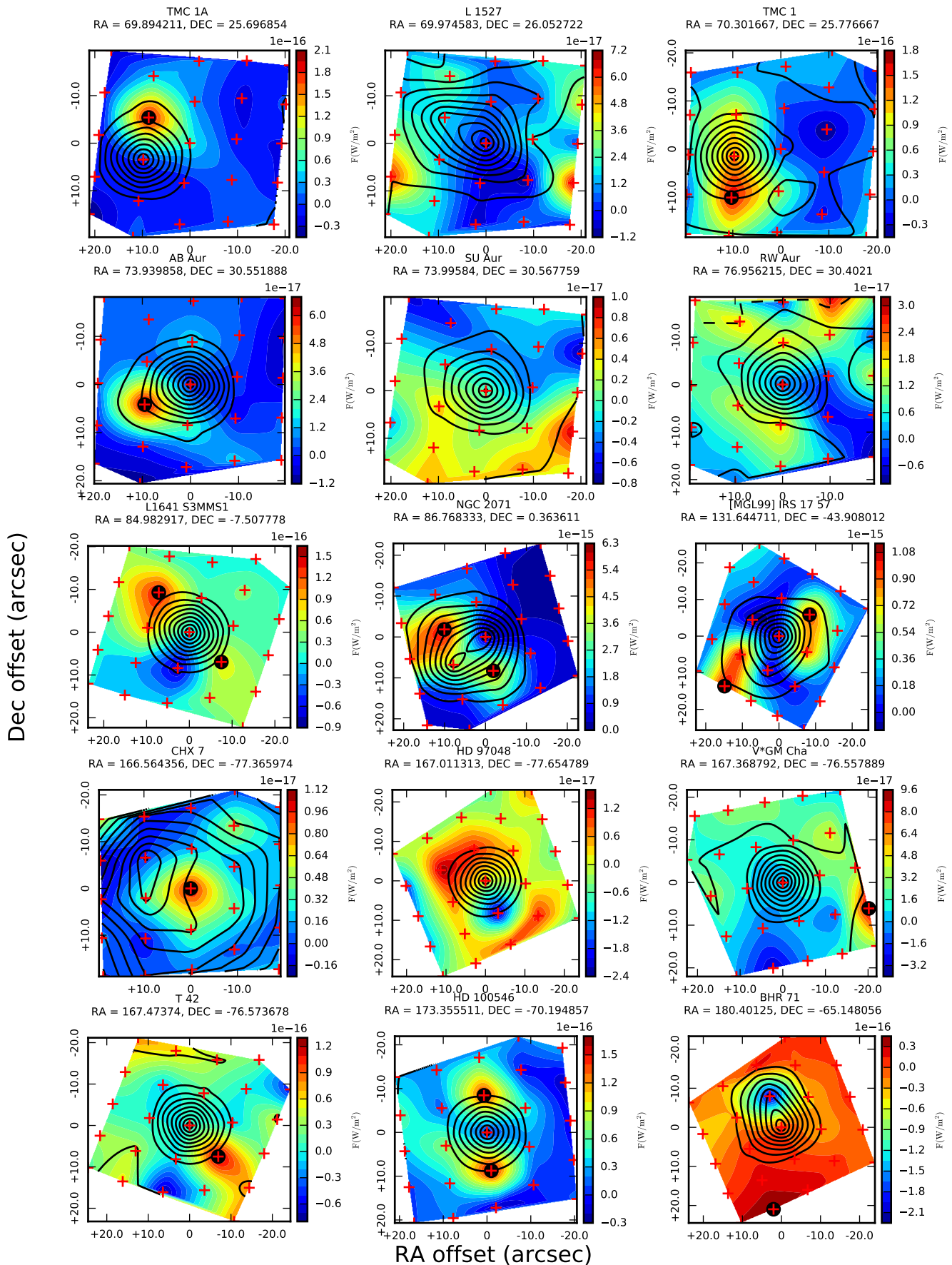


Fig. B.1. continued.

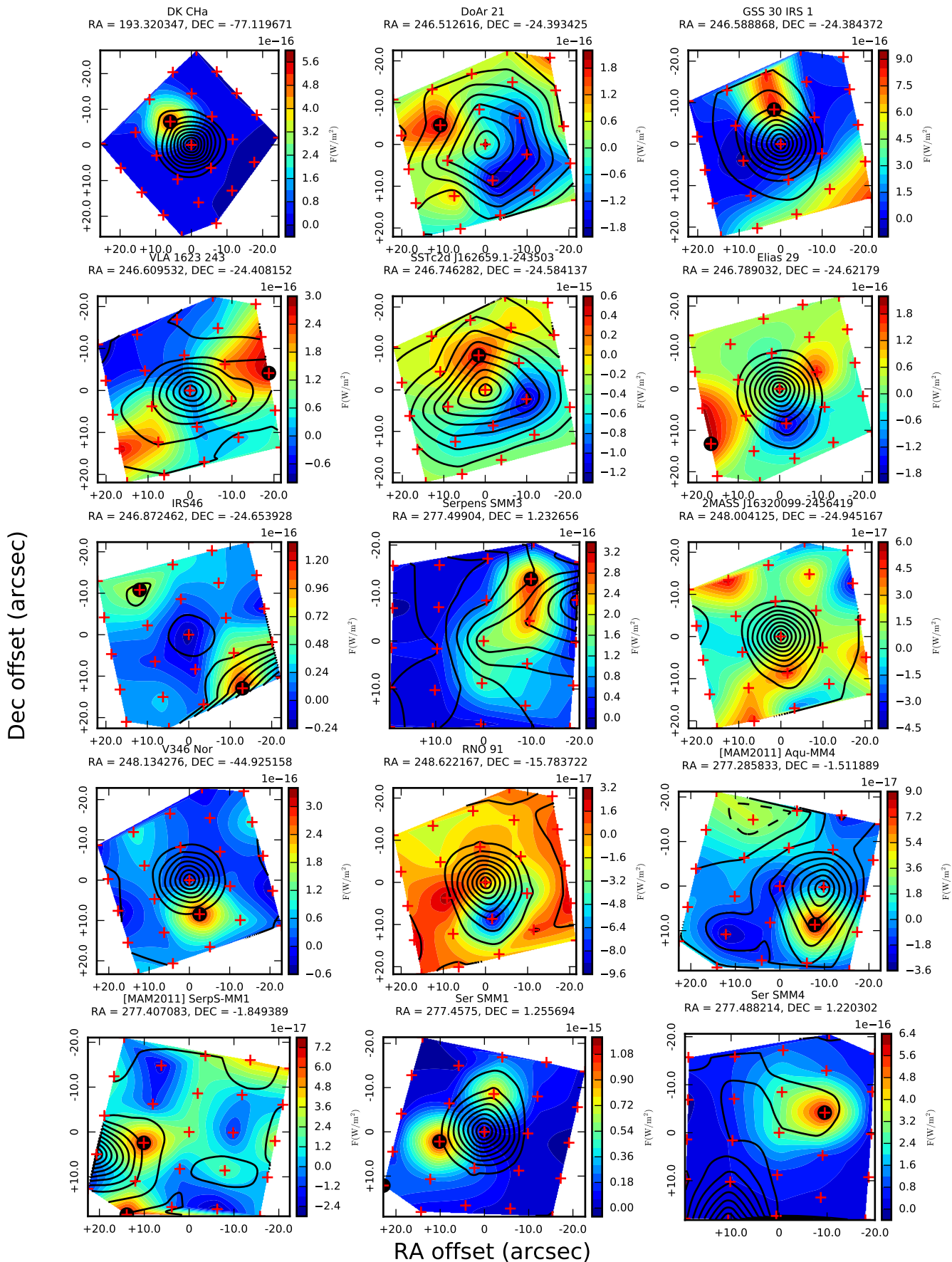


Fig. B.1. continued.

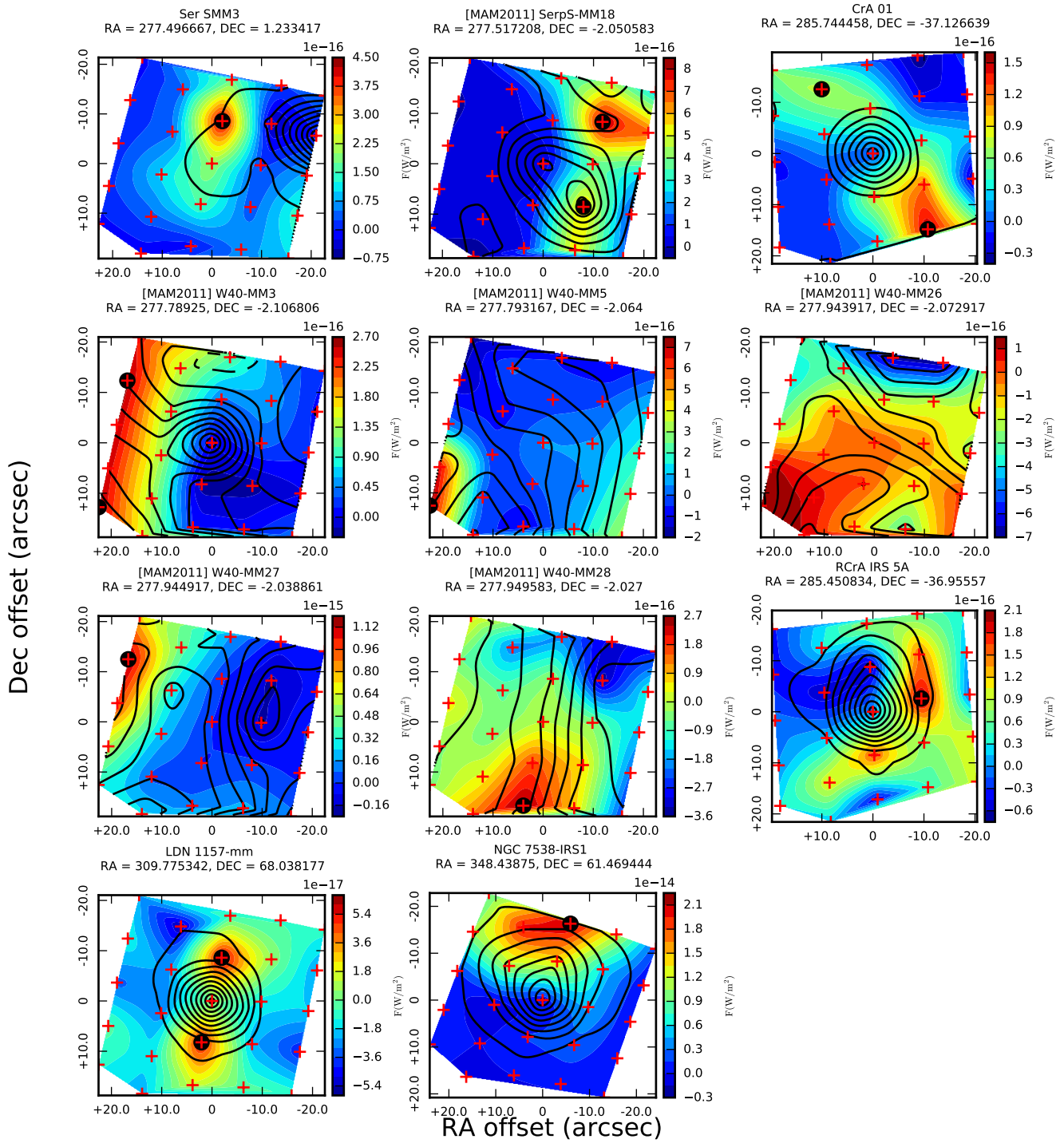


Fig. B.1. continued.

Table B.1. Sample of YSOs observed with *Herschel*-PACS

Source name	RA (deg)	Dec (deg)	Sp. type ¹	Disc type	Association
HD 105	1.468958	-41.753067	G0 ¹	DD	TucHor
HD 377	2.107291	6.616806	G2 ¹	DD	-
HD 3003	8.182958	-63.0315	A0 ²	DD	TucHor
HD 3670	9.736267	-52.534284	F5 ²	DD	-
HD 9672	23.657412	-15.676359	A1 ³	DD	Argus
tau Ceti	26.017	-15.937472	G8.5 ⁴	DD	-
W3 IRS5	36.419125	62.097361	-	0	-
HD 15115	36.567667	6.292556	F4 ⁵	DD	-
HD 16743	39.781511	-52.934806	F1 ²	DD	-
SMM J032537+30451	51.343	30.75386	-	0	Per
LDN 1448N	51.40204	30.75616	-	0	Per
L 1448-C(S)	51.413	30.73283	-	0/I	Per
IRAS 03235+3004	51.65612	30.25780	-	0	Per
L 1455	52.0167	30.1733	-	0	Per
2MASS J03283706+3113310	52.15454	31.22522	-	I	Per
SSTc2d J032857.4+311416	52.239	31.23775	-	I	Per
SSTc2d J032900.5+311200	52.25229	31.20022	-	I	Per
2MASS J03290149+3120208	52.2565	31.33905	-	I	Per
2MASS J03290773+3121575	52.28241	31.36591	-	I	Per
NGC 1333IRAS4A	52.293708	31.22527	-	0	Per
SSTc2dJ 032910.7+311821	52.2945	31.30572	-	0	Per
NGC 1333IRAS4B	52.300042	31.21894	-	0	Per
SSTc2d J032912.0+311301	52.30025	31.21713	-	0	Per
SSTc2d J032913.5+311358	52.30641	31.23283	-	0	Per
HBC 347	52.409875	24.510556	K1 ⁶	III	Taurus
LDN 1455 IRS3	52.001711	30.133690	-	0/I	-
IRAS 03267+3128	52.46591	31.65166	-	0	Per
IRAS 03271+3013	52.56308	30.39705	-	I	Per
IRAS 03282+3035	52.83741	30.75836	-	0	Per
HD 21997	52.973542	-25.614139	A3 ³	DD	-
IRAS 03292+3039	53.07483	30.82986	-	0	Per
epsilon Eri	53.232667	-9.45825	K2 ⁴	DD	-
IRAS 03301+3111	53.303333	31.356722	-	I	Per
SSTc2d J033314.3+310710	53.30991	31.11969	-	0	Per
SSTc2d J033316.4+310653	53.3185	31.11458	-	0	Per
B1-a	53.319583	31.132	-	I	Per
B1-c	53.32437	31.15886	-	0/I	Per
SSTc2d J033327.3+310710	53.3637	31.1195	-	I	Per
IRAS 03407+3152	55.9855	32.01466	-	0	Per
SSTc2d J034356.8+320305	55.98683	32.05130	-	0	Per
2MASS J03444389+3201373	56.18316	32.02672	-	0	Per
LkHa 330	56.45117	32.40331	G2	TD	Per
HBC 356	60.808292	25.883306	K2 ⁶	III	Taurus
HBC 358	60.961833	26.181444	M2 ⁶	III	Taurus
IRAS 04016+2610	61.1794625	26.315663	-	I	-
PP 13S	62.671458	38.132028	-	I	-
LkCa 1	63.308917	28.319678	M4 ⁶	III	Taurus
V1096 Tau	63.363458	28.273556	M0 ⁶	III	Taurus
V773 Tau	63.553833	28.203458	K3 ⁶	II	Taurus
FM Tau	63.556583	28.213667	M0 ⁶	II	Taurus
CW Tau	63.570833	28.182722	K3 ⁶	II	Taurus
CIDA 1	63.573375	28.102694	M5.5 ⁶	II	Taurus
CX Tau	63.699417	26.803058	M3 ⁶	TD	Taurus
LkCa 3	63.699875	27.876292	M1 ⁶	III	Taurus
FO Tau	63.705375	28.2085	M2 ⁶	T	Taurus
CIDA-2	63.7715	28.146167	M5.5 ⁶	III	Taurus
LkCa 4	64.117125	28.126614	K7 ⁶	III	Taurus
CY Tau	64.390542	28.346361	M1.5 ⁶	II	Taurus
LkCa 5	64.41225	28.550142	M2 ⁶	III	Taurus
IRAS 04158+2805	64.74225	28.206528	-	I	Taurus
FQ Tau	64.803375	28.492528	M3 ⁶	II	Taurus
BP Tau	64.815958	29.107472	K7 ⁶	II	Taurus
V819 Tau	64.859417	28.437306	K7 ⁶	II/III	Taurus
FR Tau	64.897708	28.456056	-	TD	Taurus
LkCa 7	64.921958	27.830136	K7 ⁶	III	Taurus
IRAS 04169+2702	64.99333	27.16583	-	I	Taurus
IRAS 04181+2654	65.2975	27.01916	-	I	Taurus
DE Tau	65.481833	27.918361	M1 ⁶	II	Taurus
IRAM 04191	65.487083	15.496083	-	0	-
RY Tau	65.489167	28.443206	K1 ⁶	TD	Taurus
HD 283572	65.495208	28.301844	G5 ⁶	III	Taurus
T Tau	65.497625	19.535103	M3 ⁶	I/II	Taurus

Table B.1. continued.

Source name	RA (deg)	Dec (deg)	Sp. type	Disc type	Association
–	–	–	–	–	–
2MASS J04220069+2657324	65.5025	26.95888	–	I	Taurus
FS Tau	65.509083	26.958472	M0 ⁶	II/Flat	Taurus
FS TauB	65.509071	26.958469	–	I	Taurus
FU Tau	65.8975	25.05075	M7.25 ⁶	II	Taurus
FT Tau	65.913292	24.93725	M3 ⁶	II	Taurus
IP Tau	66.237833	27.199028	M0 ⁶	TD	Taurus
J1-4872	66.323667	26.297336	K7/M1 ⁶	III	Taurus
F VTau	66.723042	26.115111	K5 ⁶	II	Taurus
DG TauB	66.760667	26.091861	–	I	Taurus
DF Tau	66.762833	25.706472	M2 ⁶	II	Taurus
DG Tau	66.769583	26.104528	K6 ⁶	II	Taurus
IRAS 04248+2612	66.98875	26.32166	–	I	Taurus
IRAS 04264+2433	67.375	24.66527	–	I	Taurus
FW Tau	67.373792	26.281444	M4 ⁶	III	Taurus
DH Tau	67.425083	26.548111	M2 ⁶	II	Taurus
IQ Tau	67.464833	26.112472	M0.5 ⁶	II	Taurus
CFHT 20	67.497958	24.552167	M5 ⁶	II	Taurus
UX Tau	67.516667	18.230389	K5 ⁶	TD	Taurus
FXTau	67.623375	24.445833	M1 ⁶	II	Taurus
DK Tau	67.684333	26.023556	K6 ⁶	II	Taurus
ZZ Tau	67.714083	24.706194	M3 ⁶	II	Taurus
ZZ TauIRS	67.715458	24.696528	M5 ⁶	II	Taurus
IRAS 04287+1801	67.891987	18.134694	–	I	Taurus
V927 Tau	67.84925	24.181369	M4.7 ⁶	III	Taurus
HL Tau	67.9101	18.232681	K7 ⁶	II	Taurus
XZ Tau	67.9145	18.232139	M2 ⁶	II	Taurus
HK Tau	67.960708	24.405019	M0.5 ⁶	II	Taurus
V710 Tau	67.990833	18.35975	M0.5 ⁶	II	Taurus
Haro 6-13	68.064208	24.48325	M0 ⁶	II	Taurus
GG Tau	68.126458	17.527944	M5.5 ⁶	II	Taurus
UZ Tau	68.178458	25.875389	M1 ⁶	II	Taurus
GH Tau	68.276792	24.162361	M2 ⁶	II	Taurus
V807 Tau	68.277621	24.165278	K5 ⁶	II	Taurus
GI Tau	68.392958	24.353194	K7 ⁶	II	Taurus
GK Tau	68.394	24.351611	K7 ⁶	II	Taurus
DL Tau	68.41275	25.343944	K7 ⁶	II	Taurus
HN Tau	68.41395	17.86454	K5 ⁶	II	Taurus
DM Tau	68.453	18.169444	M1 ⁶	T	Taurus
CI Tau	68.466667	22.841722	K7 ⁶	II	Taurus
AA Tau	68.730917	24.481444	K7 ⁶	II	Taurus
HO Tau	68.834167	22.537389	M0.5 ⁶	II	Taurus
FF Tau	68.837083	22.906722	K7 ⁶	III	Taurus
DN Tau	68.864042	24.249694	M0 ⁶	TD	Taurus
IRAS 04325+2402	68.89708	24.13861	–	I	Taurus
HP Tau	68.969917	22.906417	K3 ⁶	II	Taurus
J04381486	69.561917	26.194417	M7.25 ⁶	II	Taurus
GM Tau	69.588917	26.153806	M6.5 ⁶	II	Taurus
DO Tau	69.619083	26.180389	M0 ⁶	II	Taurus
HV Tau	69.647	26.177397	–	I	Taurus
TMR 1B	69.807875	25.889	–	I	Taurus
TMR 1	69.807917	25.889056	–	I	Taurus
VY Tau	69.822542	22.798167	M0 ⁶	II	Taurus
LkCa 15	69.824167	22.350972	K5 ⁶	TD	Taurus
2MASS J04393364+2359212	69.890208	23.989222	M5 ⁶	II	Taurus
IRAS 04365+2535	69.89421	25.69685	–	I	Taurus
BD Tau4	69.947833	26.028	M7 ⁷	II	Taurus
L 1527	69.97458	26.0527	–	0	Taurus
IRAS 04381+2540	70.302708	25.77663	–	I	Taurus
CoKu Tau4	70.32	28.666833	M1.5 ⁶	II	Taurus
IRAS 04385+2550	70.41175	25.940778	M0 ⁶	II	Taurus
DP Tau	70.657083	25.260417	M0.5 ⁶	II	Taurus
GO Tau	70.762875	25.338556	M0 ⁶	II	Taurus
DQTau	71.721042	17.000056	M0 ⁶	II	Taurus
Haro6-37	71.74575	17.043944	K7 ⁶	II	Taurus
DS Tau	71.950458	29.420681	K5 ⁶	II	Taurus
UY Aur	72.947417	30.787083	M0 ⁶	II	Taurus
GM Aur	73.79575	30.366528	K7 ⁶	T	Taurus
AB Aur	73.940958	30.551214	B9 ⁶	II	Taurus
SU Aur	73.997417	30.5671	G2 ⁶	II	Taurus
HD 31648	74.692777	29.843611	A5 ⁸	HAeBe	–
HD 32297	75.614319	7.461022	A0 ¹	DD	–

Table B.1. continued.

Source name	RA (deg)	Dec (deg)	Sp. type	Disc type	Association
V836Tau	75.7775	25.388808	K7 ⁶	TD	Taurus
RW Aur	76.956417	30.401408	K3 ⁶	II	Taurus
HD 35187	81.004875	24.960444	A2+A7 ⁹	HAeBe	-
HD 35841	81.652442	-22.489923	F3 ³	DD	GAYA2
HD 36112	82.614707	25.332523	A5 ¹⁰	HAeBe	Taurus
HD 36910	83.993612	24.748359	F3 ¹⁰	HAeBe	Taurus
V833 Ori	84.575417	-7.040611	-	I	-
HD 245906	84.877	26.331972	A6 ⁹	II	-
[SMZ2000] L1643-S3MMS1	84.982917	-7.507778	-	0	-
Re50 NNIRS	85.114167	-7.458667	-	I	-
HD 38120	85.799542	-4.997194	B9 ¹¹	HAeBe	-
HD 38207	85.837331	-20.189297	F2 ³	DD	-
HD 38206	85.840293	-18.557475	A0 ³	DD	-
V1647 Ori	86.5547	-0.101333	-	I	-
HR 1998	86.73892	-14.82195	A2 ⁴	DD	-
NGC 2071IR	86.768333	0.36361	-	0	-
β Pic	86.821208	-51.066528	A6 ⁴	DD	BPMG
R Mon	99.791458	8.736028	B8 ⁴	HAeBe	-
HD 50138	102.889167	-6.9665	A1 ¹¹	HAeBe	-
PDS 27	109.89975	-17.655	B2 ¹²	HAeBe	-
HD 61005	113.94775	-32.203889	G8 ²	DD	-
Bran 76	117.648333	-33.106639	-	I	-
RECX 1	129.234292	-78.945972	K4 ¹³	III	EtaCha
RECX 14	130.37625	-78.885139	M4 ¹³	TD	EtaCha
RECX 3	130.404292	-79.058444	M3 ¹³	TD	EtaCha
RECX 4	130.598875	-79.0675	K7 ¹³	TD	EtaCha
RECX 5	130.612958	-78.963306	M5 ¹³	TD	EtaCha
RECX 6	130.661667	-78.911889	M2 ¹³	III	EtaCha
RECX 8	130.800958	-79.070083	A7 ²	III	EtaCha
RECX 15	130.827417	-79.088389	M2 ¹³	II	EtaCha
J0844.2-7833	131.038125	-78.562694	M5.5 ¹³	II	EtaCha
RECX 9	131.06825	-78.985583	M4 ¹³	TD	EtaCha
RECX 10	131.132833	-78.775333	K7 ¹³	III	EtaCha
[MGL99] IRS1757	131.644833	43.908472	-	I	-
RECX 11	131.756917	-78.992917	K4 ¹³	II	EtaCha
RECX 12	131.986542	-78.914778	M2 ¹³	III	EtaCha
TWA 07	160.625458	-33.671167	M1 ¹⁴	DD	TWA
SZ Cha	164.569875	-77.288083	K0 ¹⁵	TD	Cha
CR Cha	164.779125	-77.027889	K2 ¹⁶	TD	Cha
TWA 01	165.466333	-34.704722	M2.5 ¹⁷	TD	TWA
CS Cha	165.603792	-77.559917	K6 ¹⁶	TD	Cha
CHX 7	166.564208	-77.365806	G5 ¹	TD	Cha
Eso-HA 559	166.606458	-76.561639	M5 ¹⁸	TD	Chai
2MASS J11064658-7722325	166.694084	-77.375710	-	I	-
[NC98] Cha HA 1	166.8195	-77.598139	M8 ¹⁹	II	Chai
Sz 18	166.829792	-76.051333	M2.5 ¹⁹	TD	Cha
HD 97048	167.013833	-77.654861	A0 ¹⁰	HAeBe	Chai
HP Cha	167.062917	-77.564778	G7 ¹⁸	Flat	Chai
Sz 27	167.162708	-77.267833	K8 ¹⁸	TD	Chai
TWA 02AB	167.307542	-30.027722	M2 ¹	III	TWA
GM Cha	167.3687	-76.5578	-	I	Cha I
T42	167.472542	-76.57375	K4.7 ¹⁹	II	Chai
WW Cha	167.500458	-76.58275	K5 ¹⁸	TD	Chai
TWA 03A	167.616167	-37.531111	M3 ²⁰	TD	TWA
Hn 13	167.733208	-76.759056	M6 ¹⁹	II	Chai
CV Cha	168.1155	-76.739528	G9 ¹⁸	II	Chai
CHX 22	168.177875	-77.373056	G8 ¹⁸	TD	Chai
Sz 45	169.404208	-77.07725	M0.5 ¹⁹	TD	Chai
TWA13AB	170.321833	-34.779306	M1 ¹	III	TWA
HD 98800B	170.522083	-24.777583	M5 ²¹	DD/TD	TWA
HD 98922	170.631958	-53.369861	B9 ²²	HAeBe	-
HD 100453	173.27325	-54.324583	A9 ¹²	HAeBe	-
HD 100546	173.356	-70.194778	B9 ²³	HAeBe	Ass Sco OB 2-4
T Cha	179.306375	-79.35875	K0 ¹	TD	Cha
HD 104237	180.021167	-78.192944	A4 ¹⁰	HAeBe	-
IRAS 11590-6452	180.404583	-65.14833	-	0	-
TWA 23	181.864083	-32.783417	M1 ²⁴	III	TWA
MML 17	185.638458	-53.563611	G2	DD ¹	Ass Sco OB 2-4
TWA 10	188.767708	-41.610722	M2.5 ¹⁴	III	TWA
HR 4796A	189.004298	-39.869505	A0 ²⁵	DD	TWA
DK Cha	193.321792	-77.119639	-	I	ChaiII

Table B.1. continued.

Source name	RA (deg)	Dec (deg)	Sp. type	Disc type	Association
–	–	–	–	–	–
ChaII J125342.86-771511.5	193.428583	-77.253194	-	I	ChaII
ChaII J125633.66-764545.3	194.14025	-76.762583	M1 ²⁶	II	ChaII
ChaII J125711.77-764011.3	194.299042	-76.669806	M0 ²⁶	II	ChaII
ChaII J125806.78-770909.4	194.52825	-77.152611	M7 ²⁶	II	ChaII
2MASSJ12590656-7707401	194.7774	-77.1277	-	I	ChaII
ChaII J130055.36-771022.1	195.230667	-77.172806	M3 ²⁶	II	ChaII
ChaII J130158.94-775121.7	195.495583	-77.856028	K8.5 ²⁶	II	ChaII
ChaII J130222.85-773449.3	195.595208	-77.580361	M5 ²⁶	II	ChaII
ChaII J130424.92-775230.1	196.103833	-77.875028	M2.5 ²⁶	II	ChaII
Hn 24	196.232292	-77.66375	M0 ²⁶	TD	ChaII
ChaII J130508.53-773342.4	196.285542	-77.561778	M2.5 ²⁶	II	ChaII
ChaII J130512.69-773052.3	196.302875	-77.514528	M1 ²⁶	II	ChaII
ChaII J130520.68-773901.4	196.336167	-77.650389	K5 ²⁶	II	ChaII
ChaII J130521.66-773810.0	196.34025	-77.636111	–	II	ChaII
ChaII J130529.04-774140.1	196.371	-77.694472	–	II	ChaII
ChaII J130718.05-774052.9	196.825208	-77.681361	M4.5 ²⁶	II	ChaII
ChaII J130748.51-774121.4	196.952125	-77.689278	M2 ²⁶	II	ChaII
ChaII J130806.28-775505.2	197.026167	-77.918111	K5 ²⁶	II	ChaII
ChaII J130827.17-774323.2	197.113208	-77.723111	M4.5 ²⁶	II	ChaII
HD 114082	197.317467	-60.308347	F3 ²	DD	LCC
ChaII J130950.38-775723.9	197.459917	-77.956639	M2.5 ²⁶	II	ChaII
HD 131835	224.226958	-35.695472	A2 ²⁵	DD	–
SAO 206462	228.951831	-37.154452	F4 ¹⁰	HAeBe	–
HIP 76310	233.817125	-25.734167	A0 ³	DD	UpSco
HD 139614	235.19325	-42.498194	A7 ¹⁰	HAeBe	Ass Sco OB 2-3
HT Lup	236.303625	-34.291833	K3 ¹	II	LupusI
HD 141569	237.490625	-3.921222	B9.5 ¹¹	DD	MBM37
G327-0.6	238.286005	-54.616659	–	–	–
HIP 77911	238.673333	-22.76625	B9 ³	DD	UpSco
HD 142666	239.166763	-22.027781	A8 ³	HAeBe	AssScoOB2-2
HD 142527	239.174542	-42.323139	F6 ²²	HAeBe	–
RU Lup	239.176292	-37.820972	G5 ²⁷	II	LupusI
USco J155729.9-225843	239.374458	-22.978806	M4 ²⁸	II	UpSco
Sz 84	239.510542	-37.60075	M5 ²⁹	TD	Cha
USco J155829.8-231007	239.624292	-23.168722	M3 ²⁹	II	UpSco
RY Lup	239.868292	-40.364222	K4 ³⁰	II	Ass Sco OB 2-3
1RXS J160044.7-234330	240.18625	-23.725	M2 ³¹	II	UpSco
EX Lup	240.772875	-40.307056	–	I	Lupus III
USco J160357.6-203105	240.990292	-20.518222	K5 ³²	II	UpSco
USco J160357.9-194210	240.991417	-19.703028	M2 ²⁸	II	UpSco
USco J160421.7-213028	241.09025	-21.507889	K2 ³³	II	UpSco
J160532.1-193315	241.383958	-19.554444	M5 ²⁸	III	UpSco
USco J160545.4-202308	241.439458	-20.385583	M2 ²⁸	II	UpSco
USco J160600.6-195711	241.502625	-19.953056	M5 ³⁴	II	UpSco
Sco PMS31	241.5915	-19.479056	M0.5 ³⁴	II	UpSco
HD 144432	241.7415	-27.719389	A9 ²⁵	HAeBe	Ass Sco OB 2-2
Sz 91	241.798375	-39.063083	M0.5 ³⁵	TD	Lupus
UScoJ160823.2-193001	242.096667	-19.500278	K9	II	UpSco
HD 144668	242.142875	-39.105083	A1-A2 ²⁷	HAeBe	LupusIII
Sz 111	242.227875	-39.628639	M1.5 ³⁵	TD	Lupus
UScoJ160959.4-180009	242.49725	-18.002528	M4 ²⁸	II	UpSco
SST Lup	242.623333	-39.370833	M5 ³⁶	TD	Lupus
AS 205	242.880625	-18.640583	K5 ³⁷	II	UpSco
HIP 79439	243.183792	-19.502833	B9V ³	DD	UpSco
UScoJ 161411.0-230536	243.546167	-23.093389	K0 ³⁸	II	UpSco
USco J161420.2-190648	243.584583	-19.113361	K5 ³⁹	II	UpSco
RXJ 1615.3-3255	243.834292	-32.918083	K5 ⁴⁰	TD	Lupus
HIP 79878	244.567375	-28.041694	A0 ²⁵	DD	UpSco
HIP 80088	245.209292	-22.594083	A9 ³	DD	UpSco
2MASS J16230923-2417047	245.788458	-24.284639	G0 ⁴¹	TD	Oph
Doar 21	246.512596	-24.393344	K0 ⁴²	II	Oph
GSS 30-IRS1	246.589167	-24.384528	–	I	Oph
GSS 31	246.597417	-24.349917	K0 ⁴²	II	Oph
DoAr25	246.59867	-24.72053	K5 ⁴³	II	Oph
VLA 1623-243	246.61	-24.408333	–	0	Oph
WL 12	246.684167	-24.580111	–	I	Oph
DoAr 28	246.697583	-23.247833	K5 ⁴¹	TD	Oph
WL 2	246.702083	-24.477417	–	0/I	Oph
Oph 01	246.7462	-24.5842	–	I	Oph
Elias 29	246.789167	-24.621833	–	I	Oph
SR 21	246.792833	-24.320139	G3 ⁴³	TD	Oph

Table B.1. continued.

Source name	RA (deg)	Dec (deg)	Sp. type	Disc type	Association
IRS 44	246.8725	-24.654472	-	0/I	Oph
IRS 46	246.8725	-24.654472	-	0/I	Oph
IRS 48	246.904958	-24.509722	A0 ⁴⁴	HAeBe	Oph
GY 314	246.914292	-24.654306	M0 ⁴⁵	-	Oph
WSB 60	247.068792	-24.616111	M4 ⁴³	TD	Oph
DoAr 44	247.889417	-24.460361	K3 ⁴²	TD	Oph
IRS 63	247.898333	-24.024806	-	0/I	Oph
L1689 SNO2	247.967	-24.937667	-	I	Oph
16289-2457	247.978083	-25.056611	-	0/I	Oph
2MASS J16320099-2456419	248.0041	-24.9451	-	I	Oph
16293-2424	248.08775	-24.509944	-	0/I	Oph
V346 Nor	248.134125	-44.925194	-	I	-
RNO 90	248.538208	-15.804667	G5 ⁴³	II	Oph
HBC 650	248.62216	-15.78372	-	I	-
HD 150193	250.074667	-23.895889	A2 ¹⁰	HAeBe	Ass Sco OB 2-2
Sco 01	251.7427	-9.58883	-	I	-
KK Oph	257.533583	-27.255056	A6 ¹⁰	HAeBe	-
NGC 6334-I	260.222037	-35.78329	-	-	-
HD 158352	262.206895	0.330625	A7 ¹⁰	DD	-
HD 158643	262.853975	-23.962643	A0 ³	HAeBe	-
HD 163296	269.0887	-21.956078	A1 ⁸	HAeBe	-
HD 164249	270.764208	-51.649011	F5 ⁴⁶	DD	BPMG
W33A	273.662980	-17.868719	-	-	-
[SER2000] L483	274.37475	4.660917	-	0/I	-
HD 169142	276.124078	-29.780381	A7 ¹⁰	HAeBe	-
[MAM2011] Aqu-MM2	277.2659	-1.65041	-	0	Aqu
[MAM2011] Aqu-MM4	277.2858	-1.51188	-	0	Aqu
[MAM2011] SerpS-MM1	277.407	-1.84938	-	0	Ser
Serpens SMM1a	277.4575	1.25572	-	0	-
EC 82	277.487042	1.24625	-	0/I	Serpens
Serpens-SMM4	277.4882	1.220302	-	0	Serpens
Serpens-SMM3	277.497083	1.233806	-	0	Serpens
Serpens-SMM18	277.51721	-2.05058	-	0	Serpens
[MAM2011] Aqu-MM6	277.6045	-1.90372	-	0	Aqu
[MAM2011] Aqu-MM7	277.6192	-1.94658	-	0	Aqu
[MAM2011] Aqu-MM8	277.6209	-1.93483	-	0	Aqu
[MAM2011] Aqu-MM14	277.708	-1.93502	-	0	Aqu
[MAM2011] W40-MM3	277.7892	-2.10680	-	0	W40
[MAM2011] W40-MM5	277.7931	-2.06400	-	0	W40
[MAM2011] W40-MM26	277.9439	-2.07291	-	0	W40
[MAM2011] W40-MM27	277.9449	-2.03886	-	0	W40
[MAM2011] W40-MM28	277.9495	-2.027	-	0	W40
[MAM2011] W40-MM34	277.9885	-2.00769	-	0/I	W40
[MAM2011] W40-MM36	278.0556	-1.95822	-	0	W40
Vega	279.23475	38.783694	A0 ⁴	DD	-
HD 172555	281.362083	-64.871258	A5 ⁴	DD	BPMG
RXJ 18523-3700	283.072083	-37.003306	K7 ⁴⁷	DD	-
G34.26+0.15	283.328128	1.249232	-	-	-
SCra	285.285833	-36.955556	-	I	Cra
R CrA-IRS5A	285.450417	-36.956306	-	I	Cra
R CrA-IRS5N	285.451921	-36.954133	-	0	Cra
R CrA-IRS 7A	285.480417	-36.954722	-	-	Cra
SMM 1C	285.48042	-36.95464	-	I	Cra
R CrA	285.473568	-36.952187	B5 ⁴	HAeBe	Cra
R CrA-IRS 7B	285.485	-36.957861	-	I	Cra
CrA 01	285.7444	-37.1266	-	I	Cra
HD 179218	287.796875	15.787667	A0 ¹²	HAeBe	-
LDN 723-mm	289.47375	19.2055	-	0	-
HD 181296	290.713375	-54.423931	A0 ⁴⁶	DD	BPMG
HD 181327	290.745583	-54.538056	F6 ⁴⁶	DD	BPMG
Parsamian 21	292.254	9.645000	-	I	-
[SER2000] B335	294.2529	7.5689	-	0	-
HD 191089	302.271727	-26.224036	F5 ²⁵	DD	-
HD 192758	304.565792	-42.860082	F0 ²²	DD	Argus
AFGL 2591	307.353139	40.189365	-	-	-
DR 21 (OH)	309.753208	42.380500	-	-	-
LDN 1157-mm	309.7758	68.0375	-	0	-
AU Mic	311.289708	-31.340889	M1 ¹	DD	BPMG
HH 381IRS	314.589208	52.490806	-	I	-
HD 203024	319.012583	68.914472	A5 ⁸	DD	-
L 1014	321.0312	49.98583	-	0	-
HH 354IRS	331.710417	59.046389	-	I	-
V733 Cep	343.388583	62.539889	-	I	Cep OB

Table B.1. continued.

Source name	RA (deg)	Dec (deg)	Sp. type	Disc type	Association
–	–	–	–	–	–
Fomalhaut	344.412708	-29.622222	A4 ⁴	DD	-
HR 8799	346.869625	21.13425	F0 ⁴	DD	Col
NGC 7538 IRS1	348.4387	61.46944	-	-	-
HD 221853	353.90064	8.382618	F0 ⁴⁸	DD	LA

Spectral types are taken from: (1) Torres et al. (2006), (2) Houk & Cowley (1975), (3) Houk & Smith-Moore (1988), (4) Gray et al. (2006), (5) Harlan (1974), (6) Luhman et al. (2010), (7) Mohanty et al. (2013), (8) Mora et al. (2001), (9) Manoj et al. (2006), (10) Meeus et al. (2013), (11) Houk & Swift (1999), (12) Vieira et al. (2003), (13) Zuckerman & Song (2004b), (14) Webb et al. (1999), (15) Rydgren (1980), (16) Furlan et al. (2009), (17) Vacca & Sandell (2011), (18) Luhman (2007), (19) Luhman (2004), (20) de la Reza et al. (1989), (21) Gregorio-Hetem et al. (1992), (22) Houk (1978), (23) Levenhagen & Leister (2006), (24) Weinberger et al. (2004), (25) Houk (1982), (26) Spezzi et al. (2008), (27) Fedele et al. (2013), (28) Bouy & Martín (2009), (29) Alcalá et al. (2014), (30) López Martí et al. (2011), (31) Carpenter et al. (2006), (32) Köhler et al. (2000), (33) Kraus et al. (2008), (34) Dent et al. (2013), (35) Hughes et al. (1994), (36) Mortier et al. (2011), (37) Prato et al. (2003), (38) Preibisch et al. (1998), (39) Preibisch et al. (2002), (40) Wichmann et al. (1997), (41) McClure et al. (2010), (42) Bouvier & Appenzeller (1992), (43) Ricci et al. (2010), (44) Erickson et al. (2011), (45) Martin et al. (1998), (46) Nilsson et al. (2009), (47) Hales et al. (2014), (48) Zuckerman & Song (2004a)

Table B.2. Fluxes at 63 μm for YSOs in the sample

Source name	RA (deg)	Dec (deg)	obs ID	$F_{[OI]}$ (10^{-18}W/m^2)	$F_{\text{H}_2\text{O}}$ (10^{-18}W/m^2)	$F_{63\mu\text{m}}$ (Jy)
HD 105	1.468958	-41.753	1342199239	< 6	< 6	< 0.5
HD 377	2.107292	6.616806	1342212530	< 7	< 7	< 0.5
HD 3003	8.182958	-63.0315	1342199240	< 7	< 7	< 1.0
HD 3670	9.736267	-52.5342	1342269870	< 7	< 7	< 0.5
HD 9672	23.65741	5.6763	1342188424	< 11	< 11	1.9 ± 0.4
tau Ceti	26.017	5.9374	1342189611	< 8	< 8	< 0.624
W3 IRS5	36.41916	62.0975	1342229091	22026 ± 520	< 632	6958 ± 20
W3 IRS5	36.41916	62.0975	1342229093	25543 ± 3329	< 1000	8461 ± 61
HD 15115	36.567667	6.292556	1342225584	< 7.6	< 7.6	< 0.50
HD 16743	39.78151	-52.9348	1342264255	< 10	< 10	< 0.57
SMM J032537+30451	51.343	30.75386	1342263508	1668 ± 8	37 ± 6	17.1 ± 1.1
LDN 1448N	51.40204	30.75616	1342263506	1609 ± 10	38 ± 5	22 ± 1
L1448-C(S)	51.413	30.73283	1342263510*,**	545 ± 13	168 ± 7	24.4 ± 1.2
LDN 1455	52.0027	30.133	1342204122	66 ± 14	< 16	1.8 ± 0.4
IRAS 03235+3004	51.65612	30.2578	1342264250	238 ± 11	< 13	5.9 ± 0.8
LDN 1455 IRS3	51.913644	30.217410	1342214677	117 ± 16	< 21	39.0 ± 0.5
2MASS J03283706+3113310	52.15454	31.22522	1342264248	188 ± 9	< 15	66 ± 1
SSTc2d J032857.4+311416	52.239	31.23775	1342264247	< 30	< 39	60.5 ± 1.7
SSTc2d J032900.5+311200	52.25229	31.20022	1342264245	114 ± 9	< 17	< 2.7
2MASS J03290149+3120208	52.2565	31.33905	1342264243	1791 ± 11	70 ± 7	20.8 ± 0.7
2MASS J03290773+3121575	52.28241	31.36591	1342267612	1465 ± 8	136 ± 6	59.9 ± 0.9
NGC 1333 IRAS 4A	52.29375	31.22525	1342216083	119 ± 4	32 ± 5	15.1 ± 0.5
	52.29375	31.22525	1342216084	141 ± 20	< 12	15.1 ± 0.8
SSTc2d J032910.7+311821	52.2945	31.30572	1342267616	< 28	< 15	15.9 ± 0.8
NGC 1333 IRAS 4B	52.300042	31.21894	1342216178	111 ± 23	< 29	5.7 ± 0.7
SSTc2d J032912.0+311301	52.30025	31.21713	1342267608*,**	260 ± 7	258 ± 4	< 2.4
SSTc2d J032913.5+311358	52.30641	31.23283	1342267610	54 ± 11	< 14	< 3
HBC 347	52.40987	24.51055	1342192136	< 14	< 14	< 1.2
IRAS 03267+3128	52.46591	31.65166	1342267614	< 20	< 12	< 3.7
IRAS 03271+3013	52.56308	30.39705	1342263513	277 ± 14	48 ± 5	8.6 ± 1.1
IRAS 03282+3035	52.83741	30.75836	1342263515	146 ± 13	< 16	5.1 ± 0.8
HD 21997	52.97354	-25.6141	1342247735	< 11	< 11	< 0.9
IRAS 03292+3039	53.07483	30.82986	1342265448	163 ± 9	< 15	< 2.8
epsilon Eri	53.23266	-9.45825	1342191348	< 9	< 9	< 0.6
IRAS03301+3111	53.30333	31.35672	1342215668	387 ± 18	39 ± 13	5.1 ± 0.6
B1-c	53.32437	31.15886	1342216213	< 21	< 21	13.0 ± 0.5
SSTc2d J033314.3+310710	53.30991	31.11969	1342263487	93 ± 8	< 17	< 2.6
SSTc2d J033316.4+310653	53.3185	31.11458	1342265450	397 ± 13	< 17	< 2.5
B1-a	53.31958	31.132	1342216182	358 ± 15	59 ± 19	8.4 ± 0.5
SSTc2d J033327.3+310710	53.3637	31.1195	1342265452	1065 ± 5	< 15	< 3.6
IRAS 03407+3152	55.9855	32.01466	1342265454	231 ± 9	< 14	2.3 ± 0.68
SSTc2d J034356.8+320305	55.98683	32.0513	1342265456	172 ± 8	< 16	4.7 ± 1.2
2MASS J03444389+3201373	56.18316	32.02672	1342265702	601 ± 7	< 10	8.4 ± 0.7
LkHa 330	56.45116	32.4033	1342239377	< 10	< 10	12.3 ± 0.2
	56.45117	32.40331	1342238941	< 57	< 57	12.6 ± 1.2
HBC 356	60.80829	25.8833	1342214359	< 11	< 11	< 1.0
HBC 358	60.96183	26.18144	1342204347	< 11	< 11	< 1.0
	60.96183	26.18144	1342214680	< 13	< 13	< 1.4
IRAS 04016+2610	61.179055	26.315706	1342216216	430 ± 22	< 28	42.2 ± 0.5
	61.17916	26.31583	1342204348	396 ± 6	31 ± 5	43.1 ± 0.5
PP 13S	62.671458	38.132028	1342263505	1108 ± 41	< 64	54 ± 1
LkCa 1	63.30891	28.31967	1342214679	< 10	< 10	< 1.4
V1096 Tau	63.36345	28.27355	1342214678	< 13	< 13	< 1.2
V773 Tau	63.55383	28.20345	1342216217	80 ± 4	< 7	0.8 ± 0.2
FM Tau	63.55658	28.21366	1342216218	< 12	< 12	< 1.20
CW Tau	63.57083	28.18272	1342216221	84 ± 6	< 12	1.5 ± 0.4
CIDA1	63.57337	28.10269	1342268646	< 4	< 4	< 0.4
CX Tau	63.69941	26.80305	1342225729	< 9	< 9	< 1.1
LkCa 3	63.69987	27.87629	1342216220	< 10	< 10	< 1.2
FO Tau	63.70537	28.2085	1342216645	< 14	< 14	< 1.8
CIDA-2	63.7715	28.14616	1342216643	< 11	< 11	< 1.2
LkCa 4	64.11712	28.12661	1342216642	< 11	< 11	< 1.2
CY Tau	64.39054	28.34636	1342192794	< 11	< 11	< 1.0
LkCa 5	64.41225	28.55014	1342216641	< 11	< 11	< 1.3
IRAS 04158+2805	64.74225	28.20652	1342192793	55 ± 4	< 11	< 1.3
FQ Tau	64.80337	28.49252	1342192795	< 10	< 10	< 1.2
BP Tau	64.81595	29.10747	1342192796*	8 ± 2	< 9	< 1.0
	64.81595	29.10747	1342225728	9 ± 3	11 ± 3	< 0.8
V819 Tau	64.85941	28.4373	1342216651	< 12	< 12	< 1.2
FR Tau	64.8977	28.45605	1342263516	< 3	< 3	< 0.2
LkCa 7	64.92195	27.83013	1342216649	< 12	< 12	< 1.3
IRAS 04169+2702	64.99333	27.16583	1342265457	608 ± 7	< 23	16.9 ± 0.7
IRAS 04181+2654	65.2975	27.01916	1342265459	206 ± 6	24 ± 3	2.7 ± 0.8

Table B.2. continued.

Source name	RA (deg)	Dec (deg)	obs ID	$F_{[OI]}$ (10^{-18}W/m^2)	$F_{\text{H}_2\text{O}}$ (10^{-18}W/m^2)	$F_{63\mu\text{m}}$ (Jy)
DE Tau	65.48183	27.91836	1342192797	< 13	< 13	1.4 ± 0.5
IRAM04191	65.48708	15.49608	1342216654	160 ± 23	< 24	< 1.7
RY Tau	65.48916	28.4432	1342190361	100 ± 6	22 ± 7	10.3 ± 0.6
HD 283572	65.4952	28.30184	1342216646	< 11	< 11	< 0.9
T Tau	65.49762	19.5351	1342190353	8339 ± 15	288 ± 14	98.1 ± 1.1
2MASS J04220069+2657324	65.5025	26.95888	1342265461	91 ± 8	22 ± 5	3.7 ± 0.9
FS Tau	65.50908	26.95847	1342192791	378 ± 4	20 ± 4	2.4 ± 0.5
FS Tau B	65.509071	26.958469	1342192791	43 ± 6	< 16	2.1 ± 0.5
FU Tau	65.8975	25.05075	1342264241	< 3	< 3	< 21
FT Tau	65.91329	24.93725	1342192790	20 ± 6	< 12	< 1.2
IP Tau	66.23783	27.19902	1342225756	< 8	< 8	< 0.7
J1-4872	66.32366	26.29733	1342216653	< 12	< 12	< 1.2
FV Tau	66.72304	26.11511	1342239720	< 72	< 72	2.35 ± 1.6
DG Tau B	66.76066	26.09186	1342192798*	130 ± 5	< 10	5.7 ± 0.5
	66.76083	26.09166	1342265463	515 ± 11	24 ± 6	16.0 ± 1.0
DF Tau	66.76283	25.70647	1342190359	52 ± 7	< 13	0 ± 0
DG Tau	66.76958	26.10452	1342190382*,**	606 ± 7	< 16	5.6 ± 0.4
	66.76958	26.10452	1342225730	1534 ± 15	< 16	25.5 ± 0.4
IRAS 04248+2612	66.98875	26.32166	1342265466	173 ± 10	< 17	5.2 ± 1.1
IRAS 04264+2433	67.375	24.66527	1342265468	569 ± 9	35 ± 9	5.4 ± 1.0
FW Tau	67.37379	26.28144	1342225735	< 10	< 10	< 1.4
DH Tau	67.42508	26.54811	1342225734	< 14	< 14	< 1.5
IQ Tau	67.46483	26.11247	1342239721	< 38	< 38	< 2.4
	67.46483	26.11247	1342192135*	< 12	< 12	< 1.2
	67.46483	26.11247	1342225733	16 ± 3	11 ± 3	0.7 ± 0.3
CFHT20	67.49795	24.55216	1342265469	< 4	< 4	< 2.5
UX Tau	67.51662	18.23038	1342204350	38 ± 4	< 10	3.3 ± 0.4
	67.51662	18.23038	1342214357	35 ± 3	< 10	3.6 ± 0.3
	67.51666	18.23038	1342239724	< 63	< 63	4.1 ± 1.4
FX Tau	67.62337	24.44583	1342192800	< 13	< 13	< 1.2
DK Tau	67.68433	26.02355	1342192132*	< 12	< 12	< 1.4
	67.68433	26.02355	1342225732	21 ± 4	< 6	0.9 ± 0.2
ZZ Tau	67.71408	24.70619	1342192799	< 13	< 13	< 1.0
ZZ TauIRS	67.71545	24.69652	1342240153	< 61	< 61	2.4 ± 1.3
V927 Tau	67.84925	24.18136	1342225763	< 9	< 9	< 0.8
IRAS 04287+1801	67.892047	18.134481	1342192805	4619 ± 77	< 89	358 ± 3
HL Tau	67.9101	18.232681	1342190351**	510 ± 54	62 ± 10	65.5 ± 3.2
XZ Tau	67.9145	18.23213	1342190351**	242 ± 6	15 ± 4	3.1 ± 0.3
HK Tau	67.9607	24.40501	1342225736	37 ± 3	< 9	2.3 ± 0.3
V710 Tau	67.99083	18.35975	1342192804	< 11	< 11	< 1.0
Haro 6-13	68.0642	24.48325	1342239763	< 78	< 78	8.4 ± 1.8
	68.0642	24.48325	1342192128	64 ± 5	< 11	4.6 ± 0.4
GG Tau	68.12645	17.52794	1342192121	53 ± 5	< 13	3.2 ± 0.5
UZ Tau	68.17845	25.87538	1342240155	< 74	< 74	< 4.7
	68.1787	25.87572	1342192131*,**	13 ± 4	< 13	< 1.4
GH Tau	68.27679	24.16236	1342192801*,**	< 9	< 9	< 1.0
V807 Tau	68.27762	24.16528	1342192801	31 ± 6	< 10	< 0.7
GI Tau	68.39295	24.35319	1342225760*,**	< 7	< 7	< 0.6
GK Tau	68.394	24.35161	1342239764*	< 50	< 50	< 3.3
DL Tau	68.41275	25.34394	1342190355*,**	< 11	< 11	< 1.5
	68.41275	25.34394	1342240154	< 56	< 56	< 3.9
	68.41275	25.34394	1342225800	27 ± 3	< 6	1.1 ± 0.2
HN Tau	68.41395	17.86454	1342225796	50 ± 3	< 7	0.9 ± 0.2
DM Tau	68.453	18.16944	1342192123*	< 10	< 10	< 1.2
	68.453	18.16944	1342239748	< 44	< 44	< 2.6
	68.453	18.16944	1342225825	11 ± 3	< 6	0.8 ± 0.2
CI Tau	68.46666	22.84172	1342225799	< 66	< 66	< 4.6
	68.46666	22.84172	1342192125	27 ± 4	< 10	1.5 ± 0.4
AA Tau	68.73091	24.48144	1342190357*	< 11	5 ± 2	< 1.2
	68.73091	24.48144	1342240152	< 51	< 51	< 3.1
	68.73091	24.48144	1342225758	25 ± 2	9 ± 2	1.0 ± 0.2
HO Tau	68.83416	22.53738	1342192803	< 13	< 13	< 1.4
FF Tau	68.83708	22.90672	1342192802	< 10	< 10	< 1.6
DN Tau	68.86404	24.24969	1342192127*	< 9	< 9	< 1.7
	68.86404	24.24969	1342240151	< 38	< 38	< 2.5
	68.86404	24.24969	1342225757	4 ± 1	< 6	0.75 ± 0.25
IRAS 04325+2402	68.89708	24.13861	1342267857	479 ± 11	< 14	11.0 ± 0.8
HP Tau	68.96991	22.90641	1342240150	< 62	< 62	4.3 ± 1.3
J04381486	69.56191	26.19441	1342265470	< 3	< 3	< 0.2
GMTau	69.58891	26.1538	1342264239	< 3	< 3	< 0.2
DO Tau	69.61908	26.18038	1342240156*,**	< 68	< 68	6.6 ± 1.4
	69.61908	26.1804	1342190385	63 ± 8	< 13	< 1.54
HV Tau	69.647	26.17739	1342225801*	40 ± 4	< 7	< 0.8
TMR 1*	69.80791	25.88905	1342192985	401 ± 19	178 ± 40	9.1 ± 0.5

Table B.2. continued.

Source name	RA (deg)	Dec (deg)	obs ID	$F_{[OI]}$ (10^{-18}W/m^2)	$F_{\text{H}_2\text{O}}$ (10^{-18}W/m^2)	$F_{63\mu\text{m}}$ (Jy)
TMR 1B	69.80708	25.88916	1342225834*,**	360 ± 7	45 ± 6	20.4 ± 0.6
VY Tau	69.82254	22.79816	1342192989	< 10	< 10	< 1.3
LkCa 15	69.82416	22.35097	1342240149*	< 73	< 73	< 4.8
	69.82416	22.35096	1342190387*	< 11	< 11	< 1.3
	69.82416	22.35097	1342225798	12 ± 2	< 6	1.2 ± 0.2
2MASS J04393364+2359212	69.8902	23.98922	1342263934	< 3	< 3	0.12 ± 0.07
IRAS 04365+2535	69.89541	25.69583	1342225832**	446 ± 13	< 31	36.6 ± 0.7
	69.89583	25.69597	1342192987*	531 ± 41	< 50	32.7 ± 0.7
BD Tau4	69.94783	26.028	1342264240	< 3	< 3	< 0.2
L1527	69.97458	26.05272	1342192983	261 ± 6	< 18	7.0 ± 0.4
	69.973865	26.052661	1342192981	243 ± 19	< 22	6.8 ± 0.5
IRAS 04381+2540	70.30166	25.77666	1342225830*,**	111 ± 9	< 21	1.1 ± 0.5
	70.30166	25.77666	1342225803	923 ± 18	< 18	9.3 ± 0.7
CoKuTau 4	70.32004	28.66669	1342191360	20 ± 5	< 12	< 1.4
	70.32004	28.66669	1342225837	23 ± 1	< 4	1.0 ± 0.2
IRAS 04385+2550	70.41175	25.94077	1342240157	< 71	< 71	< 4.6
	70.41175	25.94076	1342225828	66 ± 3	< 8	2.6 ± 0.3
DP Tau	70.65708	25.26041	1342191362*,**	< 11	< 11	< 1.1
GO Tau	70.76287	25.33855	1342191361	< 11	< 11	< 1.2
	70.76287	25.33855	1342225826	< 7	< 7	< 0.9
DQ Tau	71.72104	17.00005	1342225806	25 ± 5	< 13	1.4 ± 0.5
Haro 6-37	71.74575	17.04394	1342225805	< 15	< 15	< 1.6
DS Tau	71.95045	29.42068	1342225851*,**	< 6	< 6	< 0.7
UY Aur	72.94741	30.78708	1342193206*,**	< 11	< 11	< 1.1
	72.94741	30.78708	1342215699	338 ± 6	13 ± 3	5.6 ± 0.4
GM Aur	73.79575	30.36652	1342243657	< 80	< 80	< 5.7
	73.79579	30.36645	1342191357*	23 ± 4	< 12	1.7 ± 0.5
AB Aur	73.94095	30.55121	1342191355	667 ± 20	< 55	94.3 ± 0.6
	73.941	30.55119	1342217842*	359 ± 27	< 34	50.3 ± 0.8
SU Aur	73.99741	30.5671	1342217844	86 ± 3	< 8	6.0 ± 0.4
HD 31648	74.69277	29.84361	1342226002	101 ± 3	10 ± 2	12.4 ± 0.2
HD 32297	75.61431	7.461022	1342217849	< 9	< 9	1.2 ± 0.3
V836 Tau	75.7775	25.3888	1342227634	< 7	< 7	< 1.1
RW Aur	76.95641	30.4014	1342191359	158 ± 9	< 14	1.9 ± 0.4
HD 35187	81.00487	24.96044	1342217846	< 26	< 26	4.4 ± 0.6
	81.00488	24.96043	1342226900	27 ± 3	< 8	4.5 ± 0.3
HD 35841	81.65244	-22.4899	1342270644	< 12	< 12	< 0.8
HD 36112	82.6147	25.33252	1342227635	39 ± 3	< 9	18.5 ± 0.4
	82.6147	25.33252	1342228247	< 19	< 19	16.9 ± 0.4
HD 36910	83.99361	24.74835	1342227638	49 ± 3	< 7	19.8 ± 0.2
V833 Ori	84.57541	-7.04061	1342265949	< 120	< 120	155 ± 2.8
HD 245906	84.877	26.33197	1342228528	88 ± 24	< 29	< 1.0
[SMZ2000] L1643-S3 MMS 1	84.98291	-7.50777	1342226195	1554 ± 8	82 ± 17	364 ± 1
Re50 NN IRS	85.114167	-7.458667	1342265946	1054 ± 32	< 65	104 ± 2
V1647 Ori	86.55475	-0.101333	1342267864	139 ± 32	< 570	29 ± 1
HD 38120	85.79954	-4.99719	1342226212	66 ± 16	< 20	9.2 ± 0.5
HD 38207	85.83733	-20.1892	1342270645	< 7	< 7	< 0.5
HD 38206	85.84029	8.5574	1342270646	< 11	< 11	< 0.8
HR 1998	86.73892	4.8219	1342226192	< 7	< 7	< 0.9
NGC 2071 IR	86.76833	0.363611	1342218761*	7996 ± 39	517 ± 23	402 ± 2
β Pic	86.8212	-51.0665	1342188425	11 ± 3	< 10	9.9 ± 0.2
R Mon	99.79145	8.736028	1342250903	2370 ± 82	< 97	96.6 ± 1.9
HD 50138	102.8891	-6.9665	1342206991	2103 ± 16	< 23	8.5 ± 0.7
PDS 27	109.8997	7.655	1342251034	< 74	< 74	55 ± 1.0
HD 61005	113.94775	-32.203889	1342230911	< 8.2	< 8.2	0.4 ± 0.1
Bran 76	117.648333	-33.106639	1342254930	< 61	< 61	< 4.2
RECX 1	129.2342	-78.9459	1342210391	< 11	< 11	< 1.5
RECX 14	130.3762	-78.8851	1342210390	< 6	< 6	< 0.8
RECX 3	130.4042	-79.0584	1342210389	< 11	< 11	< 1.1
RECX 4	130.5988	-79.0675	1342199241	< 5	< 5	< 0.7
RECX 5	130.6129	-78.9633	1342210392	< 9	< 9	< 1.0
RECX 6	130.6616	-78.9118	1342223114	< 9	< 9	< 1.1
RECX 8	130.8009	-79.07	1342223113	< 10	< 10	< 1.1
RECX 15	130.8274	-79.0883	1342186314	30 ± 6	< 10	< 0.6
RECX 15	130.8274	-79.0883	1342210388	24 ± 2	< 6	< 1.2
J0844.2-7833	131.0381	-78.5626	1342210387	< 7	< 7	< 1.0
RECX 9	131.0682	-78.9855	1342223112	< 8	< 8	< 0.6
RECX 10	131.1328	-78.7753	1342223111	< 13	< 13	< 1.3
[MGL99] IRS 17 57	131.6445	-43.9084	1342211844	8156 ± 12	84 ± 18	206 ± 1
RECX 11	131.7569	-78.9929	1342223115	< 7	< 7	< 0.7
RECX 12	131.9865	-78.9147	1342223110	< 11	< 11	< 1.2
TWA 07	160.6254	-33.6711	1342199411	< 7	< 7	< 0.8
Sz Cha	164.5698	-77.288	1342225560	< 76	< 76	< 5.0
	164.5698	-77.288	1342233478	15 ± 2	< 6	3.8 ± 0.1

Table B.2. continued.

Source name	RA (deg)	Dec (deg)	obs ID	$F_{[OI]}$ (10^{-18}W/m^2)	$F_{\text{H}_2\text{O}}$ (10^{-18}W/m^2)	$F_{63\mu\text{m}}$ (Jy)
CR Cha	164.7791	-77.0278	1342232614	16 ± 3	< 6	1.6 ± 0.1
TWA 01	165.4662	-34.7047	1342248544	32 ± 5	< 15	3.4 ± 0.3
	165.4663	-34.7047	1342187127	35 ± 4	< 10	2.9 ± 0.3
CS Cha	165.6037	-77.5599	1342233479	< 65	< 65	< 4.2
	165.6037	-77.5599	1342233480	16 ± 2	< 5	3.5 ± 0.1
CHX 7	166.5642	-77.3657	1342232584	< 61	< 61	< 4.0
	166.5642	-77.3658	1342233477**	15 ± 2	< 7	0.31 ± 0.09
Eso H alpha 559	166.6064	-76.5616	1342263489	< 4	< 4	< 0.3
2MASS J11064658-7722325	166.694084	-77.37571	1342210187	0 ± 0	0 ± 0	0 ± 0
[NC98] Cha HA 1	166.8195	-77.598139	1342263459	< 3	< 3	< 0.3
Sz 18	166.8297	-76.0513	1342232290	< 32	< 32	< 2.1
	166.8297	-76.0513	1342232585	< 6	< 6	0.55 ± 0.1
HD 97048	167.0138	-77.6548	1342199412*	853 ± 18	< 26	42.9 ± 0.7
	167.0139	-77.6548	1342188436	1481 ± 4	< 11	64.1 ± 0.4
HP Cha	167.0629	-77.5647	1342233473	< 61	< 61	8.9 ± 1.3
Sz27	167.1627	-77.2678	1342233476	10 ± 1	< 4	0.4 ± 0.1
TWA 02AB	167.3075	-30.0277	1342199410	< 7	< 7	< 0.9
GM Cha	167.3687	-76.5578	1342267619	221 ± 13	< 17	11 ± 1
T 42	167.4725	-76.5737	1342232291	493 ± 59	< 74	21 ± 2
WW Cha	167.5004	-76.5827	1342232292	422 ± 55	< 70	35 ± 2
TWA 03A	167.6161	-37.5311	1342209871	< 6	< 6	0.8 ± 0.2
Hn13	167.7332	-76.759	1342263492	4 ± 1	< 3	< 0.20
CV Cha	168.1155	-76.7395	1342232293	< 78	< 78	< 5.4
CHX22	168.1778	-77.373	1342233474	24 ± 1	< 4	0.33 ± 0.09
Sz 45	169.4042	-77.0772	1342231724	< 31	< 31	< 2.1
	169.4042	-77.0772	1342233475	< 5	< 5	0.9 ± 0.1
TWA 13AB	170.3218	-34.7793	1342210382	< 7	< 7	< 0.6
HD 98800B	170.522	-24.7777	1342223821	< 7	< 7	7.6 ± 0.3
	170.522	-24.7775	1342199409	8 ± 2	< 5	6.2 ± 0.2
HD 98922	170.6319	-53.3698	1342210385	197 ± 16	< 20	4.1 ± 0.5
HD 100453	173.2732	-54.3245	1342203059	58 ± 5	< 13	37.9 ± 0.9
	173.2732	-54.3245	1342212228	34 ± 3	< 9	28.6 ± 0.3
	173.2732	-54.3245	1342211695	99 ± 32	< 21	32.8 ± 0.50
HD 100546	173.356	-70.1947	1342188038	5462 ± 72	< 88	180.2 ± 0.7
	173.356	-70.1947	1342188438	5645 ± 8	< 22	180 ± 2
T Cha	179.3063	-79.3587	1342232294	48 ± 4	< 12	6.7 ± 0.2
HD 104237	180.0211	-78.1929	1342207819	85 ± 17	< 23	10.6 ± 0.5
	180.0211	-78.1929	1342212234	80 ± 4	< 11	10.5 ± 0.3
IRAS 11590-6452	180.400965	-65.147898	1342212230	1354 ± 41	< 46	53 ± 1
	180.4012	-65.148	1342212232*	1340 ± 34	80 ± 21	52 ± 1
TWA 23	181.864	-32.7834	1342213143	< 9	< 9	< 1.0
MML 17	185.638458	-53.5636	1342226186	< 8.4	< 8.4	< 0.5
TWA 10	188.7677	-41.6107	1342203443	< 7	< 7	< 0.9
HR 4796A	189.0042	-39.8695	1342199242	< 7	< 7	6.7 ± 0.2
DK Cha	193.3217	-77.1196	1342226006	2716 ± 78	< 94	125 ± 2
	193.3216	-77.1196	1342188039*	1330 ± 119	< 98	37 ± 3
ChaII-J125342.86-771511.5	193.4285	-77.2531	1342226005	73 ± 3	< 8	2.5 ± 0.3
ChaII-J125633.66-764545.3	194.1402	-76.7625	1342226009	< 8	< 8	< 1.0
ChaII-J125711.77-764011.3	194.299	-76.6698	1342226010	< 9	< 9	< 1.0
ChaII-J125806.78-770909.4	194.5282	-77.1526	1342226007	< 7	< 7	< 0.8
2MASS J12590656-7707401	194.7774	-77.1277	1342265694	139 ± 9	10 ± 3	9.8 ± 0.7
ChaII-J130055.36-771022.1	195.2306	-77.1728	1342226008	< 6	< 6	0.7 ± 0.2
ChaII-J130158.94-775121.7	195.4955	-77.856	1342229799	< 7	< 7	< 0.8
ChaII-J130222.85-773449.3	195.5952	-77.5803	1342227072	< 6	< 6	< 0.7
ChaII-J130424.92-775230.1	196.1038	-77.875	1342229800	10 ± 3	< 8	< 0.7
Hn24	196.2322	-77.6637	1342235656*	9 ± 2	< 5	< 0.4
ChaII-J130508.53-773342.4	196.2855	-77.5617	1342227071	< 8	< 8	< 0.8
ChaII-J130512.69-773052.3	196.3028	-77.5145	1342229829	< 7	< 7	< 1.0
ChaII-J130520.68-773901.4	196.3361	-77.6503	1342229831	15 ± 5	< 8	< 1.3
ChaII-J130521.66-773810.0	196.3402	-77.6361	1342229830	6 ± 2	< 7	< 0.8
ChaII-J130529.04-774140.1	196.371	-77.6944	1342229832	< 8	< 8	< 0.7
ChaII-J130718.05-774052.9	196.8252	-77.6813	1342229833	< 8	< 8	< 0.7
ChaII-J130748.51-774121.4	196.9521	-77.6892	1342228418	< 7	< 7	< 0.8
ChaII-J130806.28-775505.2	197.0261	-77.9181	1342229801	15 ± 4	6 ± 2	< 0.8
ChaII-J130827.17-774323.2	197.1132	-77.7231	1342228419	< 8	< 8	< 0.9
HD 114082	197.3174	-60.3083	1342265693	< 8	< 8	0.5 ± 0.2
ChaII-J130950.38-775723.9	197.4599	-77.9566	1342228420	< 6	< 6	< 0.7
HD 131835	224.2269	-35.6954	1342248686	< 12	< 12	< 1.2
SAO 206462	228.9518	-37.1544	1342190370	43 ± 5	< 13	33.0 ± 0.6
	228.9518	-37.1544	1342213921	< 26	< 26	28.3 ± 0.4
HIP 76310	233.8171	-25.7341	1342191303	< 13	< 13	< 1.2
HD 139614	235.1932	-42.4981	1342191300	41 ± 7	< 17	19.8 ± 0.5
	235.1932	-42.4981	1342215683	18 ± 6	< 20	20.0 ± 0.4
HT Lup	236.3036	-34.2918	1342213920	< 19	< 19	2.2 ± 0.5

Table B.2. continued.

Source name	RA (deg)	Dec (deg)	obs ID	$F_{[OI]}$ (10^{-18}W/m^2)	$F_{\text{H}_2\text{O}}$ (10^{-18}W/m^2)	$F_{63\mu\text{m}}$ (Jy)
HD 141569	237.4906	-3.92121	1342190376	191 ± 4	< 11	3.4 ± 0.4
	237.4906	-3.92122	1342213913	203 ± 19	< 20	4.1 ± 0.5
G327-0.6***	238.286005	-54.616659	1342216202	-3105 ± 136	< 335	882 ± 8
HIP 77911	238.6733	-22.7662	1342214223	< 7	< 7	< 0.6
HD 142666	239.1667	-22.0277	1342213916*	< 16	< 16	0 ± 0
	239.1667	-22.0277	1342214224**	13 ± 2	< 8	0.9 ± 0.3
HD 142527	239.1745	-42.3231	1342216173	49 ± 3	< 8	108.4 ± 0.3
	239.1745	-42.3231	1342216174	< 36	< 36	97.6 ± 0.8
RU Lup	239.1762	-37.8209	1342215682	185 ± 20	< 19	5.7 ± 0.5
USco J155729.9-225843	239.3744	-22.9788	1342214222	< 6	< 6	< 0.7
Sz84	239.5105	-37.6007	1342229826	< 5	< 5	0.4 ± 0.1
USco J155829.8-231007	239.6242	-23.1687	1342203460	< 10	< 10	< 1.5
RY Lup	239.8682	-40.3642	1342216171	< 20	< 20	6.18 ± 0.5
1RXSJ160044.7-234330	240.1862	-23.725	1342213760	< 10	< 10	< 1.1
EX Lup	240.772875	-40.30706	1342266967	< 53	< 53	< 4.5
USco J160357.6-203105	240.9902	-20.5182	1342214227	< 9	< 9	< 0.7
USco J160357.9-194210	240.9914	9.703	1342214226	< 7	< 7	< 0.7
USco J160421.7-213028	241.0902	-21.5078	1342215681	25 ± 2	< 7	1.7 ± 0.2
J160532.1-193315	241.384	-19.5544	1342215637	< 11	< 11	< 1.0
USco J160545.4-202308	241.4394	-20.3855	1342216197	< 7	< 7	< 0.6
USco J160600.6-195711	241.5026	9.953	1342215736	< 7	< 7	< 1.0
ScoPMs 31	241.5915	9.479	1342216196	< 9	< 9	< 0.8
HD 144432	241.7415	-27.7193	1342213919	< 18	< 18	5.59 ± 0.5
Sz 91	241.7983	-39.063	1342229827	8 ± 2	< 5	0.7 ± 0.1
USco J160823.2-193001	242.0966	9.5002	1342216193	< 8	< 8	< 1.1
USco J160823.2-193001	242.0966	9.5002	1342216194	< 9	< 9	< 1.1
HD 144668	242.1428	-39.105	1342192146	128 ± 6	< 15	6.2 ± 0.5
	242.1428	-39.105	1342215641	132 ± 14	< 19	6.1 ± 0.4
Sz111	242.2278	-39.6286	1342229828	10 ± 1	< 4	1.39 ± 0.09
USco J160959.4-180009	242.4972	8.0025	1342216188	< 7	< 7	< 0.9
SSTLup	242.6233	-39.3708	1342241709	< 5	< 5	< 0.4
AS205	242.8806	8.6405	1342215737	222 ± 21	< 24	19.8 ± 0.6
HIP 79439	243.1837	9.5028	1342216190	< 7	< 7	< 0.6
USco J161411.0-230536	243.5461	-23.0933	1342216169	< 8	< 8	< 0.7
USco J161420.2-190648	243.5845	9.1133	1342216191	43 ± 4	< 8	1.1 ± 0.3
RXJ1615.3-3255	243.8342	-32.918	1342229825	17 ± 2	< 5	1.3 ± 0.1
HIP 79878	244.5673	-28.0416	1342216170	< 6	< 6	< 0.7
HIP 80088	245.2092	-22.594	1342216168	< 7	< 7	< 0.7
2MASS J16230923-2417047	245.7884	-24.2846	1342250127	19 ± 2	< 4	2.6 ± 0.1
Doar 21	246.5125	-24.3933	1342240163	385 ± 56	< 60	8.6 ± 1.3
GSS30-IRS1	246.5891	-24.3845	1342215678	1836 ± 51	334 ± 53	148 ± 1
GSS 31	246.5974	-24.3499	1342240164	< 94	< 94	5.2 ± 2.1
DoAr 25	246.5986	-24.7205	1342241708	< 68	< 68	< 4.6
VLA1623-243	246.61	-24.4083	1342213918	399 ± 19	< 20	13.1 ± 0.5
WL12	246.6841	-24.5801	1342228187	494 ± 18	50 ± 15	13.6 ± 0.5
DoAr 28	246.6975	-23.2478	1342241707	10 ± 1	< 5	0.9 ± 0.1
	246.6978	-23.2485	1342229823	< 30	< 30	< 2.0
WL 2	246.702	-24.4774	1342242631	< 60	< 60	< 4.1
Oph 01	246.7462	-24.5842	1342266925	3109 ± 19	< 12	28.2 ± 0.6
Elias 29	246.7891	-24.6218	1342228519	1840 ± 69	511 ± 71	141 ± 1
SR 21	246.7928	-24.3201	1342229824	13 ± 4	< 13	36.8 ± 0.3
	246.7928	-24.3201	1342227209	< 21	< 21	33.9 ± 0.5
IRS 44	246.8725	-24.6544	1342228474	436 ± 37	< 37	17.9 ± 0.9
IRS 46	246.8725	-24.6544	1342228474	76 ± 23	< 22	4.5 ± 0.4
IRS 48	246.9049	-24.5097	1342227069	322 ± 19	< 25	44.8 ± 0.5
GY 314	246.9142	-24.6543	1342242632	113 ± 35	< 61	3.1 ± 1.3
WSB 60	247.0687	-24.6161	1342242633	< 36	< 36	< 2.4
	247.0687	-24.6161	1342250128	< 6	< 6	0.8 ± 0.1
DoAr 44	247.8893	-24.4603	1342241269	< 68	< 68	5.2 ± 2.0
	247.8894	-24.4603	1342250578	25 ± 2	8 ± 1	4.86 ± 0.08
IRS 63	247.8983	-24.0248	1342228473	205 ± 18	< 20	16.8 ± 0.57
L1689S NO2	247.967	-24.9376	1342241270*	235 ± 70	< 73	4.3 ± 1.6
16289-2457	247.978	-25.0566	1342242634	< 78	< 78	< 5.1
2MASS J16320099-2456419	248.0041	-24.9451	1342263469	1092 ± 12	48 ± 7	87.4 ± 0.9
16293-2424	248.0877	-24.5099	1342241268	< 72	< 72	< 4.5
V346 Nor	248.134125	-44.925194	1342267622	382 ± 36	< 69	96.4 ± 1.6
RNO 90	248.5382	5.8046	1342228206	128 ± 20	< 18	3.5 ± 0.5
HBC 650	248.6221	-15.7837	1342215639	811 ± 6	< 17	27.2 ± 0.6
HD 150193	250.0746	-23.8958	1342227068	18 ± 5	< 19	7.6 ± 0.5
	250.0746	-23.8958	1342216625	23 ± 3	< 9	6.8 ± 0.2
Sco01	251.7427	-9.58883	1342267176	223 ± 9	< 17	8.5 ± 0.6
KK Oph	257.5335	-27.255	1342192148	168 ± 6	< 15	4.6 ± 0.4
NGC 6334-I***	260.222037	-35.78329	1342239385	5313 ± 151	< 742	6407 ± 17
HD 158352	262.2068	0.330625	1342190377	< 11	< 11	< 0.9

Table B.2. continued.

Source name	RA (deg)	Dec (deg)	obs ID	$F_{[OI]}$ (10^{-18}W/m^2)	$F_{\text{H}_2\text{O}}$ (10^{-18}W/m^2)	$F_{63\mu\text{m}}$ (Jy)
HD 158643	262.8539	-23.9626	1342217821	49 ± 3	< 7	1.1 ± 0.3
HD 163296	269.0887	-21.956	1342192161	206 ± 5	< 14	19.2 ± 0.6
	269.0887	-21.956	1342243512	197 ± 6	14 ± 4	18.2 ± 0.3
	269.0887	-21.956	1342217819	211 ± 18	< 21	18.1 ± 0.5
HD 164249	270.7642	-51.649	1342215648	< 8	< 8	< 1.0
W33A**,**	273.662980	-17.868719	1342239713	-3302 ± 145	< 429	1155 ± 15
[SER2000] L483	274.3745	-4.66097	1342192156	385 ± 6	58 ± 10	67.6 ± 0.6
HD 169142	276.124	-29.7803	1342186310	81 ± 5	< 13	20.2 ± 0.4
	276.124	-29.7803	1342206987*	< 23	< 23	11.5 ± 0.5
[MAM2011] Aqu-MM2	277.2659	-1.65041	1342254233	48 ± 15	9.9 ± 2.4	< 2.8
[MAM2011] Aqu-MM4	277.2858	-1.51188	1342254271*,**	48 ± 13	< 14	3.2 ± 0.8
[MAM2011] SerpS-MM1	277.407	-1.84938	1342254230	105 ± 6	< 14	14.8 ± 0.7
Serpens-SMM1a	277.4575	1.255694	1342207781	3329 ± 25	< 61	147 ± 1
EC82	277.487	1.24625	1342192975	< 23	< 23	8.4 ± 0.5
Serpens-SMM4	277.4882	1.220302	1342193217	148 ± 22	< 26	< 1.5
Serpens-SMM3	277.497	1.233806	1342193216	275 ± 29	< 21	3.3 ± 0.5
	277.4966	1.233416	1342207779	472 ± 12	< 31	31 ± 2
Serpens-SMM18	277.51736	-2.050743	1342254222	113 ± 8	< 18	13.9 ± 0.8
[MAM2011] Aqu-MM6	277.6045	-1.90372	1342254227**	< 21	< 14	< 2.4
[MAM2011] Aqu-MM7	277.6192	-1.94658	1342254224**	49 ± 14	< 12	< 4.2
[MAM2011] Aqu-MM8	277.6209	-1.93483	1342254228	< 25	< 15	< 2.9
[MAM2011] Aqu-MM14	277.708	-1.93502	1342254273	< 20	< 19	< 2.2
[MAM2011] W40-MM3	277.7892	-2.1068	1342254220	59 ± 7	< 14	10.3 ± 0.6
[MAM2011] W40-MM5	277.7931	-2.064	1342254268	802 ± 12	< 17	52 ± 2
[MAM2011] W40-MM26	277.9439	-2.07291	1342254266	1582 ± 10	< 19	7.2 ± 1.1
[MAM2011] W40-MM27	277.9449	-2.03886	1342254260	736 ± 10	< 22	10.8 ± 0.7
[MAM2011] W40-MM28	277.9495	-2.027	1342254264	656 ± 7	< 14	4.7 ± 0.8
[MAM2011] W40-MM34	277.9885	-2.00769	1342254259	< 25	< 12	< 2.1
[MAM2011] W40-MM36	278.0556	-1.95822	1342254263	76 ± 10	< 17	2.3 ± 0.8
Vega	279.2347	38.78369	1342188033	< 10	< 10	1.1 ± 0.2
HD 172555	281.362	-64.8712	1342215649	9 ± 3	< 6	< 0.8
	281.362	-64.8712	1342228417	10 ± 3	< 9	< 0.9
RXJ18523-3700	283.07208	-37.0033	1342216163	18 ± 2	< 6	1.8 ± 0.1
G34.26+0.15***	283.328128	1.249232	1342209733	-13757 ± 286	< 511	3049 ± 15
S Cra	285.2858	-36.9555	1342207809	429 ± 22	< 24	21.1 ± 0.6
RCrA-IRS 5A	285.4504	-36.9563	1342207806	1940 ± 18	170 ± 48	23 ± 2
RCrA-IRS 5N	285.451921	-36.954133	1342207806	880 ± 20	< 21	12 ± 1
RCrA-IRS 7A	285.480417	-36.954722	1342206990	4790 ± 70	< 68	122 ± 6
SMM 1C	285.48042	-36.95464	1342206990	8730 ± 60	0 ± 0	95 ± 6
R CrA	285.473568	-36.95218	1342206990	2340 ± 50	< 58	104 ± 2
R CrA-IRS 7B	285.485	-36.9578	1342207807	4768 ± 71	686 ± 210	80 ± 3
Cra 01	285.7444	-37.1266	1342254253	1416 ± 7	< 16	47 ± 0.9
HD 179218	287.7968	15.78766	1342208884	213 ± 17	< 22	27.0 ± 0.4
LDN 723-mm	289.47375	19.2055	1342208918	228 ± 7	< 24	7.7 ± 0.6
HD 181296	290.7133	-54.4239	1342209730	< 6	< 6	< 0.6
HD 181327	290.7455	-54.538	1342186311	< 8	< 8	1.8 ± 0.3
Parsamian 21	292.254	9.645	1342254615	< 53	< 53	12 ± 1
[SER2000] B335	294.2529	7.5689	1342208889	428 ± 25	< 20	10.8 ± 0.5
HD 191089	302.2717	-26.224	1342268180	< 14	< 14	< 0.9
HD 192758	304.5657	-42.86	1342216659	< 9	< 9	< 0.7
AFGL 2591***	307.353139	40.189365	1342208938	-3202 ± 89	< 480	3397 ± 12
DR 21 (OH)	309.753208	42.380500	1342209400	6269 ± 113	< 237	665 ± 7
LDN 1157-mm	309.7758	68.0375	1342208909	596 ± 21	< 25	12.2 ± 0.6
AU Mic	311.2897	-31.3408	1342193195	< 8	< 8	< 0.5
HH 381 IRS	314.589208	52.490806	1342258845*	210 ± 41	< 72	47 ± 2
HD 203024	319.0125	68.91447	1342206975	< 25	< 25	2.7 ± 0.5
L1014	321.0312	49.98583	1342208911	76 ± 16	< 22	< 1.5
HH 354 IRS	331.710417	59.046389	1342262014	602.0 ± 21	< 69	56 ± 1
V733 Cep	343.388583	62.539889	1342262017	< 72	< 72	< 4.8
Fomalhaut	344.4127	-29.6222	1342210402	< 8	< 8	1.5 ± 0.2
HR 8799	346.869625	21.13425	1342212242	< 7	< 7	< 0.4
NGC 7538 IRS1	348.4387	61.46944	1342211545*	45248 ± 147	< 440	3300 ± 11
HD 221853	353.9006	8.382618	1342212528	< 10	< 10	< 0.7

*: observation was mis-pointed.

**: source is located outside the central spaxel.

***: the source shows absorption in the central spaxel.

Table B.3. [OI] fluxes at 63 μ m from central spaxel, central 3x3 spaxels and IFU integrated

Source name	obs ID	$F_{[OI]}$ (10^{-18} W/m ²)	$F_{[OI]3\times 3}$ (10^{-18} W/m ²)	$F_{[OI]5\times 5}$ (10^{-18} W/m ²)	Ext?*
W3IRS5	1342229093	25543.0 \pm 3328.9	373064.6 \pm 28956.2	1027951.6 \pm 34137.0	YYY
	1342229091	22026.4 \pm 520.2	304283.8 \pm 1250.4	728668.6 \pm 1775.3	YYY
SMM J032537+30451	1342263508	1668.3 \pm 8.2	2260.4 \pm 28.9	2368.6 \pm 57.8	YYN
LDN1448N	1342263506	1609.5 \pm 10.0	4001.2 \pm 30.0	4927.1 \pm 66.8	YYY
L1448-C(S)	1342263510	545.1 \pm 12.6	1054.2 \pm 31.3	1418.6 \pm 95.2	YYY
IRAS 03235+3004	1342264250	238.0 \pm 11.0	361.0 \pm 25.8	492.8 \pm 72.9	YYN
LDN 1455	1342204122	65.0 \pm 14.0	<37.9	<102.2	NNN
2MASSJ03283706+3113310	1342264248	187.8 \pm 8.6	134.6 \pm 17.8	<99.0	NNN
SSTc2dJ032857.4+311416	1342264247	<30.0	<60.2	1239.7 \pm 55.7	YYY
SSTc2dJ032900.5+311200	1342264245	114.5 \pm 9.1	343.8 \pm 29.6	690.2 \pm 76.1	YYY
2MASSJ03290149+3120208	1342264243	1791.2 \pm 10.7	4074.3 \pm 34.3	6597.4 \pm 51.9	YYY
2MASSJ03290773+3121575	1342267612	1465.3 \pm 8.5	7009.4 \pm 47.5	21728.9 \pm 98.5	YYY
NGC1333IRAS4A	1342216084	140.6 \pm 20.1	419.7 \pm 54.7	485.9 \pm 126.9	YNN
	1342216083	119.3 \pm 5.2	362.7 \pm 10.6	183.8 \pm 41.1	YNN
SSTc2dJ032910.7+311821	1342267616	<28.1	999.2 \pm 23.6	2501.7 \pm 62.1	YYY
SSTc2dJ032912.0+311301	1342267608	260.3 \pm 7.4	110.8 \pm 12.4	<167.5	NNN
NGC1333IRAS4B	1342216178	111.0 \pm 23.0	235.0 \pm 42.6	<88.3	NNN
SSTc2dJ032913.5+311358	1342267610	54.0 \pm 10.6	<67.6	<107.4	NNN
IRAS03271+3013	1342263513	277.3 \pm 14.2	299.7 \pm 36.8	215.8 \pm 68.5	NNN
IRAS03282+3035	1342263515	146.4 \pm 13.4	258.9 \pm 33.3	<129.9	YNN
IRAS03292+3039	1342265448	163.1 \pm 9.0	211.8 \pm 16.9	255.5 \pm 52.2	NNN
IRAS03301+3111	1342215668	386.6 \pm 18.1	379.2 \pm 43.7	445.4 \pm 76.8	NNN
SSTc2dJ033314.3+310710	1342263487	92.7 \pm 7.7	186.5 \pm 24.3	493.9 \pm 77.0	YYY
SSTc2dJ033316.4+310653	1342265450	397.0 \pm 12.6	1076.1 \pm 29.9	1586.3 \pm 84.5	YYY
B1-a	1342216182	358.0 \pm 14.8	745.4 \pm 47.1	1008.5 \pm 119.3	YNN
SSTc2dJ033327.3+310710	1342265452	1065.3 \pm 5.2	1229.3 \pm 13.4	1259.6 \pm 49.4	YNN
IRAS03407+3152	1342265454	230.7 \pm 9.4	596.3 \pm 33.5	1267.0 \pm 57.1	YYY
SSTc2dJ034356.8+320305	1342265456	172.0 \pm 8.5	378.9 \pm 24.1	554.4 \pm 48.4	YYY
2MASSJ03444389+3201373	1342265702	600.5 \pm 6.9	868.1 \pm 13.5	758.6 \pm 72.2	YNN
IRAS04016+2610	1342216216	429.9 \pm 21.8	508.2 \pm 43.1	598.5 \pm 97.8	NNN
	1342204348	395.7 \pm 5.6	406.4 \pm 15.4	382.6 \pm 22.9	NNN
PP13S	1342263505	1102.0 \pm 41.0	1277.9 \pm 90.0	1460.1 \pm 175.7	NNN
V773Tau	1342216217	79.4 \pm 3.5	81.6 \pm 6.8	84.6 \pm 13.0	NNN
FMTau	1342216218	<11.6	19.8 \pm 6.5	<51.9	YNN
CWTau	1342216221	83.4 \pm 5.8	101.7 \pm 8.2	62.0 \pm 13.3	NNN
IRAS04158+2805	1342192793	55.1 \pm 4.2	53.6 \pm 8.4	63.1 \pm 17.8	NNN
BPTau	1342192796	6.8 \pm 2.4	<11.7	<49.3	NNN
	1342225728	9.3 \pm 2.9	10.8 \pm 3.1	<28.5	NNN
IRAS04169+2702	1342265457	608.3 \pm 7.0	951.3 \pm 25.2	1362.3 \pm 61.0	YYY
IRAS04181+2654	1342265459	206.0 \pm 6.4	235.4 \pm 15.4	213.1 \pm 28.8	NNN
IRAM04191	1342216654	161.2 \pm 22.7	176.7 \pm 35.8	269.4 \pm 93.3	NNN
RYTau	1342190361	99.6 \pm 5.8	85.7 \pm 10.0	85.5 \pm 23.2	NNN
TTau	1342190353	8337.1 \pm 15.2	16591.8 \pm 58.0	20023.0 \pm 69.0	YYY
2MASSJ04220069+2657324	1342265461	91.0 \pm 7.9	144.4 \pm 20.3	662.5 \pm 58.4	YYY
FSTau	1342192791	378.3 \pm 3.9	482.6 \pm 8.0	601.3 \pm 24.0	YYY
FTTau	1342192790	19.6 \pm 6.2	<23.3	<55.1	NNN
DGTauB	1342192798	130.0 \pm 4.8	582.7 \pm 14.9	739.2 \pm 29.3	YYY
	1342265463	514.7 \pm 10.5	722.6 \pm 32.4	810.6 \pm 58.2	YYN
DFTau	1342190359	51.9 \pm 7.0	35.9 \pm 9.0	<70.3	NNN
DGTau	1342190382	605.7 \pm 7.3	1492.7 \pm 20.8	1709.3 \pm 42.1	YYY
	1342225730	1533.0 \pm 14.7	1682.4 \pm 45.0	1921.8 \pm 89.6	YYN
IRAS04248+2612	1342265466	172.8 \pm 9.5	207.0 \pm 20.5	293.9 \pm 44.9	NNN
FWTau	1342225735	<10.0	17.0 \pm 5.6	<44.7	YNN
IRAS04264+2433	1342265468	569.3 \pm 9.3	628.0 \pm 22.4	709.8 \pm 38.6	NYN
IQTau	1342192135	<11.8	15.6 \pm 4.6	<61.7	YNN
	1342225733	16.0 \pm 2.6	<19.0	<35.6	NNN
UXTau	1342204350	37.7 \pm 3.6	32.6 \pm 6.0	<45.7	NNN
	1342214357	34.7 \pm 3.1	29.6 \pm 4.7	<55.1	NNN
DKTau	1342225732	21.2 \pm 3.6	<16.3	<30.2	NNN
IRAS04287+1801	1342192805	4611.6 \pm 77.2	6547.5 \pm 203.3	8233.6 \pm 171.5	YYY
HLTau	1342190351	510.5 \pm 10.5	859.8 \pm 32.7	1413.5 \pm 38.5	YYY
HKTau	1342225736	36.6 \pm 3.3	35.2 \pm 6.6	44.5 \pm 11.1	NNN
Haro6-13	1342192128	63.4 \pm 5.3	47.5 \pm 6.1	<48.4	NNN
GGTau	1342192121	51.9 \pm 4.9	52.2 \pm 8.0	84.9 \pm 23.8	NNN
UZTau	1342192131	<13.1	48.2 \pm 13.9	<62.8	YNN
GITau	1342225760	<7.1	39.7 \pm 8.4	<34.6	YNN
DLTau	1342225800	26.9 \pm 2.7	23.3 \pm 3.4	18.1 \pm 7.9	NNN
HNTau	1342225796	49.4 \pm 2.8	65.8 \pm 6.9	58.3 \pm 15.1	NNN
DMTau	1342225825	10.8 \pm 3.1	<12.7	<29.4	NNN
CITau	1342192125	27.0 \pm 3.9	21.4 \pm 6.6	<62.0	NNN
AATau	1342190357	<10.9	32.6 \pm 9.9	<48.6	YNN
	1342225758	24.3 \pm 2.1	17.8 \pm 2.2	<29.8	NNN
DNTau	1342225757	4.0 \pm 1.2	<14.8	<30.5	NNN

Table B.3. continued.

Source name	obs ID	$F_{[OI]}$ (10^{-18}W/m^2)	$F_{[OI]3\times 3}$ (10^{-18}W/m^2)	$F_{[OI]5\times 5}$ (10^{-18}W/m^2)	Ext?*
IRAS04325+2402	1342267857	478.9±10.7	634.0±25.6	670.1±43.7	YYN
DOTau	1342190385	62.8±8.5	158.0±14.4	267.5±61.4	YYN
HVTau	1342225801	39.3±4.3	83.9±7.4	112.3±30.1	YNN
TMR1B	1342225834	360.2±6.6	704.8±27.5	738.8±76.3	YYN
TMR1	1342192985	401.3±19.4	711.4±58.2	743.1±138.3	YNN
LkCa15	1342225798	11.3±2.2	<10.6	<22.4	NNN
IRAS04365+2535	1342225832	446.0±13.1	816.2±26.8	892.1±56.3	YYN
	1342192987	529.8±31.1	875.0±59.7	858.9±106.9	YNN
L1527	1342192981	243.3±19.4	778.3±67.1	1259.1±108.3	YYY
	1342192983	260.9±5.8	728.7±17.0	1227.8±55.3	YYY
IRAS04381+2540	1342225803	922.9±17.1	1268.3±50.4	1514.5±114.9	YYN
	1342225830	111.4±8.9	1321.5±16.4	1504.7±71.1	YYN
CoKuTau4	1342191360	19.6±5.3	<14.9	<56.0	NNN
	1342225837	23.1±1.4	16.9±1.5	<24.1	NNN
IRAS04385+2550	1342225828	66.1±2.8	75.9±6.3	86.6±14.7	NNN
DPTau	1342191362	<10.7	123.9±11.9	143.4±21.9	YYN
DQTau	1342225806	24.8±4.7	33.6±8.1	<57.1	NNN
Haro6-37	1342225805	<15.1	11.7±3.0	<58.7	YNN
UYAur	1342193206	<10.6	343.4±9.4	354.2±20.0	YYN
	1342215699	338.3±5.8	370.1±10.2	386.1±24.5	NNN
GMAur	1342191357	23.4±4.4	56.5±15.6	<60.9	NNN
ABAur	1342191355	666.5±19.6	849.5±10.6	919.4±19.9	YYY
	1342217842	358.6±27.0	888.5±64.4	1018.1±132.7	YYN
SUaur	1342217844	85.7±3.1	114.4±6.0	127.0±11.8	YYN
HD31648	1342226002	101.3±2.5	92.9±5.1	105.3±14.3	NNN
RWAur	1342191359	157.5±9.3	214.0±20.6	249.2±38.9	NNN
HD35187	1342226900	27.2±2.9	34.1±3.7	30.9±9.1	NNN
HD36112	1342227635	39.3±3.5	40.6±4.3	47.4±13.2	NNN
HD36910	1342227638	49.0±3.1	51.0±6.3	<35.3	NNN
HD245906	1342228528	87.6±24.1	197.2±59.8	<157.4	NNN
[SMZ2000]L1643-S3MMS1	1342226195	1554.1±7.9	2116.5±16.2	2462.8±61.2	YYY
Re50NNIRS	1342265946	1054.4±31.8	1176.1±68.0	1297.0±178.6	NNN
HD38120	1342226212	66.0±15.9	<45.0	<99.8	NNN
V1647Ori	1342267864	139.2±32.0	95.1±26.0	<332.2	NNN
NGC2071IR	1342218761	7995.8±39.3	40864.6±154.3	60785.1±199.4	YYY
HD50138	1342206991	2103.4±16.1	2125.3±41.9	2464.9±87.5	YYY
RECX4	1342199241	1.0±0.3	<13.1	<33.7	NNN
RECX15	1342186314	30.1±6.0	30.7±7.7	<41.0	NNN
RECX15	1342210388	23.8±2.5	19.4±3.6	<20.4	NNN
MGL99]IRS1757	1342211844	8155.9±11.5	18459.8±47.9	25508.3±79.9	YYY
SzCha	1342233478	14.5±1.8	<18.4	<27.0	NNN
CRCha	1342232614	16.4±2.6	<17.7	<25.8	NNN
TWA01	1342248544	32.4±4.7	33.1±4.3	33.8±10.9	NNN
	1342187127	34.8±3.9	55.1±11.1	<33.3	NNN
CSCha	1342233480	16.5±1.8	<19.8	<22.6	NNN
CHX7	1342233477	15.4±1.7	<29.8	64.7±10.6	YYY
HD97048	1342199412	852.7±18.3	991.3±47.5	1230.0±94.4	YYN
	1342188436	1481.4±3.7	1415.3±6.1	1485.9±18.9	NNY
Sz27	1342233476	9.8±1.3	<18.3	<21.3	NNN
GMCha	1342267619	221.4±13.3	283.2±26.4	555.4±65.2	YYY
T42	1342232291	492.8±58.6	985.6±287.2	1447.4±357.1	NNN
WWCha	1342232292	422.1±55.3	<239.3	<389.6	NNN
Hn13	1342263492	4.1±1.1	<13.4	<18.4	NNN
CHX22	1342233474	24.4±1.4	21.4±6.2	<28.3	NNN
HD98800B	1342223821	<7.1	15.3±3.5	<39.5	YNN
	1342199409	7.9±2.0	<11.4	<24.3	NNN
HD98922	1342210385	196.8±16.5	260.6±55.8	<68.8	NNN
HD100453	1342203059	58.0±5.2	51.0±6.5	<51.4	NNN
	1342212228	34.0±3.0	36.7±5.4	<42.3	NNN
	1342211695	113.4±39.2	<44.5	<80.8	NNN
HD100546	1342188038	5461.5±71.5	5339.0±92.2	5536.9±124.6	NNN
	1342188438	5645.1±8.3	5605.1±11.8	5923.6±20.1	YYY
TChA	1342232294	48.3±3.9	64.9±18.4	56.8±15.8	NNN
HD104237	1342207819	85.1±16.9	<47.7	<107.3	NNN
	1342212234	79.5±4.0	71.3±5.9	96.0±18.4	NNN
IRAS11590-6452	1342212230	1352.1±41.3	1817.4±73.5	2376.8±117.4	YYY
	1342212232	1340.4±33.9	1935.1±81.1	2229.8±101.6	YYN
DK Cha	1342188039	1329.5±119.1	3095.9±302.7	3696.5±219.7	YYN
	1342226006	2715.9±77.9	3197.7±239.2	3773.0±169.4	NNN
ChaII-J125342.86-771511.5	1342226005	72.9±3.2	72.4±8.8	70.7±11.6	NNN
2MASSJ12590656-7707401	1342265694	139.1±8.9	144.4±27.8	150.2±41.4	NNN
ChaII-J130055.36-771022.1	1342226008	<6.5	<13.0	60.9±16.7	YYY
ChaII-J130424.92-775230.1	1342229800	10.0±3.1	<14.1	<40.5	NNN
Hn24	1342235656	8.7±1.7	<18.2	<30.0	NNN

Table B.3. continued.

Source name	obs ID	$F_{[OI]}$ (10^{-18}W/m^2)	$F_{[OI]3\times 3}$ (10^{-18}W/m^2)	$F_{[OI]5\times 5}$ (10^{-18}W/m^2)	Ext?*
ChaII-J130520.68-773901.4	1342229831	14.9 \pm 4.6	<11.3	<30.5	NNN
ChaII-J130521.66-773810.0	1342229830	6.4 \pm 2.0	<9.4	<30.0	NNN
ChaII-J130806.28-775505.2	1342229801	15.0 \pm 4.3	<16.3	<30.8	NNN
ChaII-J130827.17-774323.2	1342228419	<7.8	4.6 \pm 1.0	<35.2	YNN
SAO206462	1342190370	42.7 \pm 5.0	45.9 \pm 8.6	<60.1	NNN
HD139614	1342191300	41.4 \pm 6.7	55.9 \pm 13.5	<46.4	NNN
	1342215683	19.0 \pm 5.9	<53.6	<106.0	NNN
HD141569	1342190376	190.6 \pm 4.3	218.3 \pm 8.6	199.2 \pm 28.5	NNN
	1342213913	202.9 \pm 19.1	220.4 \pm 33.6	<80.1	NNN
HD142666	1342214224	13.5 \pm 2.4	22.2 \pm 4.5	<29.9	NNN
HD142527	1342216173	49.5 \pm 3.0	44.6 \pm 5.8	39.9 \pm 10.9	NNN
RULup	1342215682	184.5 \pm 20.3	133.0 \pm 42.5	<105.4	NNN
RYLup	1342216171	<20.3	60.9 \pm 14.4	<71.6	YNN
USCoJ160421.7-213028	1342215681	24.9 \pm 2.2	31.2 \pm 4.8	35.7 \pm 11.9	NNN
Sz91	1342229827	8.2 \pm 1.5	<19.5	39.5 \pm 10.4	NNY
HD144668	1342192146	128.1 \pm 5.6	110.7 \pm 6.8	94.6 \pm 19.4	NNN
	1342215641	131.6 \pm 14.3	147.3 \pm 44.6	<83.2	NNN
Sz111	1342229828	9.7 \pm 1.4	<17.4	<23.8	NNN
AS205	1342215737	222.0 \pm 21.3	248.3 \pm 55.5	<107.2	NNN
USCoJ161420.2-190648	1342216191	43.1 \pm 3.7	43.5 \pm 5.8	62.0 \pm 20.1	NNN
RXJ1615.3-3255	1342229825	16.8 \pm 1.7	<20.1	<23.0	NNN
2MASSJ16230923-2417047	1342250127	19.4 \pm 1.6	32.4 \pm 9.1	40.5 \pm 9.2	NNN
Doar21	1342240163	385.1 \pm 56.2	1515.5 \pm 294.7	1575.7 \pm 354.2	YYN
GSS30-IRS1	1342215678	1836.3 \pm 51.4	4000.3 \pm 100.1	10189.4 \pm 165.8	YYY
VLA1623-243	1342213918	398.6 \pm 19.1	1653.6 \pm 64.2	3606.3 \pm 95.1	YYY
WL12	1342228187	494.4 \pm 17.6	408.9 \pm 31.9	309.8 \pm 74.0	NNN
DoAr28	1342241707	10.1 \pm 1.5	<18.8	<24.0	NNN
Oph01	1342266925	3109.3 \pm 9.8	7549.8 \pm 32.1	7938.9 \pm 60.2	YYY
Elias29	1342228519	1840.0 \pm 69.3	2521.7 \pm 92.8	3562.4 \pm 129.5	YYY
SR21	1342229824	12.6 \pm 4.1	<38.3	<54.3	NNN
IRS46	1342228474	75.3 \pm 22.6	718.4 \pm 77.4	1530.7 \pm 119.8	YYY
IRS44	1342228474	436.3 \pm 36.7	807.5 \pm 56.1	1530.7 \pm 119.8	YYY
IRS48	1342227069	322.3 \pm 18.7	362.4 \pm 42.6	457.1 \pm 80.8	NNN
GY314	1342242632	112.7 \pm 35.0	<168.3	<281.0	NNN
DoAr44	1342250578	25.3 \pm 1.5	32.3 \pm 9.7	<25.9	NNN
IRS63	1342228473	204.6 \pm 18.4	316.9 \pm 72.0	669.8 \pm 173.3	NNN
L1689SNO2	1342241270	235.5 \pm 70.4	<199.6	<288.4	NNN
2MASSJ16320099-2456419	1342263469	1091.7 \pm 11.8	1329.5 \pm 14.8	1354.9 \pm 55.2	YYN
V346Nor	1342267622	381.9 \pm 35.6	966.5 \pm 57.3	1482.9 \pm 136.1	YYY
RNO90	1342228206	128.1 \pm 19.8	<47.8	<72.2	NNN
HBC650	1342215639	811.2 \pm 5.7	1040.9 \pm 24.2	1055.5 \pm 76.7	YYN
HD150193	1342216625	22.8 \pm 3.4	52.0 \pm 10.2	<40.6	NNN
Sco01	1342267176	223.3 \pm 8.9	272.7 \pm 33.7	274.2 \pm 46.5	NNN
KKOph	1342192148	168.2 \pm 5.9	186.1 \pm 8.6	218.0 \pm 23.4	NNN
HD158643	1342217821	48.8 \pm 2.8	65.1 \pm 6.2	<38.4	NNN
HD163296	1342192161	206.4 \pm 5.3	209.9 \pm 12.2	197.4 \pm 22.4	NNN
	1342243512	197.1 \pm 5.5	228.8 \pm 10.4	237.5 \pm 17.3	NNN
	1342217819	210.5 \pm 18.3	220.7 \pm 56.6	<104.9	NNN
[SER2000]L483	1342192156	384.9 \pm 5.9	595.4 \pm 23.9	774.6 \pm 69.2	YYN
HD169142	1342186310	80.6 \pm 4.6	123.0 \pm 10.0	157.6 \pm 26.3	YNN
[MAM2011]Aqu-MM2	1342254233	47.7 \pm 14.5	172.0 \pm 40.0	212.1 \pm 68.3	NNN
[MAM2011]Aqu-MM4	1342254271	48.4 \pm 12.5	157.2 \pm 22.6	<150.0	YNN
[MAM2011]SerpS-MM1	1342254230	105.5 \pm 6.0	311.4 \pm 39.9	504.7 \pm 60.8	YYN
Serpens-SMM1a	1342207781	3329.5 \pm 24.9	6982.9 \pm 78.3	8213.7 \pm 139.3	YYY
Serpens-SMM4	1342193217	146.3 \pm 22.5	349.6 \pm 40.3	2858.9 \pm 112.5	YYY
Serpens-SMM3	1342207779	472.1 \pm 12.2	1557.0 \pm 18.9	3455.2 \pm 79.5	YYY
Serpens-SMM3	1342193216	121.3 \pm 24.9	931.5 \pm 46.1	2247.4 \pm 93.0	YYY
Serpens-SMM18	1342254222	113.2 \pm 7.6	2483.5 \pm 93.5	5440.7 \pm 103.7	YYY
[MAM2011]Aqu-MM7	1342254224	49.1 \pm 13.8	<63.5	<139.2	NNN
MAM2011]Aqu-MM8	1342254228	<25.2	26.3 \pm 7.5	<116.4	YNN
[MAM2011]W40-MM3	1342254220	59.5 \pm 6.6	706.3 \pm 18.5	2777.0 \pm 49.7	YYY
[MAM2011]W40-MM5	1342254268	801.8 \pm 11.7	4489.4 \pm 24.1	10708.7 \pm 46.1	YYY
[MAM2011]W40-MM26	1342254266	1581.5 \pm 10.0	10123.5 \pm 26.4	27140.0 \pm 97.4	YYY
[MAM2011]W40-MM27	1342254260	736.2 \pm 10.1	6070.4 \pm 27.7	20842.8 \pm 70.2	YYY
[MAM2011]W40-MM28	1342254264	656.3 \pm 7.1	5504.3 \pm 19.7	13798.5 \pm 65.8	YYY
[MAM2011]W40-MM36	1342254263	75.7 \pm 10.2	160.0 \pm 23.5	255.9 \pm 38.0	YYN
HD172555	1342215649	8.6 \pm 2.6	25.2 \pm 8.3	<32.0	NNN
	1342228417	10.5 \pm 3.2	<13.1	<32.8	NNN
SCra	1342207809	429.5 \pm 22.4	514.0 \pm 58.6	827.8 \pm 141.9	NNN
IRS5A	1342207806	1943.7 \pm 18.6	3467.4 \pm 183.1	5015.8 \pm 187.0	YYY
	1342207806	1939.8 \pm 18.4	3638.1 \pm 60.6	5488.0 \pm 91.2	YYY
IRS7A	1342206990	8706.1 \pm 61.7	26366.2 \pm 345.7	47729.5 \pm 320.4	YYY
IRS7B	1342207807	4768.1 \pm 71.2	26576.1 \pm 360.1	41090.1 \pm 283.0	YYY
CrA01	1342254253	1416.3 \pm 7.3	1946.1 \pm 36.7	2314.6 \pm 42.3	YYY

Table B.3. continued.

Source name	obs ID	$F_{[OI]}$ (10^{-18}W/m^2)	$F_{[OI]3\times 3}$ (10^{-18}W/m^2)	$F_{[OI]5\times 5}$ (10^{-18}W/m^2)	Ext?*
HD179218	1342208884	213.1 ± 16.5	229.9 ± 42.1	<96.4	NNN
LDN723-mm	1342208918	227.9 ± 7.2	250.3 ± 19.1	306.2 ± 47.6	NNN
[SER2000]B335	1342208889	421.5 ± 25.9	553.9 ± 56.2	606.7 ± 125.9	NNN
AFGL 2591	1342208938	<428.9	27712.4 ± 292.1	46314.9 ± 377.2	YYY
LDN1157-mm	1342208909	595.0 ± 21.2	771.5 ± 40.7	885.3 ± 88.2	YYN
HH381IRS	1342258845	209.6 ± 41.0	<136.5	480.5 ± 117.8	NNY
L1014	1342208911	75.8 ± 15.5	<46.3	<109.4	NNN
HH354IRS	1342262014	602.1 ± 21.4	639.8 ± 47.3	<317.4	NNN
NGC 7538 IRS1	1342211545	45247.8 ± 146.9	148957.8 ± 610.7	257177.9 ± 689.3	YYY

Notes. (*): the extended emission column shows the results for the 3x3 spaxels versus 1 spaxel/ 5x5 versus 1 spaxel and / 5x5 versus 3x3 spaxels.